A DFT STUDY ON INTERACTION BETWEEN Au, Re AND Au-Re SURFACES WITH SPECIES INVOLVED IN WGS REACTION

by

Ali Uzun

B.S., Chemical Engineering, Boğaziçi University, 2009

Submitted to the Institute for Graduate Studies in
Science and Engineering in partial fulfillment of
the requirements for the degree of
Master of Science

Graduate Program in Chemical Engineering
Boğaziçi University

2012

to my parents and brother

ACKNOWLEDGEMENTS

Firstly, I would like to express my sincere thanks to my thesis supervisor Prof. Ahmet Erhan Aksoylu. His advices helped me to improve my work and his guidance was invaluable throughout my thesis.

I am very grateful to my thesis committee members; Prof. Ramazan Yıldırım and Assoc. Prof. Hasan Bedir for kindly revising and commenting on my thesis.

I wish to express my gratitude to Aslıhan Sümer who deserves special thanks for her great contribution during teaching me CASTEP and DMol3. I also would like to thank Vasfiye Çimenoğlu for her friendship and sharing experiences with me as a special colleague.

I wish to express my gratitude to the members of 411/A, Burcu Selen Çağlayan, Feyza Gökaliler, Tuğba Davran Candan and Merve Eropak who deserve heartfelt thanks for their friendship, support and invaluable help throughout my thesis.

I would like to thank to other members of CATREL group, Bilge Kerem Aksakal, Melek Selcen Başar, Aybüke Leba and Aysun İpek Paksoy for their friendship and help. I also thank my friends - İhsan Ömür Akdağ, Nilay Aktürk, Tarık Can, Elif Dereli, Aslıgül Doğan, Murat Erol, Gülsüm Ersoy, Mehmet Ünal Güneş, İrfan Hösükoğlu, Cihan Kaya, Bahadır Kara, Duygu Kocaman, Çağlar Meriçer, Bahar Nalbantoğlu, Kerem Şefik Ovalı, Caner Ülgüel, Simay Yalaz, Cansu Yassı, Burcu Yoğurtçu and Okan Yüzüak - for their friendship and making this period cheerful and enjoyable.

Cordial thanks are for Bilgi Dedeoğlu, Nurettin Bektaş and Yakup Bal for their technical assistance and invaluable help.

Very special thanks should be addressed to Nihan Yılmaz, Mehtap Yücel and Yelda Semizer for their friendship, endless support and encouragement on any matter.

I cannot find the right words for the person who is there whenever I needed her help on any matter. I wish to thank Alev Güneş with all my heart and soul for her endless patience, everlasting support and encouragement during my thesis study.

Finally, I would like to express my very great appreciation to my parents, Cemile and Mehmet Uzun, and my brother, Anıl Uzun, for their unconditional love, endless patience and everlasting support throughout my whole life. This work is dedicated to them, without whom it would have never been possible.

The graduate scholarship provided by TÜBİTAK for my M.S. studies deserves thankful recognition. Financial support provided by TÜBİTAK through project 105M282, and by Boğaziçi University Research Fund through projects BAP 09M104 and BAP 5570.

ABSTRACT

A DFT STUDY ON INTERACTION BETWEEN Au, Re AND Au-Re SURFACES WITH SPECIES INVOLVED IN WGS REACTION

In this study, the steps of WGS reaction was investigated through studying the adsorption/co-adsorption of its reactants, products and possible intermediate species on Au(111), Re(001) and Au-Re(001) surfaces at atomic scale via utilizing DFT modules of CASTEP. Firstly, the adsorption energies of CO, OH, CO_2, H_2O, HOCO molecules and H atoms on Au(111) and Re(001) surfaces, LDOS profiles of these adsorbates for their free and in adsorbed state, and the surface metal atoms on the adsorption sites of Au(111) and Re(001) surfaces for their bare and adsorbed state were analyzed. Additionally, CO-OH co-adsorption on Au(111) and Re(001) surfaces were carried out in order to analyze the reaction steps of WGS reaction on Au(111) and Re(001) surfaces. In the second part of the study, Au-Re surface alloys were generated by the addition of Au atoms on Re(001) surface as point defects. The adsorptions/co-adsorptions of CO and OH molecules on Au-Re(001) surface alloys having different Au concentration on Re(001) were carried out in order to understand the reason of high activity and selectivity of Au-Re/Ceria catalysts. The results revealed that monometallic Au and Au-Re surface alloy are active catalysts, whereas Re is not an active catalyst for WGS reaction. It was found that OH has stronger interaction with Au surface than that of CO in terms of its high binding energy, and it is inferred that the active sites on Au surface, which dominantly participate in WGS reaction steps, can be poisoned by OH molecules due to site competition. The results also showed that the binding energies of OH on Re are higher than that of OH on Au, and it is concluded that OH molecules can move from Au sites to Re sites, and the active sites on Au surface can be poisoned by OH molecules to a lesser degree. The co-adsorption of CO and OH molecules on Au(111), Re(001) and Au-Re surfaces revealed that WGS reaction takes place on Au sites of monometallic and Au-Re surface alloy, and the surface reaction between CO and OH molecules on Au is consistent with the carboxyl mechanism.

ÖZET

Au, Re VE Au-Re YÜZEYLERİNİN WGS REAKSİYONUNDA VAROLAN ATOM VE MOLEKÜLLER İLE ETKİLEŞİMİ ÜZERİNE DFT ÇALIŞMASI

Bu çalışmada; gaz-buhar geçişi (WGS) reaksiyonu reaktanların, ürünlerin ve muhtemel ara ürünlerin Au(111), Re(001) ve Au-Re(001) yüzeyleri üzerindeki adsorpsiyon ve koadsorpsiyonları CASTEP™'in DFT modülleri kullanılarak atomik ölçekte incelenmiştir. İlk olarak, CO, OH, CO_2, H_2O, HOCO moleküllerinin ve H atomunun Au(111) ve Re(001) yüzeyleri üzerindeki adsorpsiyon enerjileri hesaplanmıştır. Ardından, bu adsorbe edilen moleküllerin serbest ve adsorpsiyon sonrası enerji düzeyleri lokal yoğunluğu (LDOS) profilleri ile Au(111) ve Re(001) yüzeylerindeki adsorpsiyon sitelerindeki metal atomlarının adsorpsiyon öncesi ve sonrası LDOS profilleri analiz edilmiştir. Bunlara ek olarak, WGS reaksiyonun Au(111) ve Re(001) yüzeyleri üzerindeki adımlarının analiz edilmesi amacı ile CO ve OH moleküllerinin bu yüzeyler üzerindeki koadsorpsiyonu incelenmiştir. Çalışmanın ikinci bölümünde, Au-Re/CeO_2 katalizörünün WGS reaksiyonunda gösterdiği yüksek aktivite ve seçimliliğin nedenlerinin belirlenebilmesi amacı ile Re(001) yüzeyine Au atomları eklenerek Au-Re yüzey alaşımları oluşturulmuş ve farklı Au konsantrasyonuna sahip Au-Re yüzey alaşımları üzerinde CO ve OH moleküllerinin adsorpsiyon ve koadsorpsiyonları incelenmiştir. Sonuçlar; WGS reaksiyonun Au ve Au-Re yüzeyleri üzerinde gerçekleşebileceğini, ancak Re yüzeyinin bu reaksiyon açısından aktif olmadığını göstermiştir. WGS reaksiyonunda ağırlıklı olarak görev alan Au aktif siteleri üzerinde OH molekülünün CO molekülüne nazaran daha yüksek bağlanma enerjisine sahip olduğu saptanmış ve bu yüksek etkileşimin Au aktif sitelerinin OH tarafından geniş ölçüde zehirlenmesine sebep olabileceği anlaşılmıştır. OH molekülünün Re üzerindeki bağlanma enerjisinin ise Au üzerindeki bağlanma enerjisinden daha yüksek olduğu hesaplanmış ve Au yüzeyindeki OH moleküllerinin Re yüzeyine transfer olması sonucunda Au yüzeyindeki zehirlenmenin daha düşük seviyede gerçekleşeceği sonucuna varılmıştır. CO ve OH moleküllerinin Au(111), Re(001) ve Au-Re yüzeylerindeki koadsorpsiyonları ışığında WGS reaksiyonun Au siteleri üzerinde gerçekleştiği ve bu moleküller arasındaki yüzey reaksiyonun karboksil mekanizması ile örtüştüğü gösterilmiştir.

TABLE OF CONTENTS

ACKNOWLEDGEMENTS..... iv
ABSTRACT..... vi
ÖZET..... vii
LIST OF FIGURES..... x
LIST OF TABLES..... xv
LIST OF SYMBOLS..... xviii
LIST OF ACRONYMS/ABBREVIATIONS..... xix
1. INTRODUCTION..... 1
2. LITERATURE SURVEY..... 4
2.1. Fuel Processor-Fuel Cell System..... 4
2.2. Water-Gas Shift (WGS) Reaction..... 5
2.3. Commercial Catalyst for WGS Reaction. 5
2.4. Au-Based Catalysts for WGS Reaction..... 7
2.4.1. Experimental Studies..... 8
2.4.2. Computational Studies..... 10
2.5. The Effect of Rhenium on WGS reaction..... 13
2.6. Au-Re Catalyst..... 15
2.7. Theory behind Computational Methods..... 16
2.7.1. Schrödinger Equation..... 17
2.7.2. Density Functional Models..... 18
3. CALCULATION..... 21
3.1. The Materials Studio Software..... 21
3.1.1. MS Visualizer..... 21
3.1.2. MS CASTEP..... 21
3.2. Computational Details of CASTEP..... 22
3.3. Optimizing Bulk Au and Re..... 23
3.4. Building and Optimizing the Au(111) and Re(001) Surfaces..... 24
3.5. Calculating the Adsorption Energies..... 25
3.6. Calculating the Surface Energies of Au-Re Surfaces..... 27

3.7. LDOS Profiles..... 27
4. RESULTS AND DISCUSSIONS..... 28
4.1. Au(111) Surface..... 28
4.1.1. CO Adsorption on Au(111)..... 30
4.1.2. OH Adsorption on Au(111)..... 34
4.1.3. H_2O Adsorption on Au(111)..... 38
4.1.4. CO_2 Adsorption on Au(111)..... 41
4.1.5. H Adsorption on Au(111)..... 43
4.1.6. CO-OH Co-adsorption on Au(111)..... 47
4.2. Re(001) Surface..... 51
4.2.1. CO Adsorption on Re(001)..... 52
4.2.2. OH Adsorption on Re(001)..... 55
4.2.3. H_2O Adsorption on Re(001)..... 58
4.2.4. CO_2 Adsorption on Re(001)..... 60
4.2.5. H Adsorption on Re(001)..... 63
4.2.6. CO-OH Co-adsorption on Re(001)..... 65
4.3. Au-Re Surface Alloys..... 67
4.3.1. CO Adsorption on Au-Re Surface..... 71
4.3.2. OH Adsorptions on Au-Re Surface..... 72
4.3.3. CO-OH Co-adsorptions on Au-Re Surface..... 74
5. CONCLUSIONS AND RECOMMENDATIONS..... 79
5.1. Conclusions..... 79
5.2. Recommendations..... 80
REFERENCES..... 81

LIST OF FIGURES

Figure 2.1. The Fuel Processor (FP). 5

Figure 3.1. The visual models of (a) Au and (b) Re unit cells. 24

Figure 3.2. The visual models of (2x3) slabs for (a) Au(111) and (b) Re(001) surfaces. 25

Figure 4.1. Top view (a) and side view (b) of Au(111) surface. 29

Figure 4.2. The possible adsorption sites on Au(111) single crystal surface: A, B and T. 29

Figure 4.3. The top views of optimized CO adsorption on (a) site A, (b) site B, and (c) site T on Au(111). 31

Figure 4.4. LDOS of (a) d-states of Au atom for its bare and atop CO coordinated states, (b) d-states of Au atom for its bare and threefold CO coordinated states, and (c) C of CO for its free and threefold coordinated states. 33

Figure 4.5. The visual models of optimized OH adsorption on (a) site A -top view-, (b) site B -top view-, (c) site B -side view-, and (d) site T -top view- on Au(111). 35

Figure 4.6. LDOS of (a) d-states of Au atom for its bare and bridge OH coordinated states and (b) O of OH for its free and bridge coordinated states. 37

Figure 4.7. The visual models of H_2O adsorption on site A of Au(111): (a) side view prior to energy optimization, (b) side view upon energy optimization, and (c) top view upon energy optimization. 39

Figure 4.8. LDOS of (a) d-states of Au atom for its bare and atop H_2O coordinated states, (b) O of H_2O for its free and atop coordinated states, and (c) d-states of Au atom for its bare and bridge H_2O coordinated states. 40

Figure 4.9. The visual models of CO_2 adsorption on site A of Au(111): (a) side view prior to energy optimization, (b) side view upon energy optimization and (c) top view upon energy optimization. 42

Figure 4.10. LDOS of (a) d-states of Au atom for its bare and atop CO_2 coordinated states and (b) C of CO_2 for its free and atop coordinated states. 43

Figure 4.11. The top views of optimized H adsorption (a) on site A and (b) on site T on Au(111). 45

Figure 4.12. LDOS of (a) d-states of Au atom for its bare and atop H coordinated states, (b) d-states of Au atom for bare threefold H coordinated states, and (c) H atom for its free and threefold coordinated states. ... 46

Figure 4.13. The visual model of the carboxyl (cis-HOCO). 47

Figure 4.14. The visual models of CO-OH co-adsorption on Au(111) during energy optimization: (a) initial, (b) and (c) intermediates, and (d) final stages. 48

Figure 4.15. LDOS of (a) d-states of Au atom for its bare and atop coordinated states and (b) C of HOCO for its free and atop coordinated states upon CO-OH co-adsorption, and (c) C of HOCO for its free and atop coordinated states upon HOCO adsorption. 50

Figure 4.16. Top view (left) and side view (right) of Re(001) single crystal surface. 51

Figure 4.17. The possible adsorption sites A, B and T on Re(001) single crystal surface. 51

Figure 4.18. The top views of optimized CO adsorption on (a) site A, (b) site B, and (c) site T on Re(001). 53

Figure 4.19. LDOS of (a) d-states of Re atom for its bare and atop CO coordinated states and (b) C of CO for its free and atop coordinated states. 54

Figure 4.20. The visual models of optimized OH adsorption (a) on site A -top view-, (b) on site A -side view-, and (c) on site T -top view- on Re(001). 56

Figure 4.21. LDOS of (a) d-states of Re atom for its bare and atop OH coordinated states and (c) O of OH for its free and atop coordinated states. 57

Figure 4.22. The visual models of H_2O adsorption on site A of Re(001): (a) side view prior to energy optimization, (b) side view upon energy optimization, and (c) top view upon energy optimization. 59

Figure 4.23. LDOS of (a) d-states of Re atom for its bare and atop H_2O coordinated states and (b) O of H_2O for its free and atop coordinated states. 60

Figure 4.24. The side views of optimized CO_2 adsorption (a) on site A, (b) on site B, and (c) on site T on Re(001). 62

Figure 4.25. LDOS of (a) d-states of Re atom for its bare and atop CO_2 coordinated states and (b) C of CO_2 for its free and atop coordinated states. 62

Figure 4.26. LDOS of (a) d-states of Re atom for its bare and bridge CO_2 coordinated states, and (b) C of CO_2 for its free and bridge coordinated states. 63

Figure 4.27. The visual models of optimized H adsorption on site T of Re(001): (a) top view and (b) side view. 64

Figure 4.28. LDOS of (a) d-states of Re atom for its bare and threefold H coordinated states and (b) H atom for its free and threefold coordinated states. 65

Figure 4.29. The visual models of CO-OH co-adsorption on Re(001): (a) initial structure (CO-atop and OH-atop) and (b) final structure (CO-atop and OH-atop). 67

Figure 4.30. The pseudomorphic Au-Re surface alloys: (a) $Au_{1/6}$/Re(001), (b) $Au_{3/6}$/Re(001), and (c) $Au_{6/6}$/Re(001). 69

Figure 4.31. Surface energy vs. Au concentration at topmost layer which increases from 0, monometallic Re(001) surface, to 6/6 (100%), pseudomorphic Au layer over Re(001). 70

Figure 4.32. LDOS of d-band of Au atoms for its bare states on $Au_{1/6}$/Re(001), $Au_{3/6}$/Re(001), and $Au_{6/6}$/Re(001) surface alloys, and Au atom for its bare state on monometallic Au(111). 70

Figure 4.33. The top views of optimized CO adsorption on atop Au sites of (a) $Au_{1/6}$/Re(001), (b) $Au_{3/6}$/Re(001), and (c) $Au_{6/6}$/Re(001) surface alloys upon energy optimization. 72

Figure 4.34. The top views of OH adsorption on $Au_{3/6}$/Re(001): (a) initial (OH on bridge Au) and (b) final (OH on atop Re) structures. 74

Figure 4.35. The top views of CO-OH co-adsorption on $Au_{1/6}$/Re(001) surface alloy: (a) initial (CO-atop Au and OH-atop Re) and (b) final (CO-atop Au and OH-bridge Re) structures. 75

Figure 4.36. The visual models of CO-OH co-adsorption on $Au_{3/6}$/Re(001) surface alloy: (a) initial and (b) final structures for the first co-adsorption configuration, and (c) initial and (d) final (side view) structures for the second co-adsorption configuration. 76

LIST OF TABLES

Table 3.1. Adsorbates and their total energies ($E_{adsorbate}$). 26

Table 4.1. The adsorption studies on Au(111) with the adsorbates and adsorption sites. 29

Table 4.2. Adsorption sites (Site), adsorption energy (E_{ads}), distance between C of CO and metal surface ($d_{C\text{-}Surface}$), and bond length in CO molecule ($d_{C\text{-}O}$) upon CO adsorption on Au(111). 30

Table 4.3. Adsorption sites (Site), adsorption energy (E_{ads}), distance between O of OH and metal surface ($d_{O\text{-}Surface}$), and bond length in OH molecule ($d_{O\text{-}H}$) upon OH adsorption on Au(111). 34

Table 4.4. Adsorption sites (Site), adsorption energy (E_{ads}), distance between O of H_2O and metal surface ($d_{O\text{-}Surface}$), bond lengths ($d_{O\text{-}H}$) and bond angle (H-O-H) in H_2O upon H_2O adsorption on Au(111). 38

Table 4.5. Adsorption sites (Site), adsorption energy (E_{ads}), distance between C of CO_2 and metal surface ($d_{C\text{-}Surface}$), bond lengths ($d_{C\text{-}O}$) and bond angle (O-C-O) in CO_2 upon CO_2 adsorption on Au(111). 41

Table 4.6. Adsorption sites (Site), adsorption energy(E_{ads}), and the distance between H atom and metal surface ($d_{H\text{-}Surface}$) upon H adsorption on Au(111). 44

Table 4.7. Co-adsorption sites (Site), adsorption energy (E_{ads}), and distance between the carbon of HOCO and Au atom ($d_{C\text{-}surface}$) upon CO-OH co-adsorption. 48

Table 4.8. The values of bond lengths and angles of HOCO on Au atop (upon CO-OH co-adsorption) and HOCO on Au atop (upon HOCO adsorption). 49

Table 4.9. The adsorption studies on Re(001) with the adsorbate and adsorption sites. 52

Table 4.10. Adsorption sites (Site), adsorption energy (E_{ads}), distance between C of CO and metal surface ($d_{C\text{-}Surface}$), and bond length in CO ($d_{C\text{-}O}$) upon CO adsorption on Re(001). 52

Table 4.11. Adsorption sites (Site), adsorption energy (E_{ads}), the distance between O of OH and metal surface ($d_{O\text{-}Surface}$), and the bond length in OH ($d_{O\text{-}H}$) upon OH adsorption on Re(001). 55

Table 4.12. Adsorption sites (Site), adsorption energy (E_{ads}), distance between O of H_2O and metal surface ($d_{O\text{-}Surface}$), bond length ($d_{O\text{-}H}$) and angle (H-O-H) in H_2O upon H_2O adsorption on Re(001). 58

Table 4.13. Adsorption sites (Site), adsorption energy (E_{ads}), distance between C of CO_2 and metal surface ($d_{C\text{-}Surface}$), bond length ($d_{C\text{-}O}$) and angle (O-C-O) in CO_2 upon CO_2 adsorption on Re(001). 61

Table 4.14. Adsorption sites (Site), adsorption energy (E_{ads}), and distance between H atom and metal surface ($d_{H\text{-}Surface}$) upon H adsorption on Re(001). 64

Table 4.15. Initial and final adsorption sites (CO Site and OH Site) for CO-OH co-adsorption. 66

Table 4.16. Surface energy (E_{Surf}) of Re(001) and Au-Re surface alloys with different Au concentrations at topmost surface layer. The top views of optimized surfaces are given in the first column: Dark balls (blue) represent Re, light ones (yellow) represent Au atoms. 68

Table 4.17. The initial and final sites, adsorption energy (E_{ads}), distance between C of CO and metal surface ($d_{C\text{-}Surface}$), and bond length in CO molecule ($d_{C\text{-}O}$) upon CO adsorption on $Au_{1/6}$/Re(001), $Au_{3/6}$/Re(001), and $Au_{6/6}$/Re(001) surface alloys. 71

Table 4.18. The initial and final sites, adsorption energy (E_{ads}), distance between O of OH and metal surface ($d_{O\text{-}Surface}$), and bond length in OH molecule ($d_{O\text{-}H}$) upon OH adsorption on $Au_{3/6}$/Re(001) and $Au_{6/6}$/Re(001) surface alloys. 73

Table 4.19. The values of bond lengths and angles of HOCO at atop on monometallic Au(111) upon HOCO adsorption, and HOCO formed at atop Au on Au-Re surface alloys upon CO-OH co-adsorption. 77

Table 4.20. Initial co-adsorption sites (Site), adsorption energy (E_{ads}), and distance between the carbon of HOCO and Au atom ($d_{C\text{-}surface}$) upon CO-OH co-adsorption on $Au_{3/6}$/Re(001), $Au_{3/6}$/Re(001) and $Au_{6/6}$/Re(001) surface alloys. 78

LIST OF SYMBOLS

A	Atop
B	Bridge
E	Energy
d	Distance
E_{ads}	Adsorption energy
E_{bulk}	Total energy per unit cell of the bulk crystal of metal
E_J	Hartree Coulomb energy for electron-electron interaction
E_{slab}	Total energy per unit cell of the slab
E_T	Electron energy
E_V	Electron-nuclear interaction energy
E_{XC}	Exchange-correlation energy
h, k, l	Miler indices
N	Number of atoms in the unit cell of the slab
r	Distance between the nucleus and the electron
T	Threefold
V_H	Hartree potential of the electrons.
V_{KS}	Kohn-Sham potential
V_{XC}	Exchange-correlation potential
Z	Nuclear charge
ε_{xc}	Exchange-correlation energy per electron
ε_i	Kohn-Sham eigenvalue
ρ	Total electron density
ψ	Wavefunction
ψ_i	Wavefunction of electronic state i

LIST OF ACRONYMS/ABBREVIATIONS

ADF	Amsterdam Density Functional
AFC	Alkaline Fuel Cell
CASTEP	Cambridge Serial Total Energy Package
CATREL	Catalyst Technology and Reaction Engineering Laboratory
CI	Configuration Interaction
DFT	Density Functional Theory
DOS	Density of States
dp	Deposition precipitation
DRIFTS	Diffuse Reflectance Infrared Fourier Transform Spectroscopy
FP	Fuel Processor
FTIR	Fourier Transform Infrared Spectroscopy
GGA	Generalized-Gradient Approximation
HR-TEM	High Resolution Transmission Electron Microscopy
HTS	High Temperature Shift
HT-WGS	High-Temperature Water-Gas Shift
imp	Impregnation
IR	Infrared
LDA	Local-Density Approximation
LDOS	Local Density of States
LTS	Low Temperature Shift
LT-WGS	Low-Temperature Water-Gas Shift
MCFC	Molten Carbonate Fuel Cell
ML	Monolayer
MP	Moller-Plesset Model
MP2	Second-Order Moller-Plesset Model
MS	Materials Studio
PAFC	Phosphoric Acid Fuel Cell
PBE	Perdew-Burke-Ernzerhof

PEM	Proton Exchange Membrane
PEM-FC	Proton Exchange Membrane Fuel Cell
PM	Precious Metal
PROX	Preferential Oxidation
PW91	Perdew–Wang exchange–correlation
RWGS	Reverse Water Gas Shift
SCF	Self-Consistent Field
SIESTA	Spanish Initiative for Electronic Simulations with Thousands of Atoms
SOFC	Solid Oxide Fuel Cell
SPFC	Solid Polymer Fuel Cell
TEM	Transmission Electron Microscopy
TOF	Turn over Frequency
TPR	Temperature Programed Reduction
VASP	Vienna Ab-initio Simulation Package
WGS	Water Gas Shift
XPS	X-ray Photoelectron Microscopy
XRD	X-ray Diffraction

1. INTRODUCTION

Fuel cell technology is a viable alternative for clean energy generation. Fuel Cell converts the chemical energy stored in a fuel into electricity through a chemical reaction with oxygen. This technology is suitable for small scale stationary and mobile applications. The different applications of fuel cell technology are under development. PEM-FC is considered to be the most promising fuel cell system since it possess a series of advantages for mobile power applications (vehicles) or for small stationary power units, such as low operating temperature, sustained operation at high current density, low weight, compactness and long stack life. However, PEM-FC has stable activity only if the feed stream is hydrogen rich with less than 50 ppm carbon monoxide. Therefore, it is necessary to produce hydrogen by a system including special CO clean up sections, namely by a fuel processor (FP) [1].

Fuel Processors convert hydrocarbons to CO-free hydrogen. In a fuel processor, three catalytic reactors are used in a sequential manner: Reforming, Water-Gas Shift and PROX. Depending on the reformer type, operating conditions and fuel, the WGS feed contains a significant levels of CO, 6–10%, at the reformer exit. The water–gas shift reactor reduces the CO concentration to 0.5-1%. After that, the PROX unit reduces CO content below 50 ppm, which can be tolerated by PEM-FC [1]. This study focuses on WGS reaction in the fuel processor.

Water-gas shift (WGS) is a reaction in which CO reacts with H_2O to produce H_2 and CO_2:

$$CO\ (g) + H_2O\ (g) \leftrightarrow H_2\ (g) + CO_2\ (g) \qquad \Delta H = -41.2\ kJ.mol^{-1}$$

The WGS reaction has a reversible nature; thus WGS reaction attains equilibrium with the reverse WGS (RWGS) reaction. The WGS reaction is moderately exothermic, and its equilibrium constant increases as temperature decreases. In other words, lower temperatures lead to an increase in the production of H_2. However, the higher temperatures

are needed to obtain necessary reaction rates. Therefore, a catalyst that is highly active at low temperatures is required for the intended FP-PEMFC applications [2].

To obtain high activity and conversion, WGS reaction is conventionally performed in two serial reactors: (i) the first one is high temperature shift (HTS) reactor uses Fe_2O_3/Cr_2O_3 catalyst at 350-450 °C, and (ii) the second one is low temperature shift (LTS) reactor uses $Cu/ZnO/Al_2O_3$ at 200-260 °C. On the other hand, these commercial catalysts are not suitable for small scale mobile or immobile fuel processing devices since they require special activation procedures and long pre-conditioning, have thermodynamic limitations at high temperature and slow kinetics at low temperatures, and are also pyrophoric. Therefore, there is a need of developing a single/multi stage WGS catalyst having sufficient activity at relatively low (HTS-LTS transition) temperatures for the intended applications which is at the same time, selective, thermally stable, non-pyrophoric, poison resistant, and steam tolerant. Precious metal (PM) catalysts, such as Au, Pd, Pt or Re on different oxide supports, e.g. CeO_2, ZrO_2, and TiO_2, are popular in this case, because of their high stability, high conversion, and high selectivity. They have been explored and reported to be effective for WGS. Many catalytic systems have been investigated; however, an effective commercial catalyst is still under development [3].

In the studies of WGS catalyst, it was shown that Au/ceria catalysts exhibit a high and stable activity for the WGS reaction [4, 5], but those catalysts are reported intolerant to H_2O parallel to the results presented in literature, in the experimental study of Çağlayan and Aksoylu, it was reported that the activity of Au/ceria catalyst decreases as H_2O/CO feed ratio increases [6]. On the other hand, many research groups have reported that Re can improve the activity of many reactions when it is used as a second metal [7, 8]. In CATREL (Catalyst Technology and Reaction Engineering Laboratory), Çağlayan and Aksoylu investigated water gas shift activity under ideal feed conditions on ceria supported Au, Re, and Au-Re catalysts. The experimental tests performed on investigating characterization, and WGS activity and selectivity of $Au-Re/CeO_2$ system reveal that the catalyst has Au-Re surface alloys and it has superior activity and selectivity in WGS reaction. Additionally, it retains its high activity level for high steam concentrations in the feed stream. As the catalyst has sequential addition of Re followed by Au precursors, Au-Re mixed layers are formed on Re clusters, which was confirmed by HR-TEM [6].

The aim of this study is to understand the reasons of high activity and selectivity of Au-Re system through analyzing the steps of WGS reaction via quantum mechanical simulations. In this study, the steps of WGS reaction was investigated at atomic scale through studying the adsorptions of its reactants, products and possible intermediate species on Au(111), Re(001) and Au-Re(001) surfaces by using DFT modules in CASTEP in order to understand how Au-Re surface alloy functions during the reaction. Firstly, the adsorption energies of CO, OH, CO_2, H_2O, HOCO molecules and H atoms on Au(111) and Re(001) surfaces, LDOS profiles of these adsorbates for their free and adsorbed states, and the surface metal atoms on the adsorption sites of Au(111) and Re(001) surfaces for their bare and adsorbed state were analyzed. Additionally, CO-OH co-adsorption on Au(111) and Re(001) surfaces were carried out in order to analyze the reaction steps of WGS reaction on Au(111) and Re(001) surfaces. In the second part of the study, Au-Re surface alloys were generated by the addition of Au atoms on Re(001) surface as point defects. The adsorptions/co-adsorptions of CO and OH molecules on Au-Re(001) surface alloys having different Au concentration on Re(001) were carried out in order to understand the reason of high activity and selectivity of Au-Re/Ceria catalysts that are reported by Çağlayan and Aksoylu [6].

Chapter 2 involves a literature survey containing a brief introduction to fuel cell-fuel processor systems, water gas shift reaction, the catalysts employed in WGS reaction with experimental and computational studies and theory behind computational methods. The method of calculation is presented in detail on Chapter 3. The results obtained in the DFT calculation are discussed on Chapter 4 and the conclusions are given on Chapter 5.

2. LITERATURE SURVEY

2.1. Fuel Processor-Fuel Cell System

Fuel cell is a viable alternative for clean energy generation. Fuel Cell converts the chemical energy stored a fuel into electricity through a chemical reaction with oxygen. This technology is suitable for small scale stationary and mobile applications. The variety of applications for fuel cell technology ranges from portable/micro power and transportation applications to stationary power generation for buildings and distributed energy production. These new technologies or prototype vehicles adopting fuel cells intend to reduce atmospheric pollution. Various types of fuel cells having different porperties and application areas are either in use or under development: solid polymer fuel cells (SPFC), also known as proton-exchange membrane (PEM) fuel cells, operate at 80 °C, alkaline fuel cells (AFC) at 100 °C, phosphoric acid fuel cells (PAFC) at 200 °C operation, molten carbonate fuel cells (MCFC) at 650 °C, and solid oxide fuel cells (SOFC) are used for high temperature operations ranges between 800-1100 °C. PEM-FC is considered to be most promising fuel cell system as it possess a series of advantages for mobile power applications (vehicles) or for small stationary power units; they have (i) low operating temperature, (ii) sustained operation at high current density, (iii) low weight, (iv) compactness, (v) potential for low cost and volume, (vi) long stack life, (vii) fast start-ups, and (viii) suitability to discontinuous operation. On the other hand, the ideal fuel for PEM-FC is pure hydrogen since PEM-FC has stable activity only if the feed stream is hydrogen rich feed containing less than 50 ppm level of carbon monoxide, which is the poisoning limit of the Pt anode catalyst of the fuel cell. Therefore, it is necessary to use system that produce CO-free hydrogen from hydrocarbons before PEM-FC, namely a fuel processor (FP). It is shown in Figure 2.1 that three steps are carried out sequentially in a fuel processor. Depending on the reformer type, operating conditions and fuel, the outlet stream from the reformer contains 6–10% CO, which is further converted to hydrogen and carbon dioxide via the water-gas shift reaction. The water–gas shift reactor reduces the CO concentration to the degree of 0.5-1%. After that, the PROX unit reduces CO content below 50 ppm, which can be tolerated by PEM-FC [1]. As the current study focuses on WGS reaction in the fuel processor, primary focus is on WGS literature.

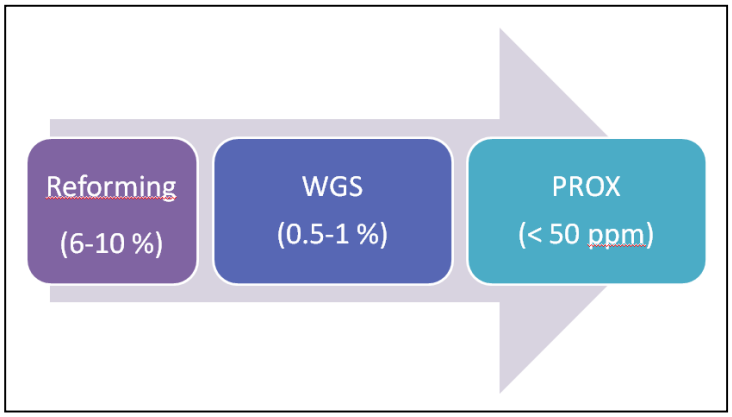

Figure 2.1. The Fuel Processor (FP).

2.2. Water-Gas Shift (WGS) Reaction

The feed stream to WGS reactor contains CO, CO_2, H_2 and water. WGS is a reaction in which carbon monoxide reacts with water to produce H_2 and CO_2:

$$CO_{(g)} + H_2O_{(g)} \leftrightarrow H_{2\,(g)} + CO_{2\,(g)} \qquad \Delta H = -41.2\ kJ.mol^{-1} \qquad (2.1)$$

In WGS reaction, CO and water are reactants, and CO_2 and H_2 are products, but in WGS reactor, there is a possibility of formation of intermediate species, such as OH, HOCO etc. [9]. The WGS reaction has a reversible nature; thus it attains equilibrium with the reverse WGS (RWGS) reaction. The WGS reaction is moderately exothermic, and its equilibrium constant increases as temperature decreases. In other words, the lower temperatures lead to an increase in the production of H_2. However, the higher temperatures may be needed to obtain necessary fast kinetics and high reaction rates. Therefore, a catalyst that is highly active at low temperatures is required for the intended applications [2].

2.3. Commercial Catalyst for WGS Reaction

To obtain high activity and conversion, WGS reaction is conventionally performed in two reactors operating in series: (i) a high temperature shift (HTS) reactor, and (ii) a low temperature shift (LTS) reactor.

The high-temperature shift (HTS) reactor operates at 350-450 °C range and provides the fast reaction kinetics. The CO concentration is reduced to about 3-4 volume per cent by high-temperature water-gas shift (HT-WGS or HTS) reaction. Conventional HT-WGS catalysts are based on iron-chromium (Fe-Cr) oxides and they have some advantages such as, low cost, long life and are reasonable sulfur resistance sulfur. The low-temperature shift (LTS) reactor operates at temperatures between 200 and 260 °C in order to take the advantage of the shift in the equilibrium to lower CO concentrations at lower temperatures. The CO concentration is reduced down to approximately 0.5-1 volume per cent with low-temperature water-gas shift reaction over Cu-Zn based catalyst [10, 11].

The technologies on production and purification of hydrogen have a great importance in the hydrogen–energy society. Water–gas-shift reaction will be one of the key technologies in the future. WGS is used in ammonia synthesis, in production and purification of hydrogen, and in the production of synthesis gas for adjusting the CO/H_2 ratio. Fe–Cr and Cu–Zn based catalysts are used in most of the industrial applications. Recently, there is a growing interest in onboard H_2 production for small scale mobile and immobile energy production via PEM fuel cells. Thus, the importance of WGS reaction has been increased in the area of small scale fuel processing and CO- free hydrogen production [12].

Current commercial large scale WGS technology involves multiple stages/catalysts, i.e. (i) HTS with (Fe_2O_3/Cr_2O_3) and (ii) LTS with ($Cu/ZnO/Al_2O_3$). On the other hand, these commercial catalysts are not suitable for small scale mobile or immobile fuel processing devices since they require special activation procedures (Long pre-conditioning), they are pyrophoric and intolerant of poisons, condensation, and oxidation, and they have thermodynamic limitations at high temperatures and have slow kinetics at low temperatures. Therefore, there is a need of developing a single/multi stage WGS catalyst that is sufficiently active at relatively low (HTS-LTS transition) temperatures for the intended applications, selective to CO conversion without catalyzing side reactions, such as methanation or hydrogen oxidation that would consume valuable hydrogen, thermally stable, and non-pyrophoric, and also has poison resistance steam tolerance, and coke resistance. Precious metal (PM) catalysts are popular in this case, as they are generally superior to base-metal catalysts for the long time use, high conversion, and high

selectivity. However, although many catalytic systems have been investigated, an effective commercial catalyst is still under development. Precious metals, such as Au, Pd, Pt or Re on different oxide supports, e.g. CeO_2, ZrO_2, and TiO_2, have been explored and reported to be effective for WGS [3].

2.4. Au-Based Catalysts for WGS Reaction

Since gold is the least reactive metal, it has been regarded as poorly active as a heterogeneous catalyst. In the past the gold catalysis was extensively studied, but it was stated that gold had been little used in practical heterogeneous catalysis. Haruta found that the chemistry of gold dramatically changes when gold is deposited on select metal oxides as ultra-fine particles. He showed that highly dispersed gold catalysts are really very active in many important reactions for chemical industry, such as CO oxidation. He signified that although the surface of gold is intrinsically inert, the catalytic nature of gold has been found to be tunable for many important reactions through the control of its particle size, the suitable selection of support materials, and the architecture of the metal-support interaction. It is indicated that the studies on gold based catalysts present future opportunities for industrial and environmental applications since it has the wide range in tunability of catalytic properties from oxidation to hydrogenation [13].

Gold catalysts show rapidly growing interest for WGS due to their high activity for CO oxidation at low temperature. Gold-particles supported on metal oxides, like CeO, TiO, Fe O have been reported active for WGS, and their improved activity at low temperature is explained through the synergism between gold and metal oxide support. Gold catalysts, however, are sensitive to the preparation condition since the desired properties of the final material depends on dispersion, gold particle size, and the intimate metal–support contact. The gold particle size can easily change during the reaction and strongly impact the activity [1].

Gold catalysis is a rapidly developing topic both in academic and industrial research and significant advances have been made within the last decade. In particular, it is interesting to note the increasing number of patents related to gold catalysts in polymer electrolyte membrane (PEM) fuel cell technology [14].

2.4.1. Experimental Studies

The initial activities of Ceria-supported Au catalysts are higher than those for a commercial Cu–Zn–Al catalyst for the WGS reaction, but there is deactivation of the Au/CeO_2 catalysts. Deactivation occurs due to the formation of carbonates and/or formates on the catalyst surface. Oxygen-deficient sites on the catalyst surface help the deposition of carbonates and/or formates. This implies that deactivation could be managed by conditioning of the CeO2 surface or the addition of constituents to minimize oxygen deficiency [15].

A catalytic study of the hydrogen production by CO water gas shift (WGS) reaction on gold, silver and copper particles supported on TiO2 has been carried out by Boccuzzi *et al.* Although silver catalyst exhibits no catalytic activity, copper and gold catalysts show intermediate and very high performances, respectively. These strong differences have been interpreted on the basis of both the FTIR data of CO adsorption at 90 K and the effect of coadsorbed species. Gold and copper catalysts, either oxidized or reduced, are able to adsorb CO, and the reduced gold catalyst activates CO molecules on surface step sites [16].

In the WGS reaction, gold and platinum catalysts supported on ZrO_2, CeO_2 and ZrO_2 are mostly investigated. It is shown that, at low temperatures, gold catalysis is more active than those based on platinum. The type and composition of the support is of great importance in promoting the activity of gold catalysts. Zirconia support is found suitable in synthesizing gold and platinum based WGS catalysts. In the case of platinum catalysts, the composition of support did not significantly affect the WGS activity. Zirconia has been found to be a very suitable support for gold since it favors the dissociation of water and strongly interacts with the gold particles to promote their capacity of adsorption and desorption of reactants involved in the reaction [17].

The high catalytic activity and stability in the WGS reaction is manifested by the gold catalysts on the basis of the well crystallized oxide support [18]. Tabakova *et al*. also investigated the impact of support composition on the performance of Au/CeO_2-Fe_2O_3 catalysts in WGS reaction. The gold particles were prepared via deposition-precipitation method on pure ceria, iron oxide and mixed Ce-Fe composite oxides. The activity order

Au/CeO_2 > $Au/Ce_{50}Fe_{50}$ > $Au/Ce_{75}Fe_{25}$ > $Au/Ce_{25}Fe_{75}$ > Au/Fe_2O_3 was observed. This tendency can be attributed to significant difference in gold particle size and in the ability of the supports to assist formation of oxygen vacancies [5].

In the study of Andreeva *et al.*, ceria supported gold catalysts, especially the ones with higher gold content, exhibit a high and stable activity for the WGS reaction. It is indicated that the high and stable activity of the catalysts is probably due to the high stability of the gold dispersion. The TPR results indicate that the reduction/oxidation processes take place readily in the presence of gold. Evidently, the sample $3Au/CeO_2$ has the optimal ratio between surface gold active centers and free ceria surface being capable to produce oxygen. In addition, catalytic activity of the catalysts slightly increased as a function of H_2O/CO ratio in the feed [19].

High activity and stability of low-content (0.2–0.9 at.%) gold–cerium oxide catalysts in water–gas shift reaction (WGS) was reported by Fu *et al.* They examined Au–ceria catalysts under realistic water–gas shift reaction conditions. They found that the number of active sites correlates well with the properties of the support oxide, namely the ceria surface area and crystallite size. The active sites for the WGS reaction on gold–ceria and on other potential Au-oxide systems, as well as other metals on ceria, are nonmetallic. Phases involving metal cations and the oxide support, M–O–Ce, appear to do the catalysis [4].

Rodriguez reported that for the gold-oxide support systems, one has a bifunctional catalyst: the adsorption and dissociation of water takes place on the oxide side while CO adsorbs on the gold nanoparticles, and all subsequent reaction steps occur at oxide-metal interface. Experimental evidence indicates that gold-oxide interface do catalyze the reaction between OH with CO to yield HOCO, HCOO or CO_3 intermediates, and then H_2 and CO_2 are produced [9].

The study on WGS mechanism on Au/Ceria catalysts is carried out by Tabakova *et al.* On the basis of their DRIFTS studies, in which they examined the interaction of ceria support and the catalyst with CO and H_2O, they conducted forward and reverse WGS reaction tests. They concluded that (i) forward reaction proceeded at the boundary between

small metallic gold particles and ceria, where CO adsorption on gold and H_2O dissociation on ceria took place on defects, (ii) formates were intermediates in WGS reaction, and (iii) the stability of Au/CeO_2 catalysts stemmed from the interactions between small gold metallic particles and ceria [20].

In kinetics and mechanistic study of Leppelt *et al.*, it is shown that Au/CeO_2 catalysts prepared via a modified deposition-precipitation process and exposed to reductive conditioning at 200 °C are highly active for the WGS reaction for an idealized reaction gas mixture and are also remarkably stable after an initial period. It is reported that a mechanism is deduced and proposed involving (i) direct CO adsorption on Au nanoparticles, as well as adsorption on an adjacent support area and subsequent reverse spillover on the Au particles; (ii) formation and decomposition of surface formates at active sites, such as at the interface of Au particles and CeO_2 support, by reaction of CO_{ad} and OH_{ad}, and their subsequent decomposition to CO_2 and H_2; and (iii) the spillover and reversible spillover of these species on the support and back [11].

The experimental and theoretical studies have shown that water dissociates on O/Au(111), yielding hydroxyls which react with CO to produce CO_2. Following the reaction mechanisms postulated in this study, the reaction of OH with CO can produce formate (HCOO), carboxyl (HOCO), and/or carbonate (CO_3) species as key intermediates before the final production of CO_2 and H_2. Although formates and carbonates have been detected in many experiments studying the WGS on metal/oxide catalysts, the HOCO intermediate is favored in DFT calculations for the WGS reaction on gold surfaces. Senanayake *et al.* reported that neither HCOO nor CO_3 was detected during the reaction of CO with OH on Au(111) at 90-120 K, and the results of photoemission and IR spectroscopy point to HO + CO interactions, consistent with the formation of an unstable HOCO intermediate which has a short lifetime on the gold surface [21].

2.4.2. Computational Studies

Density functional theory (DFT) is an important tool for computational chemistry and theoretical surface science. Computational simulation programs which utilize DFT, such as CASTEP, are useful for investigating surface properties, such as catalytically

active sites and metal alloys, in determining interaction between surface and adsorbates, and in identifying the reaction mechanisms.

The atomic structures of gold supported on (111) and (110) surfaces of CeO_2 have been studied using density-functional theory calculations. The total energy calculations are carried out using two DFT codes: VASP and SIESTA. A single Au atom is placed on two adsorption sites on the surfaces, i.e. an O-vacancy and a Ce-vacancy on both CeO_2(111) and CeO_2(110). The stability of Au adsorption is following the order: $E_{ad(Ce\text{-}vacancy)} > E_{ad(O\text{-}vacancy)}$. Au atom adsorption on a Ce-vacancy causes a large distortion on the surfaces: it creates an O-vacancy. The O atom near the Au atom becomes more reactive than that formed on stoichiometric surfaces [22].

The trends in CO adsorption on close-packed metal surfaces of Co, Ni, Cu from the 3d row, Ru, Rh, Pd, Ag from the 4d row and Ir, Pt, Au from the 5d row using density functional theory were studied by Gajdos *et al.* They were concerned with the trends in adsorption energy, geometry, vibrational properties and other parameters derived from the electronic structure of the substrate. It is reported that while the geometrical and vibrational properties of the adsorbate–substrate complex are calculated with high accuracy, the adsorption energies calculated with the gradient-corrected Perdew–Wang exchange–correlation (PW91) are overestimated. It is indicated that the analysis of density of states projected onto 1π, 2π, 5σ and 4σ molecular orbitals (LDOS) of a CO molecule on atop, bridge and hollow sites of Au shows that there is no principal difference between the Au and Pt DOS. It is also concluded that the weakly bonded CO molecules on the Au(111) surface already show the general interaction trends [23].

In spite of the well-known inertness of gold, a clear chemical interaction between CO and Au(111) is evidenced, through on-top chemisorption accompanied with surface restructuring. According to DFT calculations, chemisorption is favored at low-coordinated sites, with the classical trend: terraces < steps < kinks < adatoms. The DFT calculations of Piccolo *et al.* show that the adsorption on atop site is the most stable one between all surfaces on gold. They also reported that the C–O distance is slightly elongated (1.149 Å) upon chemisorption compared to the optimized gas phase molecule (1.142 Å) [24].

Adsorption of hydroxyl on the Au(110), Au(100), and Au(111) surfaces has been investigated by means of density functional based methods, by using both cluster models and periodic slabs by Pessoa *et al.* According to the cluster models, the final structures of adsorbed OH are upright and the preferred modes for its adsorption onto the Au(110), Au(100), and Au(111) surfaces are the short-bridge site with an adsorption energy of -1.96 eV, the bridge site with an adsorption energy of -0.79 eV, and the hollow hcp site with an adsorption energy of -1.25 eV. According to the periodic calculations, the final $(OH)_{ads}$ structures are in a few cases (i.e.: the bridge site) more tilted as compared to the cluster model results and OH has a different preferred adsorption site for the Au(111) surface, i.e. the bridge site. It is signified that the interaction of the OH radical with the gold surfaces is stable on all possible adsorption sites as a general conclusion. The analysis of the density-of-states indicates that the metal d-band and the O 2p orbital are heavily involved in the bonding mechanism [25].

A detailed density functional theory (DFT) investigation of Liu *et al.* revealed there are three possible mechanisms (redox mechanism, carboxyl mechanism, and formate intermediate mechanism) for the water-gas shift reaction on Au(111) surface. Adsorption energy of all the pertinent species (H_2O, CO, OH, O, H, CO_2, COOH, HCOO) are calculated, and their preferred adsorption sites are obtained. The reaction pathway containing 14 elementary steps is characterized and the reaction potential energy surfaces are calculated. The results of the study show that the carboxyl mechanism and the redox mechanism are feasible while the formate intermediate mechanism is unlikely because of its high formation barrier. It is also shown that the carboxyl mechanism is more probable compared with the redox mechanism and the most feasible reaction pathway is $\mathrm{H_2O} \xrightarrow{-\mathrm{H}} \mathrm{OH} \xrightarrow{+\mathrm{CO}} \mathrm{COOH} \xrightarrow{+\mathrm{OH}} \mathrm{CO_2}$ [26].

DFT-GGA calculations were employed by Liu and Rodriguez. on the study about WGS on Cu and Au systems including both surfaces and nanoparticles. Their results show that the WGS follows a redox mechanism on Cu(100), while the associative mechanism via a carboxyl intermediate is preferred for Au(100), Au_{29}, and Cu_{29}, but the rate limiting step for all of these systems is the same: water dissociation. This study proposes WGS mechanism on Au(100). CO adsorption is exothermic and the bridging sites are preferred

with a reaction energy of −0.54 eV, and H_2O molecules are weakly adsorbed at the top sites with −0.15 eV. The most energy-consuming step is water dissociation, there are several possibilities for the next step, where the reaction intermediates can be O, HCOO or OCOH. The calculated barrier and the corresponding transition state structures show that WGS should follow the associative mechanism via carboxyl intermediates. Through interaction with OH species, OCOH dissociates to yield CO_2 gas and adsorbed H_2O. The last step is the desorption of H_2, which is also a downhill reaction [27].

2.5. The Effect of Rhenium on WGS reaction

It is shown that Pt/TiO_2 and Pt/ZrO_2 catalysts have relatively high catalytic activity for LT-WGS. In order to examine the effects of Re addition to these catalysts, $Pt–Re/TiO_2$ (Rutile) and $Pt–Re/ZrO_2$ catalysts were prepared and characterized by TEM and XPS measurements. The reactivity of the adsorbed CO species with steam increased with the Re addition to Pt/ZrO_2 and Pt/TiO_2. It was reported that CO bonding is weakened by Re redox reaction. The results showed that the $Pt–Re/TiO_2$ catalyst has superior catalytic activity compared to a commercial Cu–Zn catalyst [28]. Iida *et. al.* also reported that Pt-Re catalysts are promising systems for new generation LT-WGS catalysts considering the superior activities of $Pt–Re/ZrO_2$ and $Pt-Re/TiO_2$ (Rutile) catalysts [29].

Pt/TiO_2 shows the highest intrinsic activity (TOF, s^{-1}), however, it was deactivated during time-on-stream tests. Pt sintering is the cause of deactivation. Deactivation can be overcome by adding Re to the catalyst. The stability of Pt/TiO_2 can be improved by adding Re, which prevents Pt sintering. In addition, the presence of Re increased the catalytic activity of Pt/TiO_2 [30]. The developed $Pt–Re/TiO_2$ catalyst shows excellent activity, selectivity to H_2 and stability. Since Re is present at least partly as ReO_x, it provides an additional redox route for WGS reaction through which ReO_x is reduced by CO generating CO_2 and it is re-oxidized by H_2O forming H_2. However, there is still a debate about the reason for the higher activity of $Pt–Re/TiO_2$ compared to Pt/TiO_2 [3].

WGS activity was increased by the addition of Re in both Pt/TiO_2 and Pd/TiO_2 catalysts. Different types of CO adsorption occurred upon the addition of Re, which are observed in the IR spectra taken after WGS reaction [12]. According to Sato *et al.* it is

generally accepted that addition of Re causes significant improvement in the catalytic activity. The one of the role of Re can be the stabilization of formate species and accelerating the rate of H_2 formation [31].

The relativistic density-functional calculations were carried out using the Amsterdam density functional (ADF) program package. CO adsorption and H_2O dissociation on a series of mixed Pt–M surface–vacuum interfaces (M= Ru, Sn, Mo, W, Re, Os, Rh, Ir, Cu, Zn, Ge, Pb, and Zr) were investigated. The adsorption of CO on binary Pt–M, except Cu and Pb, is weakened compared with pure Pt. Ru is better for dissociating H_2O into OH than Pt. Mo, W, and Re were found more active than Ru in adsorbing and dissociating H_2O. These metals not only weaken CO adsorption, but also promote H_2O dissociation. For Re, the activation energy for the $CO_{ads} + OH_{ads}$ combination reaction is the highest. Hence, the rate-determining step of the reaction becomes in CO removal [32].

The addition of Re to $Pt/Ce_{0.46}Zr_{0.54}O_2$ was shown to enhance the WGS rate compared with the WGS rate observed with $Pt/Ce_{0.46}Zr_{0.54}O_2$ for similar Pt weight loadings. The Pt dispersion was found higher on the Pt-Re catalysts than the Pt catalysts in CO chemisorption measurements. The WGS rate for both the Pt-Re and Pt catalysts was seemed to correlate with the exposed Pt surface area on the various catalysts; however, the enhancement in the rate was observed upon the addition of Re could not be completely explained by just the higher Pt dispersion [33].

The binding of atomic hydrogen on monometallic Pd(111), Re(0001), and bimetallic Pd_{ML} /Re(0001) and Re_{ML} /Pd(111) surfaces was analyzed with DFT-GGA periodic slab calculations by Pallassana *et al.* The binding of hydrogen is strongest on the Re surfaces, with a chemisorption energy of -2.82 eV for Re(0001) and -2.78 eV for Re_{ML} /Pd(111). Formal chemisorption theory was used to correlate the predicted binding energy with the location of the d-band center of the bare metal surfaces by using a model developed by Hammer and Nørskov. The analysis of adsorption energies computed by using DFT and the density of states (DOS) analysis conducted for the clean metal surfaces indicates that there is a clear correlation between the d-band center of the surface metal atoms and their hydrogen chemisorption energy [34].

Chayakul *et al.* investigated that the catalytic activities of Re–Co/CeO_2 bimetallic catalysts for the water gas shift (WGS) reaction, and compared their activities with the activity of Co/CeO_2. It was found WGS reaction rate over Re–Co/CeO_2 bimetallic catalysts is higher than that of monometallic Co on ceria. XRD and Raman spectroscopy results indicate that metal oxides are dispersed on ceria surface and H_2-chemisorption indicates better dispersion of Co on the ceria surface upon addition of Re. It was also reported that Re withdraws electron density from Co and lowers the back-donation of d-electron from cobalt to π orbital of adsorbed CO molecules, and the Co-adsorbate bonds are weaker and thus the CO_2 product can easily leave the catalyst surface. It seems that Re presence influences the catalyst properties and performance in several ways. Re increases the reducibility of the surface ceria, and facilitates the redox process at the surface. Re also increases the metal active sites available for WGS reaction and weakens the active metal-adsorbate bonds. All of these effects contribute to an increase in the WGS reaction rates [7].

The results of reaction kinetics measurements and characterization studies indicated that Pt and Re are in close contact in Pt–Re/C catalysts. Kunkes *et al.* reported that Re alters the Pt surface. One of the effects of Re in Pt–Re catalysts is to weaken the strength of CO adsorption. Since the binding energies of oxygen atoms and hydroxyl groups are stronger on Re than on Pt, the effect of Re on the catalytic properties of Pt-Re based catalysts may be caused by the presence of oxygen species, for example hydroxyl groups, associated with Re atoms on the surface of Pt–Re particles. These –OH groups on Re may also react with CO adsorbed on neighboring Pt sites, leading to the formation of the reactive intermediate species for the water–gas shift reaction on Pt. In addition, the –OH group on Re may serve as a hydrogen transfer agent for reaction with hydroxyl groups [8].

2.6. Au-Re Catalyst

Many research groups have reported that Re can improve the activity of catalysts in various reactions when it is used as a second metal. CATREL (Catalyst Technology and Reaction Engineering Laboratory) is the first group that conducted a study on WGS performance of ceria supported Au-Re. Çağlayan and Aksoylu investigated water gas shift activity under ideal feed conditions on ceria supported Au, Re, and Au-Re catalysts.

Au/ceria, Re/ceria and Au–Re/ceria catalysts were prepared by using deposition precipitation and impregnation techniques for Au and Re addition, respectively, except the sample prepared by sequential impregnation. It was shown that Re/ceria catalyst is not active in WGS. Au addition by dp technique on impregnated Re/ceria catalysts (Au-Re/ceria) led to a higher dispersion and, consequently, higher CO conversion values. On the other hand, impregnation of Re on Au/ceria catalysts resulted in slight blockage of active sites and poor WGS activity. Therefore, the application sequence of the impregnation and dp methods, which were used in Re and Au addition, respectively, was found crucial. They explained this significant activity difference between the two catalysts prepared by (imp+dp) and (dp+imp) with surface alloy formation and/or interaction between Au and Re atoms since Au–Re bulk alloy formation requires very high temperatures. The results indicate that novel Au–Re/ceria catalysts are highly active for WGS reaction, especially at high H_2O/CO ratios, led by the presence of catalytically active and steam tolerant sites formed on the bimetallic catalyst [6].

2.7. Theory Behind Computational Methods

Theoretical models that have been developed to calculate molecular structure and energetics are divided into two categories: quantum chemical models and molecular mechanics models.

Quantum chemical models are ultimately derived from the Schrodinger equation. It treats molecules as collections of nuclei and electrons, without any reference to chemical bonds. However, approximations need to be made to solve the Schrodinger equation for more than one electron systems. Quantum chemical models differ in the nature of these approximations. Actually, the quantum chemical model is defined as a set of approximations to Schrodinger equation.

The first one of these is the Hartree-Fock approximation that provides the foundation for the so-called Hartree-Fock molecular orbital models, or simply molecular orbital models. The Hartree-Fock approximation assumes that electrons move essentially as independent particles, without interacting with each other. The instantaneous interactions between individual electrons in this model are replaced by interactions between a particular electron and the average field created by all the other electrons. The failures of Hartree-Fock models

can be traced to an incomplete description of "electron correlation" or simply stated, the way in which the motion of one electron affects the motions of all the other electrons. Two fundamentally different approaches for improvement of Hartree-Fock models have emerged.

One approach is to construct a more flexible description of electron motions in terms of a combination of Hartree-Fock descriptions for ground and excited states. Configuration interaction (CI) and Moller-Plesset (MP) models are the two of the most commonly used models of this type. The second-order Moller-Plesset model (MP2) is the most practical and widely employed.

An alternative approach to improve upon Hartree-Fock models involves including an explicit term to account for the way in which electron motions affect each other. In practice, this account is based on an "exact" solution for an idealized system, and is introduced by using empirical parameters. The resulting models are referred to as density functional models.

The Hartree-Fock approximation also provided the basis for semi-empirical models. These models introduce additional approximations as well as empirical parameters to greatly simplify the calculation, with minimal adverse effect on the results. While this goal has yet to be fully realized, several useful schemes have found effective, included the popular AMI and PM3 models.

The alternative to quantum chemical models is so-called molecular mechanics models. These do not start from an "exact-theory" (the Schrödinger equation), but rather from a simple but chemically reasonable picture of molecular structure. In this picture, the molecules are made up of atoms and bonds (as opposed to nuclei and electrons), and atom positions are adjusted to best-match known structural data (bond lengths and angles), as well as to accommodate non-bonded interactions. This is much simpler than solving the Schrödinger for electron motions, but requires an explicit description of chemical bonding, as well as a large amount of information about the structures of molecules [35].

2.7.1. Schrödinger Equation

All quantum mechanical models ultimately trace back to Schrödinger equation, which is written for the special case of the hydrogen atom as such:

$$\left[-\frac{1}{2}\nabla^2 - \frac{Z}{r}\right]\psi(r) = E\psi(r) \qquad (2.2)$$

Here, the quantity in square brackets represents the kinetic energy and potential energy of an electron at a distance r from a nucleus of charge Z. There, E is the electronic energy, and ψ which is a function of the electronic coordinates, r, is a wave function describing the motion of the electron as fully as possible. Wavefunctions for the hydrogen atom are the familiar s,p,d… atomic orbitals [36].

2.7.2. Density Functional Models

One approach to the treatment of electron correlation is density functional theory developed by Hohenberg and Kohn (1964) and Kohn and Sham (1965). Both exchange and correlation effects are included in DFT.

Density functional models have at their heart the electron density, as opposed to the many-electron wavefunction, Ψ(r1, r2,…). Hohenberg and Kohn proved that the total energy, including exchange and correlation, of an electron gas (even in the presence of a static external potential) is a unique functional of the electron density. If the true exchange correlation functional can be used, DFT theoretically would give the exact solution, however the exact exchange-correlation functional required for this purpose is unknown. The minimum value of the total-energy functional is the ground-state energy of the system, and the density that yields this minimum value is the exact single-particle ground-state density. Kohn and Sham then extended the theory to practice by showing how the energy can be partitioned into kinetic energy, potential energy and electron-electron repulsion terms and showed how it is possible, formally, to replace the many-electron problem by an exactly equivalent set of self-consistent one-electron equations.

The energy is written as:

$$E = E_T + E_V + E_J + E_{XC} \qquad (2.3)$$

where E_J is the Hartree Coulomb term for electron-electron interaction, which does not include exchange and correlation effects and E_V is the electron-nuclear interaction energy. The electron energy is given by E_T. E_{XC} is the exchange and correlation energy. Except from E_T, all others depend on the total electron density, $\rho(r)$.

$$\rho(r) = 2 \sum_{i}^{\text{orbitals}} |\psi_i(r)|^2 \tag{2.4}$$

where ψ_i are the Kohn-Sham orbitals and the summation is carried over pairs of electrons.

Only the minimum value of the Kohn-Sham energy functional has physical meaning. At the minimum, the Kohn-Sham energy functional is equal to the ground-state energy of the system of electrons. Minimizing E with respect to the unknown orbital coefficients yields a set of matrix equations, the "Kohn-Sham equations". These are n Schrödinger-like equations for n non-interacting electrons moving in an effective potential. In the KS equations, the effective potential is the Kohn-Sham potential, which is defined as the functional derivative,

$$V_{KS}(r) = \frac{\delta}{\delta\rho(r)}\left(E_J[\rho(r)] + E_{XC}[\rho(r)]\right) = V_H(r) + \frac{\delta E_{XC}[\rho(r)]}{\delta\rho(r)} \tag{2.5}$$

Defining the exchange-correlation potential, V_{xc}, formally by the functional derivative,

$$V_{XC}(r) = \frac{\delta E_{XC}[\rho(r)]}{\delta\rho(r)} \tag{2.6}$$

Then, it is obtained:

$$\left[-\frac{1}{2}\nabla^2 + V_{ion}(r) + V_H(r) + V_{XC}(r)\right]\psi_i(r) = \varepsilon_i\psi_i(r) \tag{2.7}$$

where ψ_i is the wave function of electronic state i, ε_i is the Kohn-Sham eigenvalue, and V_H is the Hartree potential of the electrons.

Finding a functional E_{XC} that handles the complexity of interacting electrons remains the great challenge in DFT. There are two major approximations to solve this problem. The most widely used is the local-density approximation (LDA), which was introduced by Kohn and Sham along with KS equations. The LDA states that E_{XC} can be given by assuming that the exchange-correlation energy is that of a uniform electron gas of density $\rho=\rho(r)$. Then,

$$E_{XC} = \int dr\, \rho(r)\varepsilon_{XC}\big(\rho(r)\big) \tag{2.8}$$

where $\varepsilon_{xc}(\rho)$ is the exchange-correlation energy per electron in a uniform gas of density ρ. However in reality, the charge density is highly non-uniform around the atoms. Functionals that have been developed including dependence on the gradient of the density are called generalized-gradient approximation (GGA).

The set of wave functions that minimize the Kohn-Sham energy functional are given by the self-consistent solutions to the Kohn-Sham equations. The Kohn-Sham equations must be solved self-consistently so that the occupied electronic states generate a charge density that produces the electronic potential that was used to construct the equations. At the process, the first step is to estimate a V_{KS}. Then this potential is used in Equation 2.7 to solve for the wave function, ψ_i. The found wave functions are used to calculate the density via Equation 2.4. Finally, the density is used to calculate a new V_{KS}. The iteration continues until V_{KS} and density converge [36, 37].

3. CALCULATION

3.1. The Materials Studio Software

3.1.1. MS Visualizer

DFT calculations in this study are performed in a repeated slab geometry by Materials Studio (MS version 5.0) of Accelrys Inc. MS Visualizer is used to construct and modify graphical models of molecules, organic and inorganic crystals, polymers, amorphous materials, metal surfaces and layered structures. MS Visualizer contains the essential modeling functionality required to support computational materials science, and provides the information about properties or processes related to molecules and materials. It is integrated with special DFT codes, like CASTEP, for energy calculations.

3.1.2. MS CASTEP

CASTEP is an *ab-initio* quantum mechanical program employing density functional theory (DFT) to simulate the properties of solids, interfaces, and surfaces for a wide range of material classes, such as ceramics, semiconductors, and metals. First principle calculations provide to investigate the nature and origin of the electronic, optical, and structural properties of a system without the need for any experimental input.

Originally developed in the Theory of Condensed Matter Group at Cambridge University, UK, CASTEP uses quantum mechanical calculations to study problems in chemicals and materials research. It is used in the field of surface chemistry, physi- and chemisorption, and heterogeneous catalysis to predict the structure of a material as well as many essential properties, such as molecular geometry, lattice constants, electronic structures, and density-of-states.

CASTEP uses a total energy plane-wave pseudopotential method. In the mathematical model of the material, CASTEP replaces core electrons with effective potentials acting only on the valence electrons in the system. Electronic wavefunctions are

expanded through a plane-wave basis set, and exchange and correlation effects can be included within either the local density (LDA) or generalized gradient (GGA) approximations. Combining the use of pseudopotentials and plane wave basis sets enable extremely efficient geometry optimizations of molecules, solids, surfaces, and interfaces. The primary reason that CASTEP has become so powerful is that the numerical methods used to solve the underlying quantum mechanical calculations are both computationally efficient and extremely accurate [37].

3.2. Computational Details of CASTEP

Our DFT calculations were performed for a repeated slab geometry, using the program package CASTEP in Materials Studio (version 5.0) of Accelrys Inc. Periodic boundary conditions generate a pair of two-dimensionally infinite surfaces, separated by a substantial slab of material in one direction and on the other by a vacuum region. The metal slab in Au and Re cases consists of 3 layers. The positions of the atoms present at the uppermost 2 layers were relaxed together with the adsorbate, while the positions of the atoms of remaining 1 bottom layer was kept fixed in their ideal bulk geometry. The gap between neighboring slabs is 14 Å.

The electron-ion interaction was included through the use of ultrasoft pseudopotentials and the electronic wave functions involved were expanded in a basis set of plane waves. Exchange and correlation energy and the potential were included through the use of generalized gradient approximation (GGA) along with the PBE (Perdew-Burke-Ernzerhof) functional. No spin-polarization effects were included in the exchange-correlation functional.

In order to determine the optimum values of kinetic energy cutoff and k-points sampling for Au and Re cases, Au and Re bulks were optimized with different kinetic energy cutoff (from 320 eV up to 380 eV) and k-points sampling (4x4x4, 6x6x6 and 8x8x8). In Au case, for kinetic energy cutoff, it was seen that the differences of total energy result between 320-340 eV, 340-360 eV, and 360-380 eV are around 0.09, 0.01, and 0.006 eV, respectively. For k-points sampling, it was seen that the differences of total energy result between 4x4x4 and 6x6x6, and 6x6x6 and 8x8x8 are around 0.14 eV and

0.04 eV, respectively. After the comparative analysis of accuracy-convergencetime combinations for different cut-off and k-point sampling values, the optimum kinetic energy cutoff and k-points sampling for Au surface were determined as 340 eV and 6x6x6, respectively. Likely, for Re bulk geometry optimization 340 eV and 6x6x4 were determined as the optimum kinetic energy cutoff and k-point sampling values for Re surface.

The calculations were carried out within (2x3) super cells, so sampling of the (2x3) Brillouin zones of Au and Re metal surfaces were achieved by summation over Monkhorst-Pack meshes of dimensions 3x2x1. Pulay's density mixing scheme was used for the SCF electronic minimization. A smearing range of 0.1 eV was applied at the Fermi level and 20% empty bands were introduced to speed up the convergence. The convergence criteria for structure optimizations were 1.0 × 10−6 eV/atom for SCF, 1.0 × 10−5 eV/atom for energy, 0.03 eV/Å for maximum force, and 1.0 × 10−3 Å for maximum displacement. The energy was corrected by extrapolation to zero temperature.

3.3. Optimizing Bulk Au and Re

In order to build up a surface with MS Visualizer, the first step is to optimize the bulk structure of the material. The bulk crystal structure of a material can be imported from MS library if the material is monometallic, or can be prepared manually depending on the experimental data if the material is not involved in the database. For this study, Au and Re bulk crystal structures imported from MS library. Bulk Au has a face-centered cubic crystal structure, while bulk Re has a hexagonal close-packed crystal structure. The ball-and-stick models of bulk Au and Re are given in Figure 3.1 The geometry of the bulk Au and Re was optimized by CASTEP with the selected parameters given in Section 3.2. During the geometry optimization, the position of atoms are arranged in order to minimize the total energy. Total energy of a molecule or a crystal refers to the energy of a specific arrangement of atoms. The zero of the energy is taken to be the infinite seperation of all electrons and nuclei, so the total energy is generally negative.

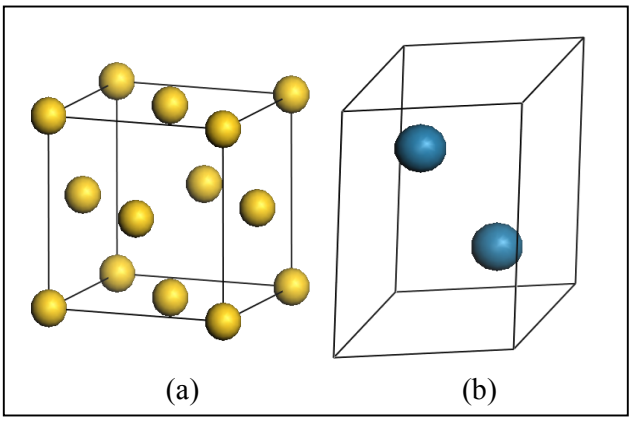

Figure 3.1. The visual models of (a) Au and (b) Re unit cells.

3.4. Building and Optimizing the Au(111) and Re(001) Surfaces

The process of creating the surface has two steps. The first step is to cleave the surface and the second one is to build up a vacuum slab containing the surface.

In the first step, the cleaving was performed by entering the Miller indices of the surface into the specific dialog box and then, specifying the thickness of the slab that is the number of atomic layers in the slab. In this study, since gold has a face cubic centered crystal structure, (111) Miller indices was selected for Au surface, considering the DFT studies of gold [9] and the HR-TEM image of the experimental study of Çağlayan and Aksoylu [6]. On the other hand, Rhenium has hexagonal close-packed crystal structure, so it is presented in Bravais-Miller index, which has the four numbers (h, k, i, l). In this system, h, k and ℓ are identical to the Miller index, and i is a redundant index (i=-h-k). According to the DFT studies of Rhenium, (0001) surface was selected [34], and (0001) was converted to Miller index as (001). For a reasonable computational time, the thickness of the slab was determined as three layers for both of Au and Re surfaces.

The slab has to include a sufficiently thick vacuum layer above the surface, so that there was no attraction between the topside and the underside of the surface. On the other hand, one must be careful to choose the appropriate values because of the proportionality between the computational time and the thickness of the slab. In the second step, the thickness of the vacuum layer separating the two surfaces was determined as 14 Å.

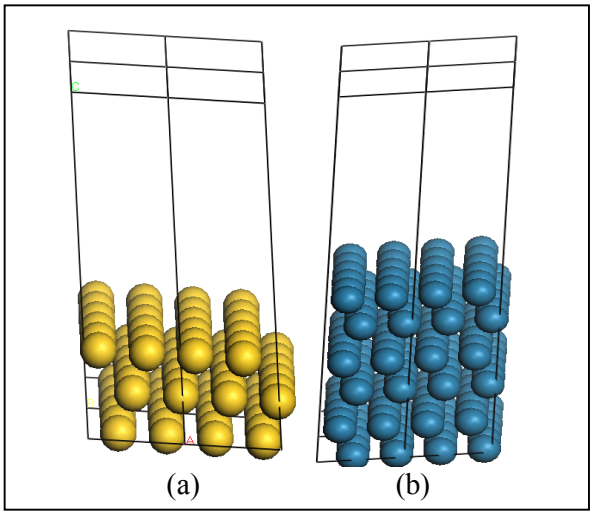

Figure 3.2. The visual models of (2x3) slabs for (a) Au(111) and (b) Re(001) surfaces.

For the adsorption, (2x3) super cells were used in generating slabs of Au(111) and Re(001) surfaces. To decreases computational time, the two top layers of the slab were relaxed, while the atoms in remaining bottom layer were constrained at their bulk positions. The final slabs of Au(111) and Re(001) surfaces are shown in Figure 3.2.

3.5. Calculating the Adsorption Energies

DFT calculations make systematic (but unknown) errors relative to the true solution of the Schrödinger equation because of the approximate nature of the exchange-correlation functional. However, a very broad body of calculations has shown that: *if two DFT calculations compare "chemically similar" states, then the systematic errors in these two calculations are also similar.* In other words, relative energies of chemically similar states can be calculated much more accurately with DFT than absolute energies. Adsorption on surface gives a concrete example of this general principal. If the relative energy of an adsorbate in a site is calculated, then it is certainly reasonable to describe these as chemically similar. Therefore, it is expected that a good level of accuracy in this relative energy [38].

Adsorptions were performed on Au(111) and Re(001) at three possible adsorption sites, atop, bridge and threefold. A constant surface coverage was used as 1/6 ML. Adsorbates (such as CO, OH, H_2O and CO_2) were bonded to atoms at adsorption sites with reasonable ends. For example, OH was bonded with its oxygen end, and CO was bonded with its carbon end. The initial distance between adsorbate and surface was taken 1.5 Å [39]. After an adsorbate molecule is bonded to a possible adsorption site with its reasonable end, geometry optimization is performed. During the geometry optimization, the position of atoms are arranged in order to minimize the total energy.

Adsorption energies were obtained by using this equation [40]:

$$E_{ads} = E_{system} - (E_{adsorbate} + E_{surface}) \quad (3.1)$$

where E_{ads} is the adsorption energy of the adsorbate at that site, E_{system} is the total energy of the optimized adsorption complex, $E_{adsorbate}$ is the total energy of the optimized adsorbate molecule, and $E_{surface}$ is the total energy of the optimized bare surface. The total energy of bare Au(111) and Re(001) surfaces were found as -16445.35 and -88532.33 eV. The total energies of the adsorbates used this study are given in Table 3.1.

Table 3.1. Adsorbates and their total energies ($E_{adsorbate}$).

Adsorbates	$E_{adsorbate}$ (eV)
CO	-590.11
OH	-449.20
H_2O	-468.72
CO_2	-1027.91
H	-12.52
trans-HOCO	-1041.54
cis-HOCO	-1041.41

3.6. Calculating the Surface Energies of Au-Re Surfaces

The stability of the Au-Re bimetallic surfaces were compared based on their surface energy for both monometallic surfaces and bimetallic surfaces. The surface energy ($E_{surface}$) was calculated according to the following formula [36]:

$$E_{surface} = \frac{E_{slab} - N_{Au}E_{bulk}^{Au} - N_{Re}E_{bulk}^{Re}}{2A} \quad (3.2)$$

where A is the surface area of the unit cell of the slab, E_{slab} is the total energy per unit cell of the slab, E_{bulk} is the total energy per unit cell of the bulk crystal of metal and N is the number of atoms in the unit cell of the slab. The factor 2 reflects the presence of two surfaces in the slab. E_{bulk}^{Au} and E_{bulk}^{Re} was obtained as -3655.47 and -4919.20 eV. The surface area of the unit cell of the Re(001) slab was calculated as 40.37 $Å^2$.

3.7. LDOS Profiles

Local density of states (LDOS) is a useful semi-qualitative tool for analyzing electronic structure. LDOS profiles show the electron density of an atom for given energy levels. CASTEP uses a simplified linear interpolation scheme developed by Ackland (1998). This method is based on linear interpolation in paralelopipeds formed by the points of the Monkhorst-Pack set, followed by the histogram sampling of the resultant set of band energies. Smearing method is employed with a width of 0.2 eV. Profiles are produced by plotting the LDOS (electrons/eV) versus energy (eV) [41].

LDOS analysis was performed for metal atom(s) on Au(111) and Re(001) surfaces for their bare and coordinated states as well as for atom of coordination of adsorbates for their free and coordinated states in order to understand how adsorbate and metal atom(s) at the adsorption sites interact further. LDOS profiles show the probabilistic electron density of an atom for the given energy levels, and the comparative changes in the energy level and amplitude of the electron density peaks/profiles observed between the LDOS of uncoordinated (bare metal or free adsorbate) and coordinated structures indicate the presence and extent of electronic interaction between adsorbate and metal surface.

4. RESULTS AND DISCUSSIONS

The experimental tests performed on investigating characterization and WGS activity and selectivity of Au-Re/CeO_2 system show that the catalyst has Au-Re surface alloys and it has superior activity and selectivity in WGS reaction. Additionally, it retains its high activity level for high steam concentrations in the feed stream. As the catalyst has sequential addition of Re followed by Au precursors, Au-Re mixed layers are formed on Re clusters. In this study, the steps of WGS reaction was investigated at atomic scale through studying the adsorptions of its reactants, products and possible intermediate species on Au(111), Re(001) and Au-Re(001) surfaces by using DFT calculations in CASTEP in order to understand how Au-Re surface alloy functions during the reaction.

Firstly, the adsorption energies of CO, OH, CO_2, H_2O, HOCO molecules and H atoms on Au(111) and Re(001) surfaces, LDOS profiles of these adsorbates for their free and adsorbed states, and the surface metal atoms on the adsorption sites of Au(111) and Re(001) surfaces for their bare and adsorbed states were analyzed. Additionally, CO-OH co-adsorption studies on Au(111) and Re(001) surfaces were carried out in order to analyze the reaction steps of WGS reaction on Au(111) and Re(001) surfaces.

In the second part of the study, Au-Re surface alloys were generated by the addition of Au atoms on Re(001) surface as point defects. The adsorption/co-adsorption of CO and OH molecules on Au-Re(001) surfaces that have different Au concentration, i.e. surface alloys, in order to understand the reasons of high activity and selectivity of Au-Re/Ceria catalysts that are reported by Çağlayan and Aksoylu [6].

4.1. Au(111) Surface

The Au(111) surface is modeled by a (2x3) unit cell. The slab is modeled with 3 layers for which the coordinates of the atoms at bottom layer is fixed. The Au(111) surface is shown in Figure 4.1, and possible adsorption sites on Au(111) surface is shown in Figure 4.2. The details of adsorption studies performed on Au(111) surface are summarized in Table 4.1.

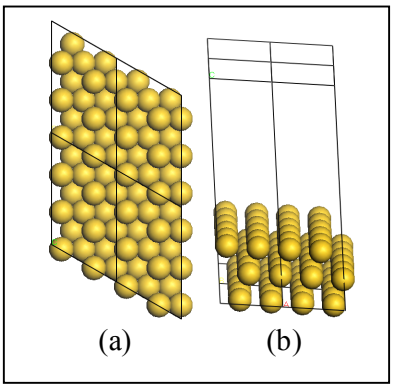

Figure 4.1. Top view (a) and side view (b) of Au(111) surface.

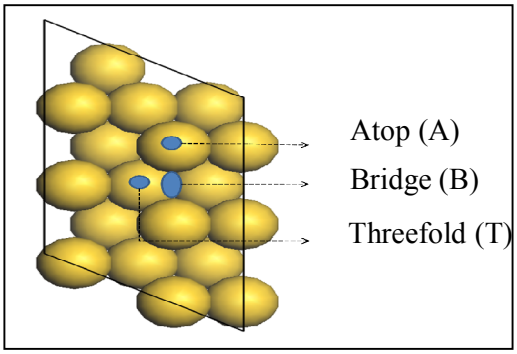

Figure 4.2. The possible adsorption sites on Au(111) single crystal surface: A, B and T.

Table 4.1. The adsorption studies on Au(111) with the adsorbates and adsorption sites.

Metal Name	Surface	Size	Adsorbate	Adsorption Site	Adsorption ML
Au	(1 1 1)	(2x3)	CO	A, B, T	1/6
Au	(1 1 1)	(2x3)	OH	A, B, T	1/6
Au	(1 1 1)	(2x3)	H_2O	A, B, T	1/6
Au	(1 1 1)	(2x3)	CO_2	A, B, T	1/6
Au	(1 1 1)	(2x3)	H	A, B, T	1/6
Au	(1 1 1)	(2x3)	cis-HOCO	A	1/6
Au	(1 1 1)	(2x3)	OH-CO co-ads	OH-A, CO-A	1/6, 1/6
Au	(1 1 1)	(2x3)	OH-CO co-ads	OH-B, CO-B	1/6, 1/6

4.1.1. CO Adsorption on Au(111)

CO is one of the reactants of WGS reaction, and its interaction with both active sites and reactant/reaction intermediates dominantly determines WGS surface reaction mechanism. CO adsorption on the possible adsorption sites (Atop-A, Bridge-B and Threefold-T) of Au(111) at a constant surface coverage of 1/6 ML were studied. For each one of three possible sites shown in Figure 4.2, one CO molecule was placed on Au(111) surface through following the method mentioned in Chapter 3, i.e. the initial distance between carbon of CO and metal surface is used as 1.5 Å, for which the CO molecule is bonded to Au atom(s) from its carbon end with a perpendicular orientation to the surface. The adsorption energy, the distance between C atom of CO and metal surface, and the bond length in CO molecule upon CO adsorption are shown in Table 4.2.

Table 4.2. Adsorption sites (Site), adsorption energy (E_{ads}), distance between C of CO and metal surface ($d_{C\text{-}Surface}$), and bond length in CO molecule ($d_{C\text{-}O}$) upon CO adsorption on Au(111).

CO adsorption on Au(111)			
Site	**E_{ads} (eV)**	**$d_{C\text{-}Surface}$ (Å)**	**$d_{C\text{-}O}$ (Å)**
A	-0.334	2.053	1.159
B	-0.539	1.427	1.181
T	-0.561	1.336	1.189

All CO adsorptions on A, B and T sites are stable with adsorption energies, -0.334, -0.539 and -0.561 eV, respectively. The lowest CO adsorption energy indicates the most energetically favored adsorption site for CO. The most favored site for CO adsorption is site T, and the second energetically preferred CO adsorption site is B. Their binding energies are close each other, and higher than that for A site. Piccolo *et al*. reported the binding energy of CO on top Au(111) as -0.34 eV in their DFT calculations [24]. In general, CO is weakly adsorbed on all three sites of the Au(111) surface as indicated by the low binding energies, and in terms of binding energies, the adsorption strength sequence of three possible sites is T > B > A. Gajdos *et al.* reported that CO molecules are weakly bonded on the Au(111) surface [23].

The sequence of the adsorption strength is consistent with the corresponding distance values found between C atom of CO and metal surface upon energy optimization (Table 4.2). There the distance between CO and coordinated site is defined as the distance between center of coordinated metal atom and center of C for adsorption at atop site, and the distance between the plane passes through at centers of coordinated metal atoms and center of C for multifold adsorption sites. As an example, CO adsorbed on site T with the lowest binding energy is the closest one to metal surface. Additionally, the bond length of free CO is obtained 1.154 Å, and as both the interaction strength between adsorbate and surface, and increase in number of coordination of CO with Au weaken the molecular bond between C and O, the bond length in CO molecule upon adsorption (Table 4.2) increases.

In Figure 4.3, the visual model of optimized CO adsorption at A, B and T sites on Au(111) are shown. It is seen that CO molecules are binding to the metal surface from their carbon end and still keep their perpendicular geometry to the metal surface upon energy optimization.

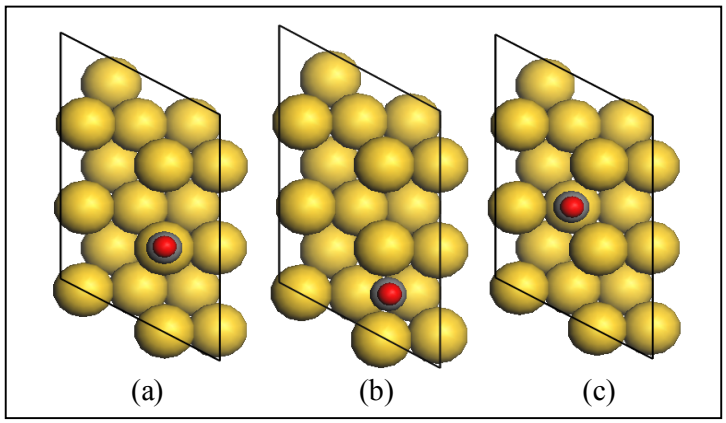

Figure 4.3. The top views of optimized CO adsorption on (a) site A, (b) site B, and (c) site T on Au(111).

In order to understand how CO and metal atoms at the adsorption sites interact further, LDOS analysis was also performed for Au atom(s) on the surface for their bare and coordinated states as well as for carbon end of CO for its free and coordinated states. LDOS profiles show the probabilistic electron density of an atom for the given energy levels, and the comparative changes in the energy level and amplitude of the electron

density peaks/profiles observed between the LDOS of uncoordinated (bare Au or free CO) and coordinated structures indicate the presence and extent of electronic interaction between adsorbate and metal surface.

In the comparison of LDOS profiles of bare and atop CO adsorbed states of Au atom, a significant change in the d-band center observed upon CO adsorption (Figure 4.4a). CO adsorption on B and T sites also leads to notable shifts in the d-band of Au atom. The changes in the d-bands center of Au atoms in CO coordinated state upon adsorption indicate that there is considerable interaction between CO and the Au surface. Figure 4.4-b shows the changes in LDOS of Au atom in threefold CO coordinated state compared to that of its bare state. The comparison of the changes in LDOS of Au atom in atop CO coordinated (Figure 4.4a) and Au atom in threefold CO coordinated states (Figure 4.4b) shows that there is less electron density shift for the threefold coordinated site, as there are three Au atoms are coordinated with CO molecule at threefold site, and the electron density shift is given only for one of the three Au atoms in Figure 4.4b.

The chemisorption of CO on transition metal surface was studied by Hu *et al*. They divided the molecular orbitals of CO into three groups: (i) the first group, containing only the 3σ orbital, hardly interacts with the metal d-bands due to low energy level, and is essentially not involved in chemisorption, (ii) the second group, containing the 4σ and lπ orbitals, is mixed with the metal d-bands during adsorption, and the peaks in LDOS coming from the 4σ and lπ orbitals are shifted downwards in energy. However, the net contribution to the chemisorption energy from these orbitals is very small since all the mixed orbitals have energy levels below Fermi level, (iii) the third group, containing the 5σ and 2π orbitals, is strongly mixed with the metal d-bands during adsorption to produce unfilled antibonding states above Fermi level, which provide significant net bonding to the surface [42]. In addition, Lynch and Hu reported that the significant contributions to bonding arise from the 5σ and 2π orbitals, with the contribution of the 5σ decreasing with high coordination of the CO molecule and the contribution of the 2π increasing with high coordination [43]. Gajdos *et al.* reported that there is no principal difference between the Au and Pt in LDOS analysis of CO adsorption [23].

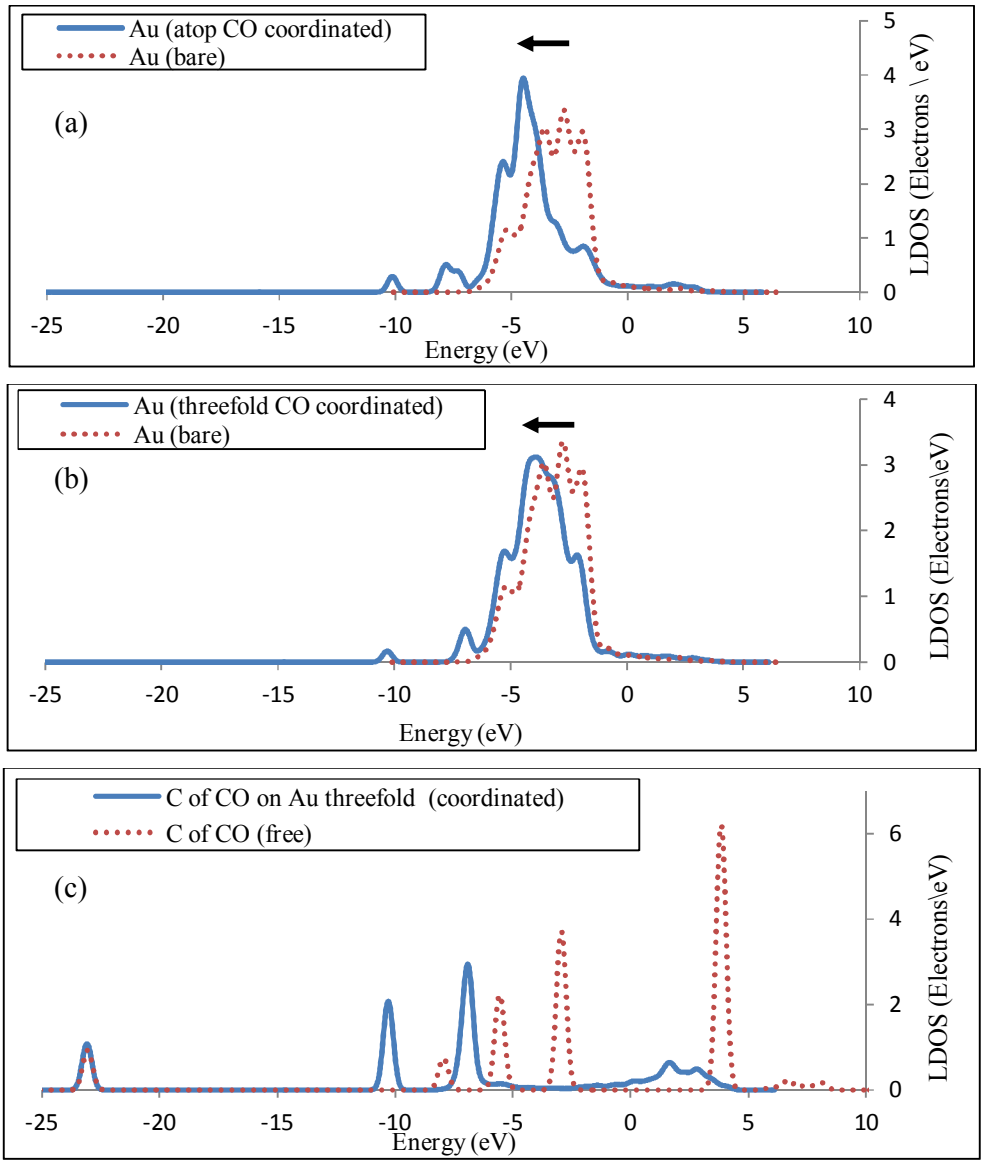

Figure 4.4. LDOS of (a) d-states of Au atom for its bare and atop CO coordinated states, (b) d-states of Au atom for its bare and threefold CO coordinated states, and (c) C of CO for its free and threefold coordinated states.

In Figure 4.4c, there are three distinct electron-rich regions along the energy scale for carbon end of the threefold coordinated CO. The first peak at -23 eV corresponds to the 3σ orbital which do not interact with the metal d-bands, and there is no change in this orbital upon adsorption. The second peak around -10 eV is the 4σ-derived orbital. The next peaks at -7 eV belong to the 1π-derived orbital. LDOS profiles of CO free and coordinated states

are significantly different at energy levels correspond to 4σ and 1π orbitals, proving the electronic interaction between CO molecule and the Au surface. The most significant contribution comes from the 5σ molecular orbital (around -3 eV in Figure 4.4c), as the peak was vanished upon adsorption.

The notable changes in the energy level and amplitude of the peaks observed between the LDOS profiles of uncoordinated and coordinated states for both Au and CO and the low adsorption energies found in CO adsorption for all three adsorption sites on Au indicate that CO adsorption is stable but weak on the Au surface. This result supports that CO, as a reactant of WGS, is adsorbed on Au active sites during the reaction.

4.1.2. OH Adsorption on Au(111)

One of the products of H_2O dissociation is surface OH and its function has significant importance in WGS surface reaction. OH adsorption was studied on the possible adsorption sites (Atop-A, Bridge-B and Threefold-T) of Au(111) surface at a constant surface coverage of 1/6 ML. For each one of three possible sites shown in Figure 4.2, one OH molecule was placed perpendicular to the surface with O-end attached to Au atom(s) at the site prior to energy optimization. The adsorption energy, the distance between O atom of OH and metal surface, and the bond length in OH molecule upon OH adsorption are shown in Table 4.3 for all adsorption sites.

Table 4.3. Adsorption sites (Site), adsorption energy (E_{ads}), distance between O of OH and metal surface ($d_{O\text{-}Surface}$), and bond length in OH molecule ($d_{O\text{-}H}$) upon OH adsorption on Au(111).

OH on Au(111)			
Site	**E_{ads} (eV)**	**$d_{O\text{-}surface}$ (Å)**	**$d_{O\text{-}H}$ (Å)**
A	-2.204	1.98	0.983
B	-2.460	1.628	0.983
T	-2.262	1.484	0.981

OH adsorption on A, B and T sites are stable with the adsorption energies of -2.204, -2.460 and -2.262 eV, respectively. The lowest OH adsorption energy indicates the most energetically favored adsorption site for OH. According to the adsorption energies in Table 4.3, the most energetically favored OH adsorption site is site B, which was also reported as the most energetically favored site of OH-adsorption on Au(111) by Pessoa *et al* [25]. It is seen that A and T sites are the second energetically preferred adsorption sites following site B with very close OH adsorption energy levels. It is conclued that the high OH adsorption energy on all sites of Au(111) indicate strong interaction between OH molecule and the Au surface. In addition, the binding energies of OH on Au are higher than to those of CO on Au. This signifies that OH has the stronger interaction with Au surface than that of CO.

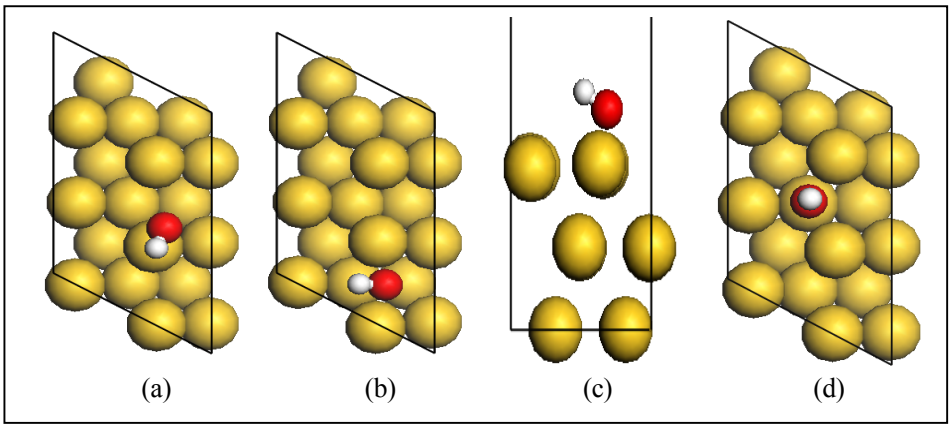

Figure 4.5. The visual models of optimized OH adsorption on (a) site A -top view-, (b) site B -top view-, (c) site B -side view-, and (d) site T -top view- on Au(111).

Although the sequence of the adsorption strength is not consistent with the corresponding distances between O atom of OH and metal surface upon OH adsorption (Table 4.3), it is consistent with the number of coordination of OH with surface Au atoms. Namely, OH on site T, which has higher the coordination number with OH, is the closest one to metal surface. Another interesting fact to be mentioned is the decrease in O-H bond length upon adsorption. Although there is a strong OH-surface interaction, the bond lengths in OH molecules upon adsorption decrease compared to its free state value of 0.991 Å. This can be explained by the additional interaction between the H atom of OH

with surface indicated by a tilted geometry of OH on A and B sites upon adsorption, i.e. H is getting close to surface for those sites (Figure 4.5a,b).

In Figure 4.5, the visual models of optimized OH adsorption on A, B and T sites. As expected, OH is bound to the surface from its oxygen end. It is seen that OH molecules on A and B sites are tilted upon adsorption, but OH on site T keeps its perpendicular orientation to the metal surface upon adsorption. It should be noted that if, at the beginning of energy optimization, OH on site T is not placed perpendicular to surface, i.e. if OH is placed tilted on site T, it diffuses towards site B, which was found as the most energetically favored OH adsorption site of Au(111). The result is consistent with the findings reported in Pessoa *et al.* [25].

In order to understand how OH and metal atoms at the adsorption sites interact further, LDOS analysis was also performed for Au atom(s) on the surface for their bare and coordinated states as well as for oxygen end of OH for its free and coordinated states. In the energy optimized LDOS profiles of OH adsorbed on A, B and T sites, notable shifts are observed in the center of d-band of Au atom on which OH adsorbed compared to that of LDOS of bare Au atom. In Figure 4.6a, LDOS profiles of Au atom for its bare and bridge type CO-coordinated states are shown. The arrow indicates shift towards lower energy. It is seen that there is less electron density shift for the OH coordinated Au at the bridge site as there are two Au atoms are coordinated with OH molecule at bridge site, and electron density shift is given for only one of the Au atoms (Figure 4.6a). The changes in d-band of OH coordinated Au atoms upon adsorption indicate that there is a considerable interaction between OH and the Au surface.

The adsorption of OH on transition metal surface was studied by Hu and Nakatsuji. According to their studies, 1π and 3σ orbitals of OH mix strongly with metal d-bands during adsorption which leads to bonding and anti-bonding levels, while 2σ orbital does not mix with the metal d-states [44].

In Figure 4.6b, it is seen that there are three distinct electron-rich regions 2σ, 3σ and 1π along the energy scale for oxygen end of free OH. The first peak at -19 eV corresponds to the 2σ orbital which does not interact with the metal d-band, and there is no change in

the electron density of this orbital upon adsorption. The peaks around -6 eV and -3 eV are the 3σ and 1π orbitals of free OH, respectively. These peaks were shifted and lowered in amplitude while got broadened upon adsorption, and the resultant derived orbital upon mixing with metal d-states has strong metallic character, i.e. continuous electron density, in ca. (-8)-(0) eV range with rather small local peaks at -1 eV and -7 eV. The significant change in the LDOS profiles of coordinated Au and OH compared to their LDOS profiles of uncoordinated states, respectively, at energy levels corresponds to that of 3σ and 1π molecular orbitals proves the strong electronic interaction between OH molecule and the Au surface.

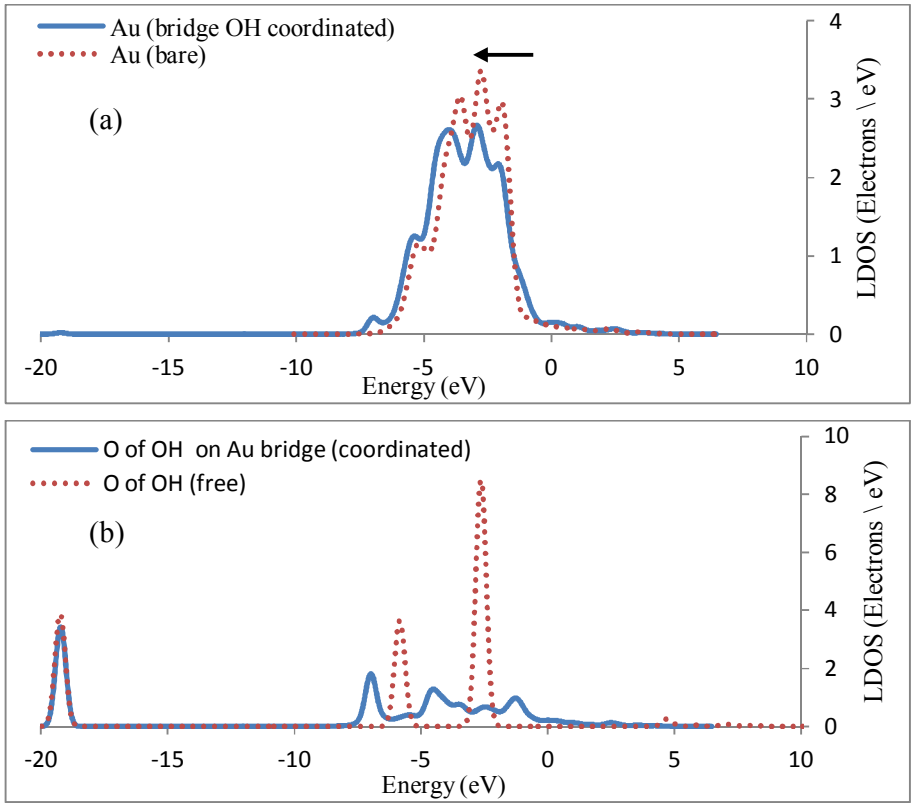

Figure 4.6. LDOS of (a) d-states of Au atom for its bare and bridge OH coordinated states and (b) O of OH for its free and bridge coordinated states.

The significant changes between the LDOS profiles of both coordinated Au and OH compared to that of their uncoordinated states and low adsorption energies calculated for all three sites show OH-adsorption is strong and stable on Au surface. During WGS

reaction, OH, which is the product of water dissociation, is the reaction intermediate interacting with the active sites of the catalysts. The results of OH and CO adsorption on Au are consistent with experimental evidence indicating gold-metal oxide support interfaces catalyze the reaction between OH and CO to produce intermediates which furtherly yields H_2 and CO_2 [9].

4.1.3. H_2O Adsorption on Au(111)

H_2O adsorption on possible adsorption sites (Atop-A, Bridge-B and Threefold-T) of Au(111) for a constant surface coverage of 1/6 ML were studied. Prior to the energy optimization, one H_2O molecule was placed on Au(111) surface with the initial distance between the oxygen of H_2O and metal surface is 1.5 Å, and H_2O molecule is bonded to metal surface from its oxygen end for each one of three possible sites shown in Figure 4.2. The adsorption energy, the distance between O atom of H_2O and metal surface, the bond lengths and the bond angle in H_2O molecule upon H_2O adsorption on each possible adsorption site of Au(111) are shown in Table 4.4.

Table 4.4. Adsorption sites (Site), adsorption energy (E_{ads}), distance between O of H_2O and metal surface ($d_{O\text{-}Surface}$), bond lengths ($d_{O\text{-}H}$) and bond angle (H-O-H) in H_2O upon H_2O adsorption on Au(111).

H_2O on Au(111)				
Site	**E_{ads} (eV)**	**$d_{O\text{-}surface}$ (Å)**	**$d_{O\text{-}H}$ (Å)**	**H-O-H (°)**
A	-0.129	2.75	0.979	104.8°
B	-0.083	3.206	0.979	104.7°
T	-0.099	3.024	0.979	104°

H_2O adsorption on A, B and T sites are stable with the adsorption energies, -0.129, -0.083 and -0.099 eV, respectively. The adsorption energy values indicate that the most favorable adsorption site is A, which is consistent with the findings by Liu *et al.* [26]. However, the binding energies are close to each other and very close to zero for all those three sites, and water moves away from the surface to a distance around 3 Å upon energy optimization (Figure 4.7). The O-H bond lengths and the H-O-H angles (Table 4.4) upon

adsorption are also very similar to those of free H_2O molecule, which are 0.977 Å and 104.53°, respectively. These calculated values of the bond length and the angle of free H_2O are consistent with the experimental values for gaseous water molecule, 0.96 Å and 104.474°, respectively [45].

In Figure 4.7, the initial and final structures of H_2O upon adsorption on site A are shown. It is seen that H_2O molecule moves away from the metal surface and is stabilized 3 Å away the surface. Additionally, the orientation of water molecule changes from its initial perpendicular orientation to flat and parallel-to-surface orientation at the end of energy optimization (Figure 4.7b,c.). This is agreeable with the studies of Liu *et al.* They investigated WGS mechanisms on Au(111) with DFT calculations, and they reported that H_2O is adsorbed flat with respect to the surface [26]. The evaluation of calculated values together with the change observed in the orientation of water molecule at the end of energy optimization reveal that the interaction between water and Au(111) surface is very weak, but still exists.

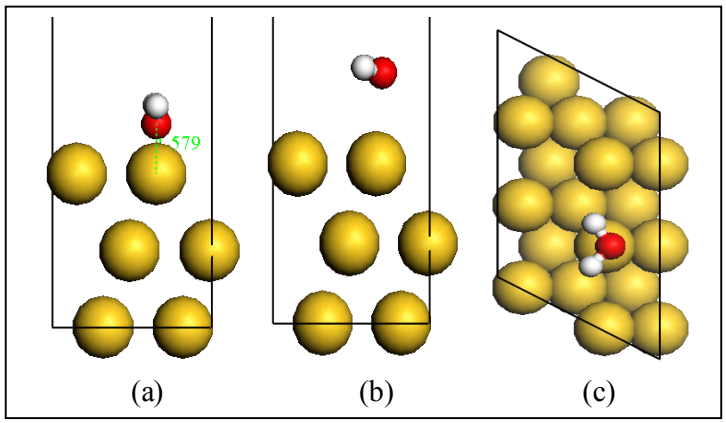

Figure 4.7. The visual models of H_2O adsorption on site A of Au(111): (a) side view prior to energy optimization, (b) side view upon energy optimization, and (c) top view upon energy optimization.

In order to understand how H_2O and metal atoms at the adsorption sites interact further, LDOS analysis was also performed for both Au atom(s) on the surface for their bare and coordinated states and for oxygen end of H_2O for free and coordinated states of H_2O. As can be seen in Figure 4.8, the changes in the energy level and amplitude of the

peaks present in the LDOS profiles of bare Au and free H_2O upon adsorption on all possible A, B and T sites are very small. This reveals that there is a very limited electronic interaction between adsorbate H_2O and metal surface, and the adsorption is very weak. It should be noted that though there is a very limited change in LDOS profile of bare Au upon adsorption at site A, the LDOS profiles of bare and bridge type coordinated Au are fully matched.

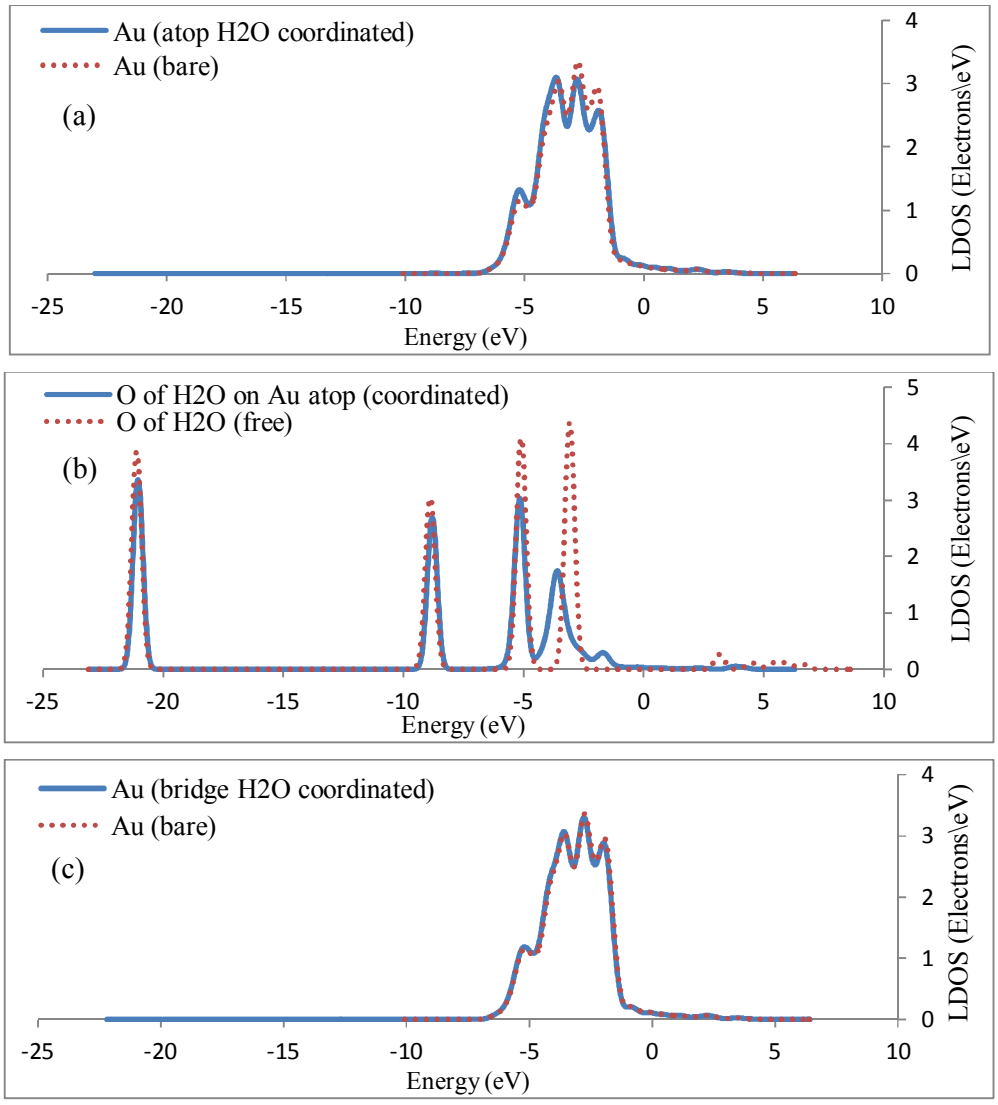

Figure 4.8. LDOS of (a) d-states of Au atom for its bare and atop H_2O coordinated states, (b) O of H_2O for its free and atop coordinated states, and (c) d-states of Au atom for its bare and bridge H_2O coordinated states.

The results of CO, OH and water adsorptions studies on Au(111) are consistent with the previous data reported on gold base catalyst for WGS. Rodriguez reported that the results of DFT calculations point to a very high barrier for the dissociation of H_2O on Au(111), which leads to negligible activity for the WGS process, but in the gold-metal oxide systems, the catalyst is bifunctional: there, adsorption and dissociation of water takes place on the metal oxide support used, like CeO_2, while CO adsorbs on the gold nanoparticles, and all subsequent reaction steps occur at oxide-metal interface [9].

4.1.4. CO_2 Adsorption on Au(111)

CO_2 is one of the products of WGS reaction and its interaction with the active sites is of great importance. CO_2 adsorption studies on the possible adsorption sites (Atop-A, Bridge-B and Threefold-T) on Au(111) for a constant surface coverage of 1/6 ML were performed. For each one of three possible sites shown in Figure 4.2, one CO_2 linear molecule was placed parallel to the Au(111) surface prior to the energy optimization calculations with the initial distance between the carbon of CO_2 and metal surface is 1.5 Å, and CO_2 molecule is bonded to metal surface from its carbon atom. The adsorption energy, the distance between C atom of CO_2 and metal surface, the C-O bond lengths and O-C-O angle upon CO_2 adsorption on Au(111) are shown in Table 4.5 for adsorption at each site.

Table 4.5. Adsorption sites (Site), adsorption energy (E_{ads}), distance between C of CO_2 and metal surface ($d_{C\text{-}Surface}$), bond lengths ($d_{C\text{-}O}$) and bond angle (O-C-O) in CO_2 upon CO_2 adsorption on Au(111).

CO_2 on Au(111)				
Site	**E_{ads} (eV)**	**$d_{C\text{-}surface}$ (Å)**	**$d_{C\text{-}O}$ (Å)**	**O-C-O (°)**
A	0.001	3.446	1.181	179.2°
B	-0.020	3.564	1.181	179.9°
T	-0.025	3.709	1.181	179.9°

The results indicate that there is no energetically favorable CO_2 adsorption site on Au(111). As reported in Table 4.5, the binding energies of CO_2 adsorption on A, B and T sites are very close to zero, 0.001, -0.020 and -0.025 eV, respectively, and the distance

between the CO_2 and the Au surface upon adsorption increase from 1.5 to 3.5 Å, i.e. CO_2 moves away from the metal surface. In addition, the linear structure of CO_2 was preserved upon adsorption; the O-C-O bond angle, 179.2 °, for adsorption on all sites indicates planar geometry, and C-O bond length of free CO_2 molecule - which is calculated as 1.181 Å, and is close to experimental value of 1.160 Å by Pan *et al.* [46] - do not change at all upon adsorption. As an example, the initial and energy optimized structure of CO_2 upon adsorption on site A are shown in Figure 4.9a,b. It is seen that CO_2 molecule moves away from the metal surface while keeping its linear geometry. The results obtained from CO_2 adsorption study on Au revealed that CO_2 adsorption is unstable on Au(111).

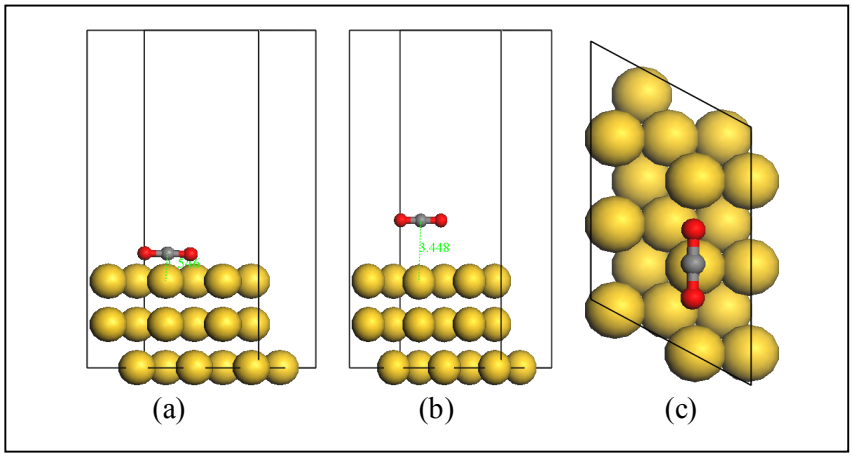

Figure 4.9. The visual models of CO_2 adsorption on site A of Au(111): (a) side view prior to energy optimization, (b) side view upon energy optimization and (c) top view upon energy optimization.

In order to understand whether there is any electronic interaction between CO_2 and metal atoms at the adsorption sites, LDOS profiles of Au atom(s) on the surface for their bare and coordinated states and of carbon end of CO_2 for its free and coordinated states were obtained and comparatively analyzed. As can be followed from Figure 4.10, the changes in the energy level and amplitude of the peaks present in the LDOS of bare Au and free CO_2 are negligible upon adsorption on site A, and this is also valid for adsorption at bridge and threefold sites. The results show that there is no electronic interaction between CO_2 and Au metal surface. This result is perfectly consistent with the conclusion that CO_2 adsorption on Au(111) is unstable and CO_2 molecule desorbs from the surface.

This result confirms that CO_2, as a product of WGS reaction, is fully desorbs from Au active sites of the catalyst during reaction without any site occupation and/or product inhibition.

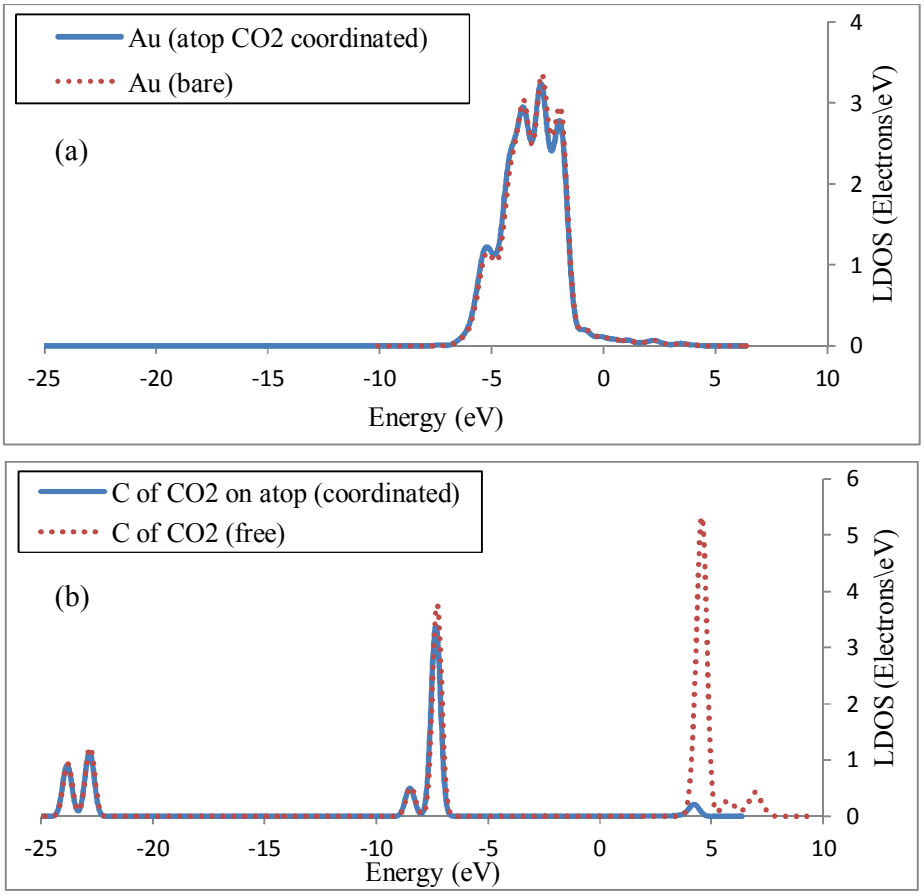

Figure 4.10. LDOS of (a) d-states of Au atom for its bare and atop CO_2 coordinated states and (b) C of CO_2 for its free and atop coordinated states.

4.1.5. H Adsorption on Au(111)

The dissociation of H_2O on the metal oxide support sites produces two reaction intermediates, H and OH, during WGS reaction. The type and extent of interaction between those intermediates and the active sites should be analyzed in order to shed a light on the surface mechanism. H adsorption studies on the possible adsorption sites (Atop-A, Bridge-B and Threefold-T) of Au(111) for a constant surface coverage of 1/6 ML were performed. For each one of three possible active sites shown in Figure 4.2, one H atom was

placed on Au(111) surface. The adsorption energy and the distance between H atom and Au metal surface upon H adsorption are shown in Table 4.6 for each adsorption site.

Table 4.6. Adsorption sites (Site), adsorption energy(E_{ads}), and the distance between H atom and metal surface ($d_{H\text{-}Surface}$) upon H adsorption on Au(111).

H on Au(111)		
Site	**E_{ads} (eV)**	**$d_{H\text{-}surface}$ (Å)**
A	-3.025	1.611
B -> T	-3.405	0.627
T	-3.356	0.733

H adsorption is stable on sites A and T with adsorption energies of -3.025 and -3.405 eV, respectively. For H adsorption on site B, H atom moved towards threefold site at the end of energy optimization. As the lowest adsorption energy indicates the most energetically favored adsorption site, the most favored site for H adsorption according to the adsorption energies in Table 4.3 is site T. It is seen that site A is the second energetically preferred adsorption site. The high adsorption energies of H at A and T sites of Au(111) indicate the strong interaction between H atom and the Au surface. According to the last column of Table 4.6, H atom is closest to the surface for site T, which has the highest strength of adsorption. Results revealed that adsorption strength increases with the increase in number of coordination of H atom with surface Au atoms. The visual models of optimized H adsorption at sites A and T are shown in Figure 4.11. It is seen that H atoms are perfectly stable at sites A and T of the metal surface.

The interaction between H and Au atom(s) at the active sites was investigated further through the use of LDOS analysis. There, LDOS of bare and H-coordinated Au atoms as well as those of free and coordinated H atoms were comparatively evaluated. There is a significant shift observed in the center of d-band of Au atom upon atop H adsorption (Figure 4.12a). Similarly, LDOS profile of Au atom in H coordinated state show a notable shift in the d-band compared to LDOS of bare Au atom. The changes in the center of d-bands of H coordinated Au atoms upon adsorption indicate that there is a considerable interaction between H and the Au surface. Figure 4.12b shows the changes in LDOS of

threefold H coordinated Au atom compared to that of its bare state. A comparison of the changes in LDOS of Au atoms on which H is coordinated atop and threefold (Figure 4.12a,b) shows that there is less electron density shift for the Au atom at the one leg of threefold adsorption, since at threefold site three Au atoms are coordinated with H atom, and electron density shift is given for only one of three Au atoms.

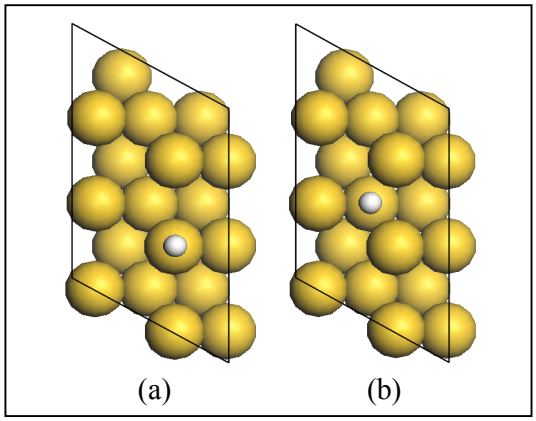

Figure 4.11. The top views of optimized H adsorption
(a) on site A and (b) on site T on Au(111).

The principal bonding in H adsorption on transition metal comes from the interaction between 1*s* electron of H atom and d-electrons of transition metal. Although there is a significant shift in energy coupled with a change in amplitude at d-band of Au atom upon atop H adsorption, no splitting of d-band is observed (Figure 4.12a). On the other hand, though the shift in energy for the d-band is rather limited for Au atom present at one of the legs of threefold H-adsorption, d-band split at ca. (-7)-(-9) eV, corresponding to the energy level of H-electron density upon adsorption (Figure 4.12c), is observed. This is consistent with stronger H adsorption on site T than on site A. Qi *et al.* reported the split off phenomenon for d-states as was found in their DFT study involved H adsorption for different surface concentrations on Pd; there, no d-band split is reported for atop H adsorption [47]. Strong interaction between H and Au surface, as in the case of threefold adsorption, reveals itself in the significant shift of electron density in energy, from ca. 0 eV to ca (-8) eV, coupled with disappearance of peak at ca. 0 eV.

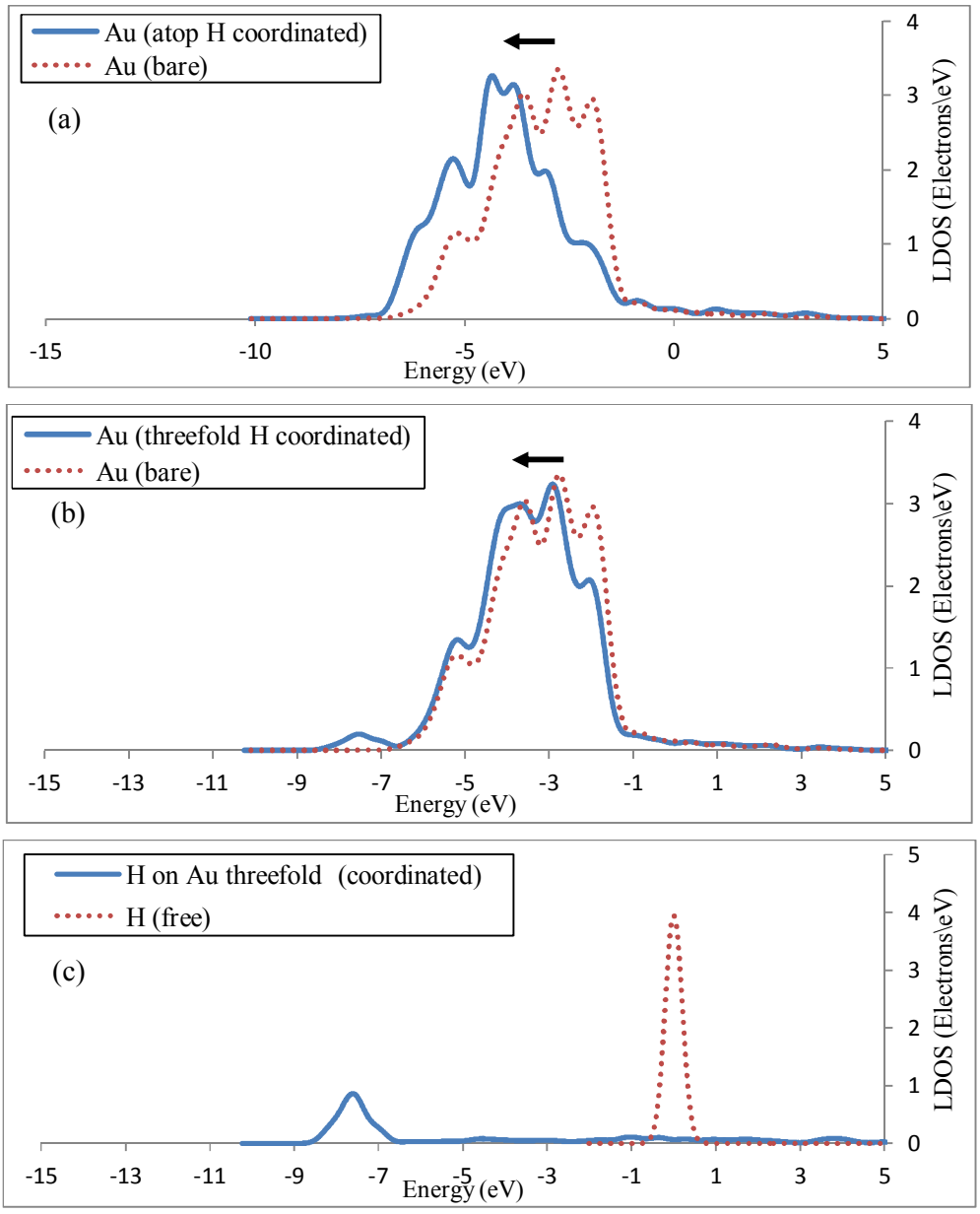

Figure 4.12. LDOS of (a) d-states of Au atom for its bare and atop H coordinated states, (b) d-states of Au atom for bare threefold H coordinated states, and (c) H atom for its free and threefold coordinated states.

The results clearly indicate that H adsorption is stable and strong at A and T sites on the Au surface.

4.1.6. CO-OH Co-adsorption on Au(111)

According to the literature on WGS reaction over Au/metal oxide catalyst, the adsorption and water dissociation steps take place on the support metal oxide. There, water is dissociated to OH and H on the surface of the oxide support, such as ceria, and CO adsorbs on the gold surface. All subsequent reaction steps following adsorption occur at Au-support interfaces. Experimental evidence indicates that gold-oxide interfaces do catalyze the reaction between OH and CO to yield reaction intermediates, from which H_2 and CO_2 are produced [9]. On the basis of these information, surface CO and OH are considered as the reactants to form any intermediate species of WGS reaction.

CO and OH co-adsorption was studied on Au(111) for two different co-adsorption combinations considering stability/adsorption strength of individual CO and OH on the possible adsorption sites of Au(111). Surface coverage of CO and OH were taken as 1/6 ML for each. In CO-OH co-adsorption system, total surface coverage is 1/3 ML. For first co-adsorption configuration, OH and CO were placed on atop sites, whereas for second one, both of them were placed on bridge sites. The energy optimized forms of both coadsorption configurations clearly indicate the formation of cis-HOCO species through CO-OH interaction, (shown in Figure 4.13 and Figure 4.14), which is reported as the intermediate species for the carboxyl mechanism of WGS reaction on Au(111) by Liu *et al.* [26].

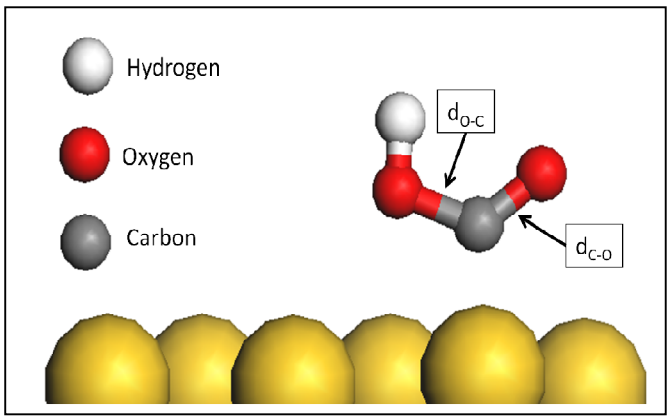

Figure 4.13. The visual model of the carboxyl (cis-HOCO).

Table 4.7. Co-adsorption sites (Site), adsorption energy (E_{ads}), and distance between the carbon of HOCO and Au atom ($d_{C\text{-}surface}$) upon CO-OH co-adsorption.

CO-OH co-adsorption on Au(111)		
Site	**E_{ads} (eV)**	**$d_{C\text{-}surface}$ (Å)**
CO-A, OH-A	-3.981	2.111
CO-B, OH-B	-3.993	2.103

For both CO-OH co-adsorption combinations, the total adsorption energy of the co-adsorption, which can be taken as the formation energies of HOCO molecule, and the distance between Au atom and the carbon of HOCO molecule formed are shown in Table 4.7. The formation energy of HOCO molecule is around -4 eV for each coadsorption combination. The highly negative adsorption energy values indicate that the formation of HOCO through CO-OH interaction on the surface is energetically favorable.

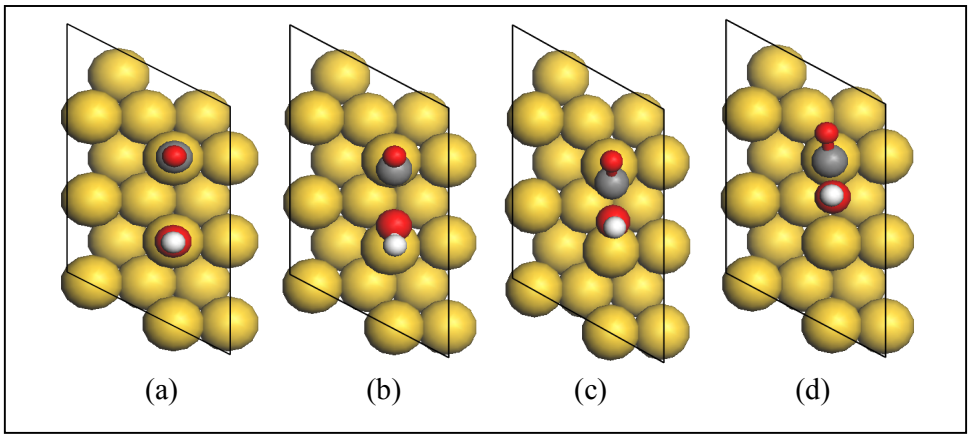

Figure 4.14. The visual models of CO-OH co-adsorption on Au(111) during energy optimization: (a) initial, (b) and (c) intermediates, and (d) final stages.

The positions and movement of CO and OH molecules at the initial, intermediate and final stages of energy optimization are given in Figure 4.14. There, CO and OH are at their initial positions in Figure 4.14a, i.e. CO and OH adsorbed atop, and in the energy optimized structure the HOCO molecule is formed as shown in Figure 4.14d. As can be

followed from Figure 4.14 that, CO and OH get close to each other during energy optimization scheme, form HOCO molecule, and HOCO moves to Au atop position.

In order to confirm whether CO and OH formed the carboxyl (HOCO), the adsorption of HOCO molecule on Au atop site was simulated through binding its carbon end to surface Au atom. A comparative analysis of the H-O, O-C, C-O bond lengths, H-O-C and O-C-O bond angles of HOCO molecule and C-Au distance (Table 4.8) for both HOCO formed through CO-OH coadsorption and HOCO molecularly adsorbed Au-atop clearly shows the values perfectly matches with each other confirming the formation of WGS reaction intermediate HOCO through CO-OH surface interaction on Au(111).

LDOS analysis was also performed for Au atom on the surface for its bare and coordinated states as well as for carbon end of HOCO for its free and coordinated, CO-OH co-adsorption, states. The notable shift of the d-band of CO-OH coadsorption-coordinated Au atom compared to its bare state (Figure 4.15a) as well as significant changes in both amplitude and energy levels of coordinated C of CO-OH coadsorbed state compared to that of C of HOCO for the free state (Figure 4.15b) clearly show that there is a strong interaction between CO-OH and the Au surface. It is worth to mention that LDOS of carbon of C-atop coordinated HOCO molecule, which is formed at the energy optimized CO-OH coadsorption structure (Figure 4.15b), and LDOS of carbon of HOCO molecule adsorbed atop are almost exactly the same, proving HOCO molecule is formed through CO and OH interaction on Au surface for their coadsorbed state.

Table 4.8. The values of bond lengths and angles of HOCO on Au atop (upon CO-OH co-adsorption) and HOCO on Au atop (upon HOCO adsorption).

	d_{H-O} (Å)	**d_{O-C} (Å)**	**d_{C-O} (Å)**	**H-O-C (°)**	**O-C-O (°)**	**$d_{C-surface}$ (Å)**
HOCO on Au atop (CO-OH co-adsorption)	0.991	1.214	1.358	107.231	123.904	2.111
HOCO on Au atop (HOCO adsorption)	0.991	1.215	1.356	106.988	124.01	2.107

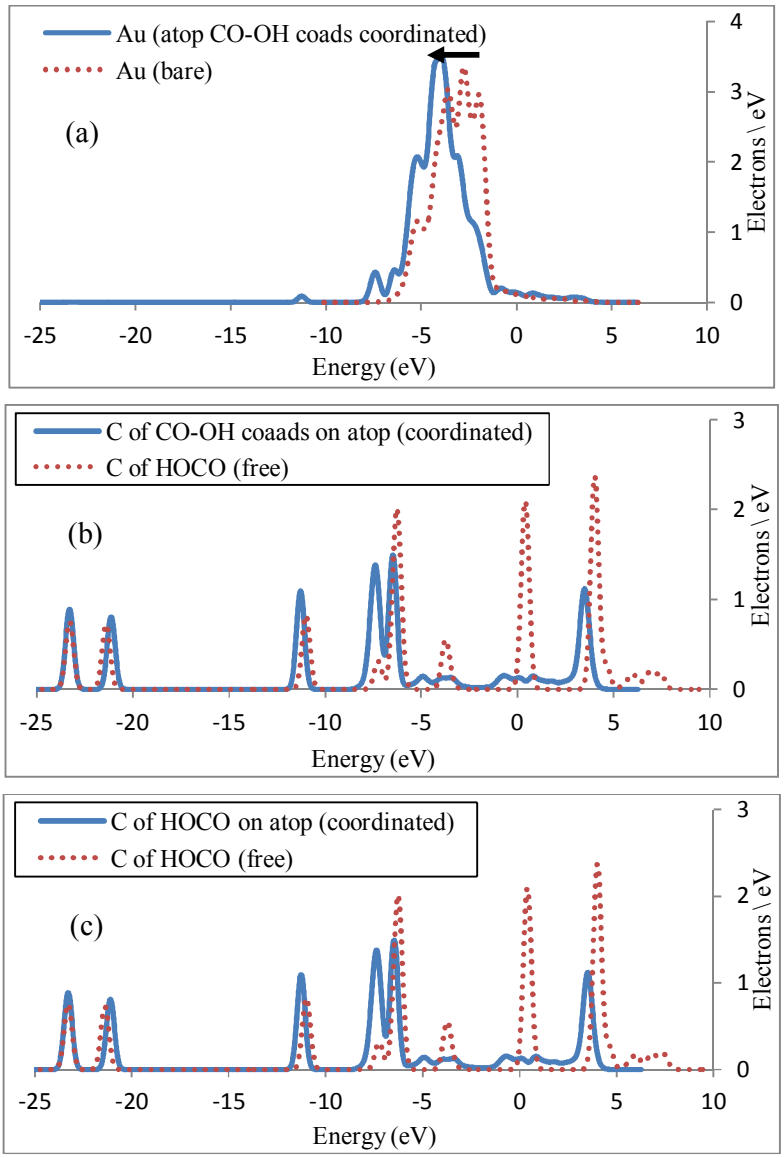

Figure 4.15. LDOS of (a) d-states of Au atom for its bare and atop coordinated states and (b) C of HOCO for its free and atop coordinated states upon CO-OH co-adsorption, and (c) C of HOCO for its free and atop coordinated states upon HOCO adsorption.

The results of the CO-OH co-adsorptions on Au(111) confirm that Au is an active catalyst for WGS reaction. In the literature, gold based catalysts were found promising WGS catalysts, and Au/metal oxides catalysts manifest a high catalytic activity in the

water gas shift reaction [18]. In recent studies, the gold/ceria catalysts are reported having high and stable activity with high CO selectivity [4, 6, 19].

4.2. Re(001) Surface

The Re(001) surface was modeled by using a (2x3) unit cell. The Re slab has 3 layers for which the coordinates of Re atoms at the bottom layer is fixed, and those at top two layers are relaxed. The Re(001) surface and possible adsorption sites on Re(001) are shown in Figure 4.16 and Figure 4.17, respectively. The parameters and conditions used in the adsorption studies conducted on Re surface are summarized in Table 4.9.

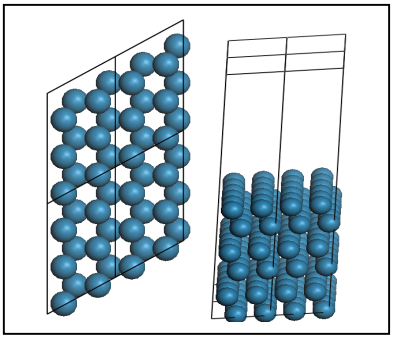

Figure 4.16. Top view (left) and side view (right) of Re(001) single crystal surface.

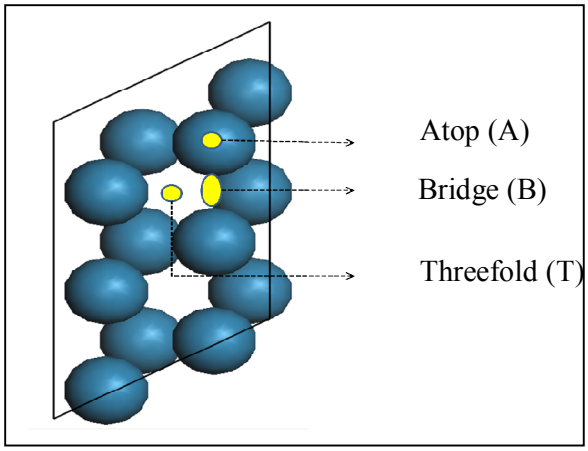

Figure 4.17. The possible adsorption sites A, B and T on Re(001) single crystal surface.

Table 4.9. The adsorption studies on Re(001) with the adsorbate and adsorption sites.

Metal Name	Surface	Size	Adsorbate	Adsorption Site	Adsorption ML
Re	(0 0 1)	2x3	CO	A, B, T	1 / 6
Re	(0 0 1)	2x3	OH	A, B, T	1 / 6
Re	(0 0 1)	2x3	H_2O	A, B, T	1 / 6
Re	(0 0 1)	2x3	CO_2	A, B, T	1 / 6
Re	(0 0 1)	2x3	H	A, B, T	1 / 6
Re	(0 0 1)	2x3	OH-CO co-ads	OH-A, CO-A	1/6, 1/6
Re	(0 0 1)	2x3	OH-CO co-ads	OH-B, CO-B	1/6, 1/6

4.2.1. CO Adsorption on Re(001)

CO adsorption on the possible adsorption sites (Atop-A, Bridge-B and Threefold-T) of Re(001) were performed for a constant surface coverage of 1/6 ML. For each one of the three possible sites shown in Figure 4.17, one CO molecule was placed on Re(001) surface setting the initial distance between carbon of CO and metal surface is 1.5 Å for which the CO molecule is positioned perpendicular to the metal surface, and is bonded from its carbon end. The adsorption energy, distance between C atom of CO and metal surface, and the C-O bond lengths upon CO adsorption are shown in Table 4.10 for adsorption on A, B and T sites.

Table 4.10. Adsorption sites (Site), adsorption energy (E_{ads}), distance between C of CO and metal surface ($d_{C\text{-}Surface}$), and bond length in CO ($d_{C\text{-}O}$) upon CO adsorption on Re(001).

CO adsorption on Re(001)			
Site	**E_{ads} (eV)**	**$d_{C\text{-}Surface}$ (Å)**	**$d_{C\text{-}O}$ (Å)**
A	-2.013	1.963	1.177
B	-1.941	1.772	1.196
T	-1.977	1.445	1.215

CO adsorption on A, B and T sites were found stable with -2.013, -1.941 and -1.977 eV adsorption energies, respectively. Though the binding energies of all three sites are very close each other, the strongest CO adsorption is on A site. As the number of coordination of CO with surface Re atoms is the highest on site T, CO is the closest to metal surface. In its coordinated state, CO molecular bond length is lower than that of its free state, 1.154 Å, for all adsorption types, indicating strong interaction between surface and CO. It should be noted that C-O bond length increases with the increase in coordination number of C with the metal surface.

In Figure 4.18, CASTEP energy optimized structure of adsorbed CO at A, B and T sites of Re(001) are shown. It is seen that CO molecule is still perpendicular to the metal surface at site A (Figure 4.18a) and site T (Figure 4.18c), but it is tilted towards metal surface on site B (Figure 4.18b).

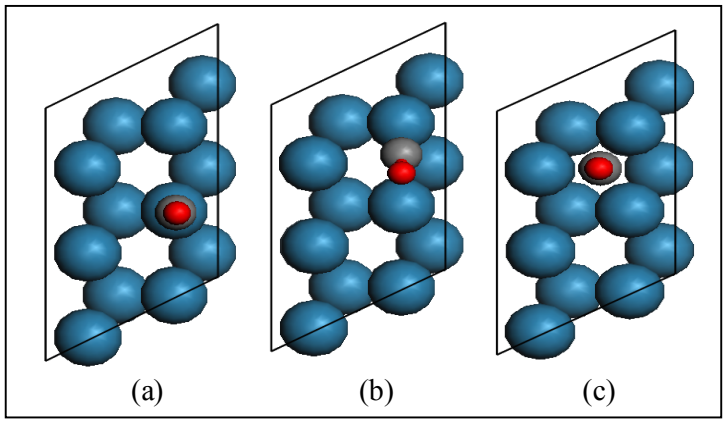

Figure 4.18. The top views of optimized CO adsorption on (a) site A, (b) site B, and (c) site T on Re(001).

Aiming to analyze how CO and metal atoms at the adsorption sites interact further, LDOS analysis was also performed for Re atoms on the surface for their bare and coordinated states as well as for carbon end of CO for its free and coordinated states. There is significant changes in LDOS of d-bands of Re atom on which CO is adsorbed compared to LDOS of bare Re atom (Figure 4.19a). The CO atom adsorbed at A site leads to the split of the d-band of Re around −9 eV. In addition, there are three distinct electron-rich regions along the energy scale of carbon end of atop coordinated CO as shown in Figure 4.19b.

The first peak at -23 eV corresponds to the 3σ molecular orbital which do not interact with the metal d-band, and there is no change in the energy level and electron density of this orbital upon adsorption. The second peak around -9 eV belongs to the 4σ-derived molecular orbital. The next peaks at -6 eV belong to the 1π-derived orbital. LDOS profiles of free and coordinated CO are significantly different for LDOS profiles of 4σ and 1π orbitals, proving the electronic interaction between CO molecule and the Re surface. The most significant contribution comes from the 5σ molecular orbital (around -3 eV in Figure 4.19-b), as the peak was vanished upon adsorption. These results are also valid for B and T sites.

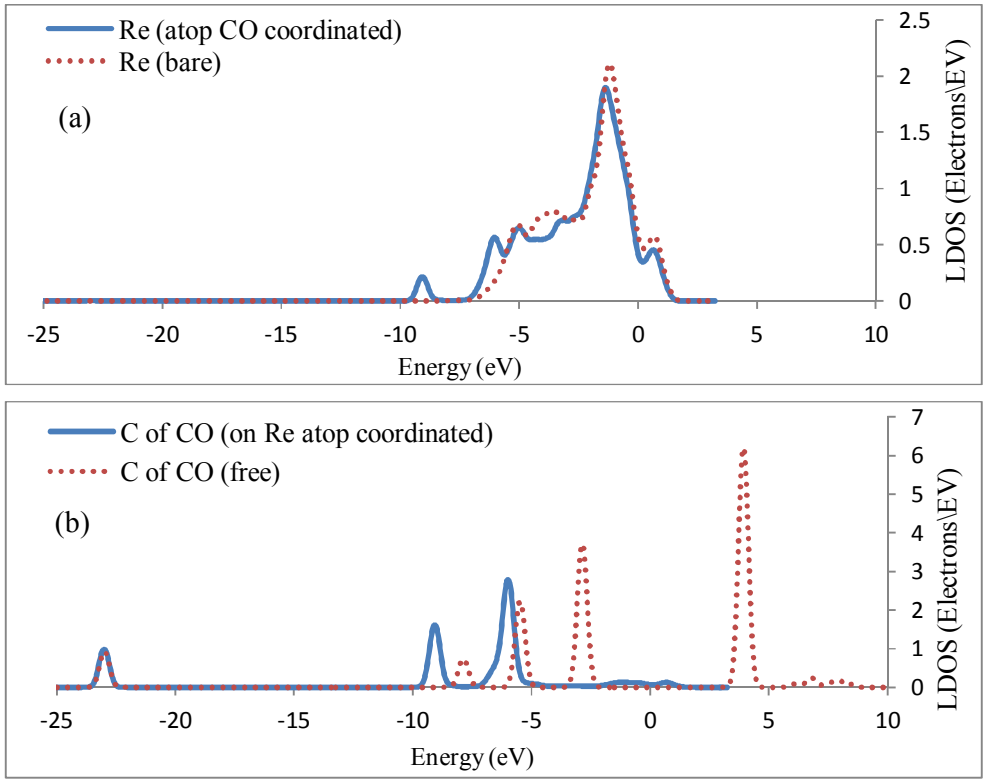

Figure 4.19. LDOS of (a) d-states of Re atom for its bare and atop CO coordinated states and (b) C of CO for its free and atop coordinated states.

The significant changes in the energy level and amplitude of the peaks present in the LDOS profiles of coordinated Re and CO compared to those of their uncoordinated states and strong CO adsorption on all three Re adsorption sites indicate that CO adsorption is energetically favorable and stable on Re surface.

4.2.2. OH Adsorption on Re(001)

OH adsorption on possible adsorption sites of Re(001) (Atop-A, Bridge-B and Threefold-T) for a constant surface coverage of 1/6 ML were studied. In the adsorption study, energy optimization was conducted for OH molecule which is oriented perpendicular to the surface and was attached each possible sites from its oxygen end. The adsorption energy, distance between O atom of OH and metal surface, and the molecular bond length in OH molecule upon OH adsorptions are shown in Table 4.11.

Table 4.11. Adsorption sites (Site), adsorption energy (E_{ads}), the distance between O of OH and metal surface ($d_{O\text{-}Surface}$), and the bond length in OH ($d_{O\text{-}H}$) upon OH adsorption on Re(001).

OH on Re(001)			
Site	**E_{ads} (eV)**	**$d_{O\text{-}surface}$ (Å)**	**$d_{O\text{-}H}$ (Å)**
A	-3.867	1.921	0.98
B->T	-4.417	1.365	0.977
T	-3.987	1.551	0.977

OH adsorption were found stable at sites A and T on Re(001) with adsorption energies of -3.867 and -3.987 eV, respectively. For OH adsorption at site B, OH atom moved towards threefold site in the neighborhood. The lowest adsorption energy indicates the most energetically favored adsorption site. According to the adsorption energies in Table 4.11, the most favored site for OH adsorption is site T. It is seen that site A is the second energetically preferred adsorption site following site T. The calculated OH adsorption energies on A and T sites indicate there is a strong interaction between OH and the Re surface. The tilted geometry of OH molecule in the energy optimized system hints that both O and H atoms interact with Re surface. The binding energies of OH on Re is higher than to those of OH on Au, confirming that OH has a stronger interaction with Re surface than with Au surface.

Though O-metal distance is not consistent with the sequence of adsorption strength, it is correlated with the coordination number of O atom with surface Re atoms (Table

4.11). As an example, OH on site T, which has higher the coordination number between OH and Re atoms, is the closest one to metal surface. In addition, the bond length of free OH is obtained as 0.991 Å. Although there is strong OH-surface interaction for all possible adsorption sites, the O-H bond lengths upon adsorption decrease, which can be explained through the tilting of OH molecule indicating that not only O-end of the OH interacts with surface, but also there is an interaction between H-end of OH and the metal atoms for site A (Figure 4.20a,b).

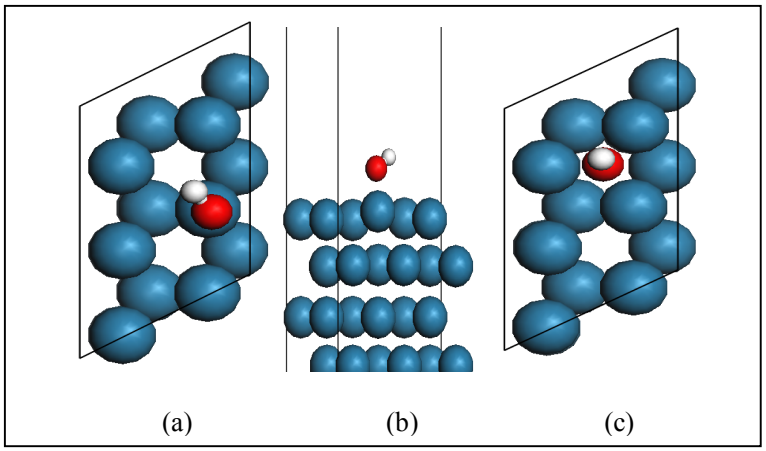

Figure 4.20. The visual models of optimized OH adsorption (a) on site A -top view-, (b) on site A -side view-, and (c) on site T -top view- on Re(001).

On the other hand, OH on T site preserved its perpendicular geometry to the metal surface upon adsorption (Figure 4.20c); for this site there is still H-metal interaction but, owing to perfectly symmetrical orientation of metal atoms with respect to OH, they vectorally cancelled out and perpendicular geometry is retained.

In order to understand how OH and metal atoms at the adsorption sites interact further, LDOS analysis was also performed for Re atoms on the surface for their bare and coordinated states as well as for oxygen end of OH for free and coordinated states of OH. The adsorption of OH on transition metal surface was studied previously by Hu *et al.* According to their results, 1π and 3σ orbitals of OH mix strongly with metal d-bands, leading to bonding and anti-bonding levels. On the contrary, 2σ orbital of OH does not mix with the metal d-states [44].

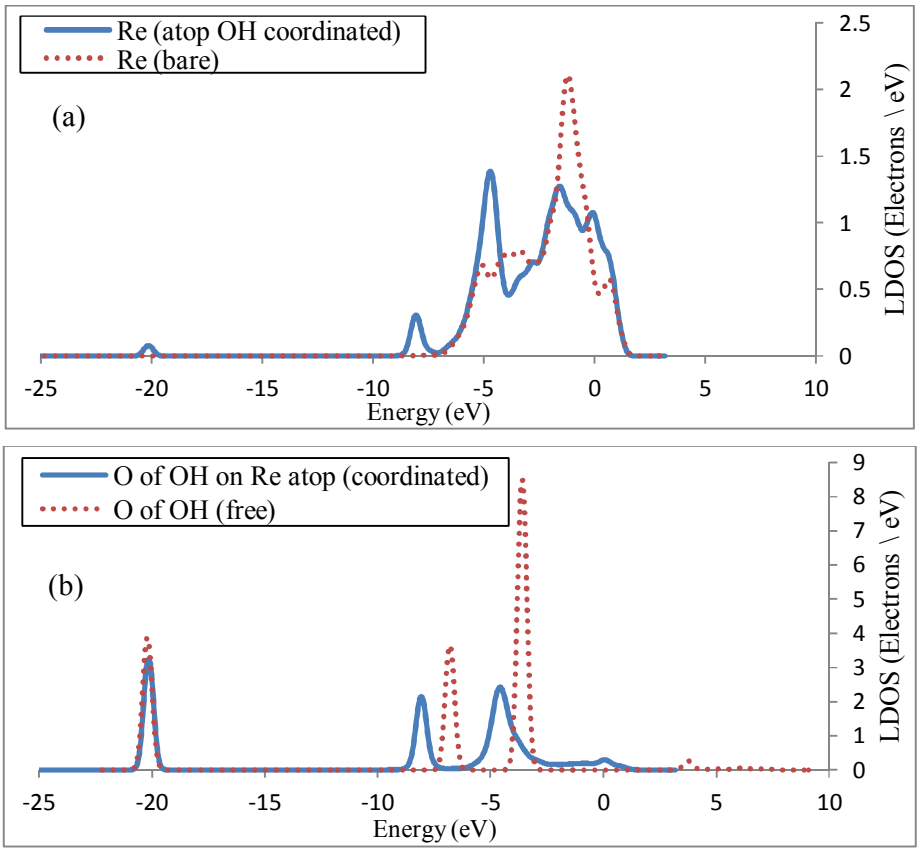

Figure 4.21. LDOS of (a) d-states of Re atom for its bare and atop OH coordinated states and (c) O of OH for its free and atop coordinated states.

A comparative analysis of LDOS of d-bands of bare and OH-coordinated Re atom on (Figure 4.21a), reveals that OH-adsorption led to a split of the Re d-bands around −7 eV. As can be seen in Figure 4.21b there are three distinct electron-rich regions along the energy scale for oxygen end of free OH, which are assigned to 2σ, 3σ and 1π molecular orbitals. The first peak at -20 eV corresponds to the 2σ orbital, which does not interacts with the metal d-bands, and there is no change in electron density profile of this orbital upon adsorption. The other peaks at -6.5 eV and -4 eV are assigned to 3σ and 1π orbitals of free OH, respectively. The shift of those peaks in the energy scale accompanied with significant change in their amplitudes proves that there is a strong electronic interaction between OH molecule and the Re surface. These results are also valid for site T.

Changes in LDOS profiles of Re and OH upon adsorption as well as strong OH adsorption indicated by low adsorption energies for atop and threefold Re sites indicate that OH adsorption is stable on Re surface.

4.2.3. H_2O Adsorption on Re(001)

H_2O adsorption on the possible adsorption sites (Atop-A, Bridge-B and Threefold-T) of Re(001) for a constant surface coverage of 1/6 ML was studied. Prior to simulations, one H_2O was placed at each one of adsorption sites (Figure 4.17) which is attached to metal atoms from its O-atom with 1.5 Å initial O-metal distance. Adsorption energy, distance between O atom of H_2O and metal surface, as well as bond lengths and bond angles in H_2O molecule upon energy optimization are given in Table 4.12.

Table 4.12. Adsorption sites (Site), adsorption energy (E_{ads}), distance between O of H_2O and metal surface ($d_{O\text{-}Surface}$), bond length ($d_{O\text{-}H}$) and angle (H-O-H) in H_2O upon H_2O adsorption on Re(001).

H_2O on Re(111)				
Site	**E_{ads} (eV)**	**$d_{O\text{-}surface}$ (Å)**	**$d_{O\text{-}H}$ (Å)**	**H-O-H (°)**
A	-0.4489	2.335	0.983	107.1
B->A	-0.4693	2.332	0.984	106.1
T->A	-0.453	2.332	0.986	105.5

H_2O adsorption is stable only at site A of Re(001) surface with the adsorption energy around -0.45 eV. The energetically most favored adsorption site is site A. H_2O originally at sites B and T moved towards site A as shown in the first column of Table 4.12 by the arrows. As all adsorbed H_2O molecules are stabilized at site A, the binding energies are essentially equal. The small differences in the adsorption energies, and bond lengths and angles of H_2O molecules upon energy optimization are most probably caused by the configuration of H_2O at different initial positions prior to energy optimization.

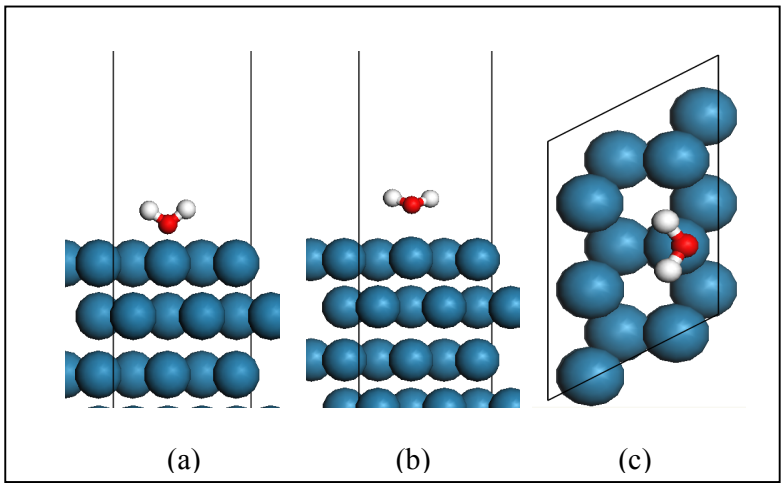

Figure 4.22. The visual models of H_2O adsorption on site A of Re(001): (a) side view prior to energy optimization, (b) side view upon energy optimization, and (c) top view upon energy optimization.

The initial and final structures of adsorbed H_2O on site A are given in Figure 4.22. At the end of energy optimization, H_2O molecule moves away from the metal surface to a distance around 2.3 Å (Figure 4.22a,b). H_2O molecular bond lengths and angle (Table 4.12) have small differences compared to those in the free H_2O molecule, which are 0.977 Å and 104.53° respectively, and the change in molecular orientation of H_2O from initially perpendicular orientation to parallel (Figure 4.22c) with respect to the metal surface upon energy optimization proves that, although it is limited, there still exists an interaction between H_2O and Re surface. These calculated values of the bond length and the angle of free H_2O are consistent with the experimental values for gaseous H_2O molecule, which are 0.96 Å and 104.474°, respectively [45].

Comparative analysis of LDOS profiles of Re atom at the sites in their bare and adsorbed states (Figure 4.23a) indicates there is no shift in d-band, and changes in amplitude along the energy scale is insignificant. Parallel analysis for O of H_2O indicates there are small shifts of LDOS peaks, which most probably comes from the change in orientation rather than direct metal-H_2O interaction.

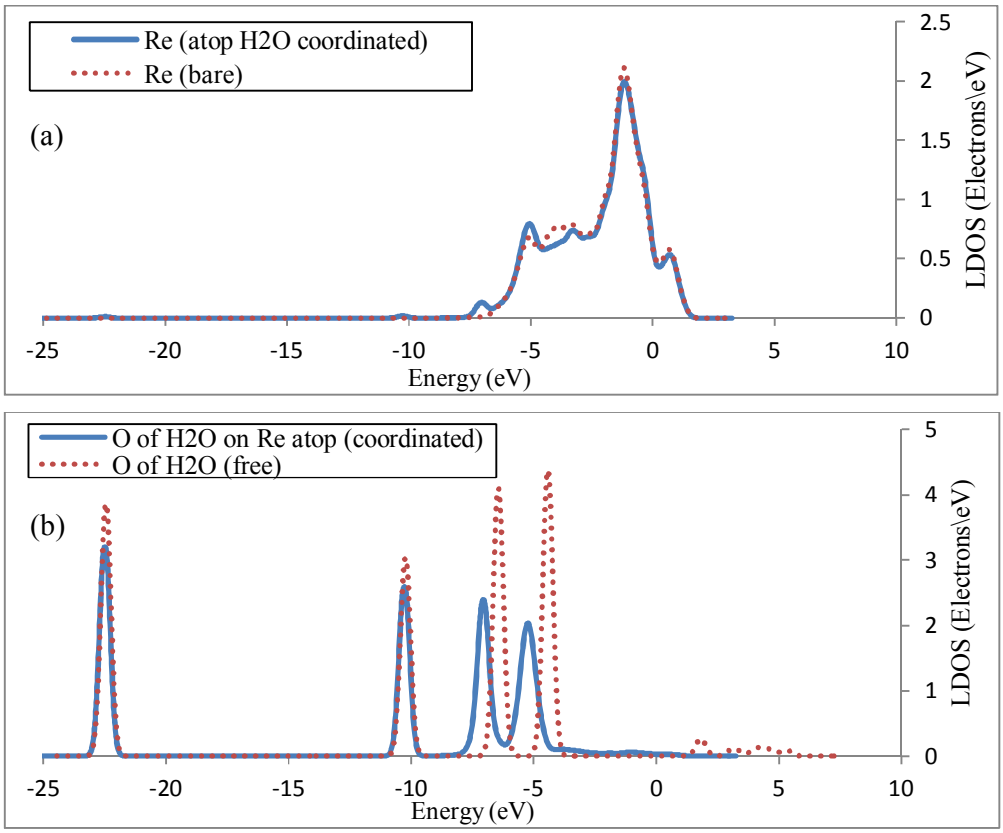

Figure 4.23. LDOS of (a) d-states of Re atom for its bare and atop H_2O coordinated states and (b) O of H_2O for its free and atop coordinated states.

4.2.4. CO_2 Adsorption on Re(001)

The CO_2 adsorption studies were performed for adsorption on possible adsorption sites (Atop-A, Bridge-B and Threefold-T) of Re(001) at a constant surface coverage of 1/6 ML. For each one of three possible sites shown in Figure 4.17, one CO_2 molecule was placed on Re(001) surface at the initial distance between the carbon of CO_2 and metal surface of 1.5 Å for which CO_2 molecule is bonded to metal surface from its carbon atom. The adsorption energy, the distance between C atom of CO_2 and metal surface, as well as molecular bond lengths and angle of CO_2 molecule upon energy optimization are given in Table 4.13.

Table 4.13. Adsorption sites (Site), adsorption energy (E_{ads}), distance between C of CO_2 and metal surface ($d_{C\text{-}Surface}$), bond length ($d_{C\text{-}O}$) and angle (O-C-O) in CO_2 upon CO_2 adsorption on Re(001).

CO_2 on Re(001)				
Site	**E_{ads} (eV)**	**$d_{C\text{-}surface}$ (Å)**	**$d_{C\text{-}O}$ (Å)**	**O-C-O (°)**
A	-0.005	3.661	1.181	179.8°
B	-0.537	1.772	1.262	134.8°
T	-0.432	1.575	1.327	117.1°

CO_2 adsorption is found stable at B and T sites on Re(001) surface. Though adsorption is not strong on both sites B and T with adsorption energies -0.537 and -0.432 eV, respectively, CO_2 geometry and position upon energy optimization confirms adsorption is stable; for adsorbed CO_2 molecule on B and T sites, C-O distance are 1.262 and 1.327, and O-C-O angle are 134.8° and 117.1°, respectively. Thus, the linearity of CO_2 at sites B and T is conserved. However, CO_2 is not stable at A site on Re(001) as the distance between the CO_2 and the Re surface upon energy optimization increase from 1.5 to 3.6 Å, i.e. it moves away from the Re surface, and its adsorption energy is also almost zero. In addition, the structure of CO_2 does not change upon adsorption on site A indicated by the bond lengths and the bond angles (Table 4.13) in CO_2 upon adsorption on A site, 1.181 Å and 179.8°, are the same for those of free CO_2 molecule, 1.181 Å which is in good agreement with experimental values of 1.160 Å [46], and 179.9°. Hence, these results of CO_2 adsorption on Re revealed that there is a significant interaction between CO_2 and Re surface for B and T sites, whereas there is no interaction between CO_2 and Re surface for site A.

The optimized structures of CO_2 at A, B and T sites on Re(001) are shown in Figure 4.24. It is seen that CO_2 on site A moves away from the Re surface (Figure 4.24a). On the other hand it is shown in Figure 4.24b,c that the linearity of CO_2 is not conserved.

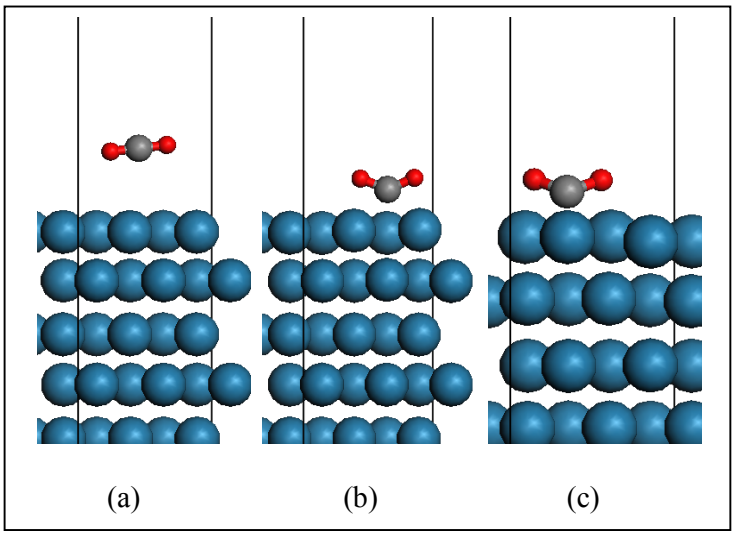

Figure 4.24. The side views of optimized CO_2 adsorption (a) on site A, (b) on site B, and (c) on site T on Re(001).

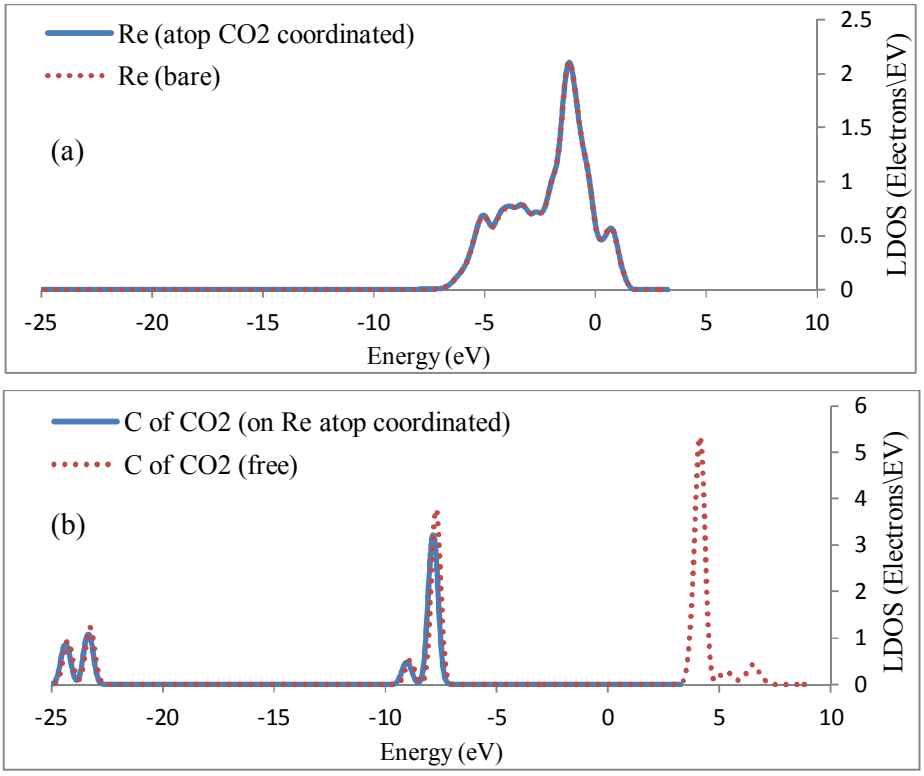

Figure 4.25. LDOS of (a) d-states of Re atom for its bare and atop CO_2 coordinated states and (b) C of CO_2 for its free and atop coordinated states.

Comparative analysis of LDOS profiles of Re on the site for its bare and coordinated states as well as C of CO_2 for its free and adsorbed states revealed that there is no change in LDOS profiles of C of CO_2 and Re upon adsorption on site A (Figure 4.25a and Figure 4.25b, respectively) whereas there are significant changes both in LDOS of metallic d-band as well as LDOS of C of CO_2, for example, for the adsorption on site B. This implies that there is an electronic interaction between CO_2 and Re for adsorption on sites B and T.

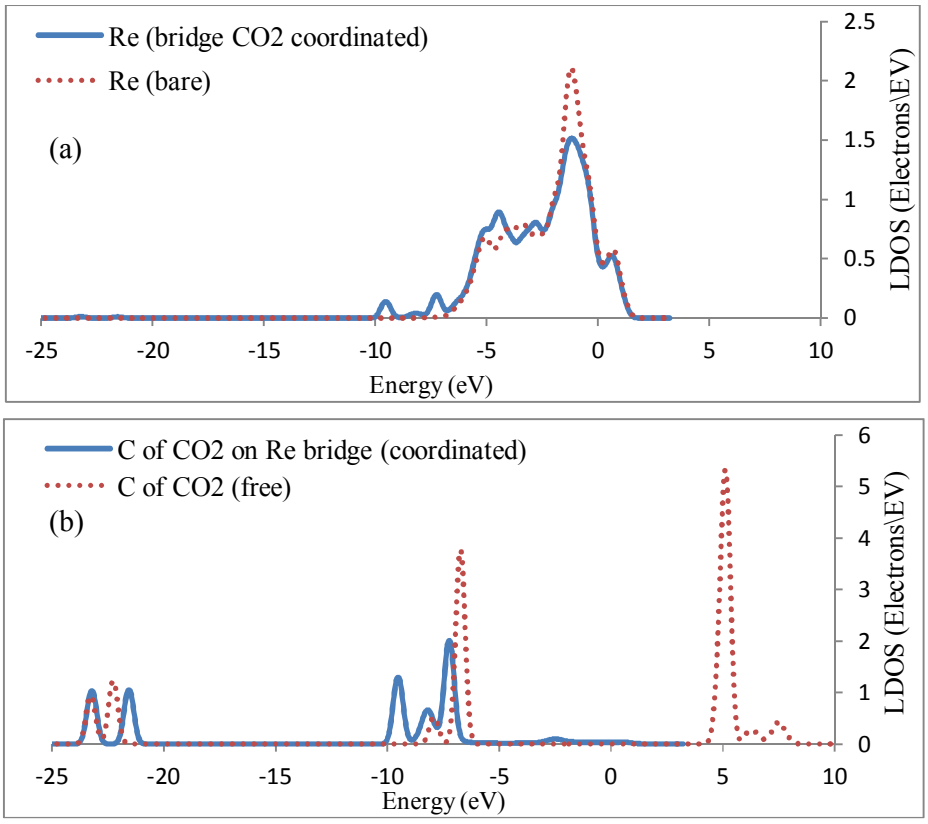

Figure 4.26. LDOS of (a) d-states of Re atom for its bare and bridge CO_2 coordinated states, and (b) C of CO_2 for its free and bridge coordinated states.

4.2.5. H Adsorption on Re(001)

H adsorption on the possible adsorption sites (Atop-A, Bridge-B and Threefold-T) of Re(001) were studied for a constant surface coverage of 1/6 ML. The adsorption energy and the distance between H atom and Re metal surface upon energy optimization are shown in Table 4.14.

Table 4.14. Adsorption sites (Site), adsorption energy (E_{ads}), and distance between H atom and metal surface ($d_{H\text{-}Surface}$) upon H adsorption on Re(001).

H on Re(001)		
Site	**E_{ads} (eV)**	**$d_{H\text{-}surface}$ (Å)**
A -> T	-4.131	1.02
B -> T	-4.115	1.06
T	-4.134	1.03

H adsorption is stable and strong only at site T of Re(001). As H atom moved towards threefold site for sites A and B upon energy optimization, H adsorption on those sites is unstable. The adsorption energy of H on site T of Re(001), -4.134 eV, indicate there is a strong interaction between H atom and the Re surface. Stability of H atom at site T upon energy optimization is shown in Figure 4.27.

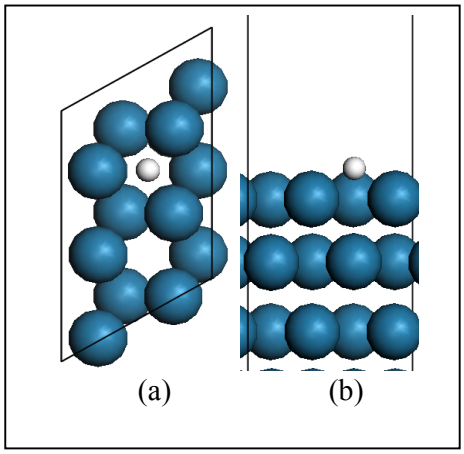

Figure 4.27. The visual models of optimized H adsorption on site T of Re(001): (a) top view and (b) side view.

Comparative analysis of LDOS profiles of free and threefold coordinated states of H atom indicates there is a significant shift in amplitude of electron density accompanied by ca. 7 eV shift in energy scale. The shift observed in parallel analysis for one of the coordinated Re atoms at site T does not seem significant, but one should consider that all three Re atoms at the site interact with the adsorbed H.

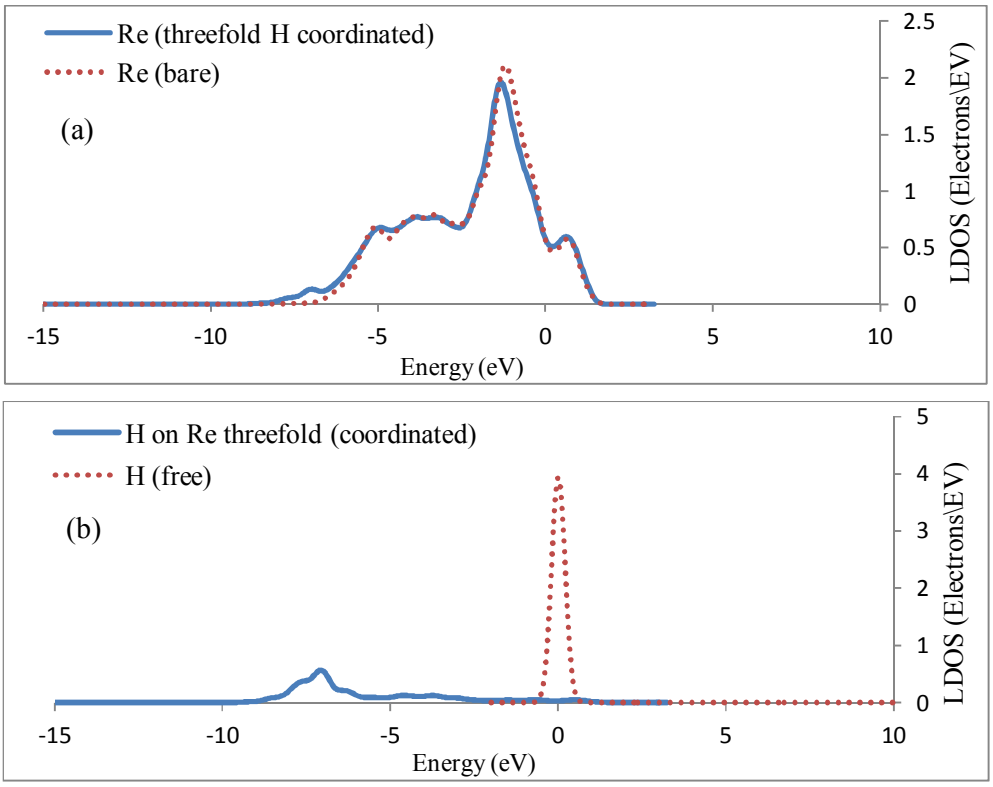

Figure 4.28. LDOS of (a) d-states of Re atom for its bare and threefold H coordinated states and (b) H atom for its free and threefold coordinated states.

For H adsorption on transition metal, it is known that the principal bonding comes from the interaction between 1*s* electron of H atom and d-electrons of transition metal. As can be followed from Figure 4.28b, the peak around at 0 eV is vanished, and a newly peak at -7.5 eV is formed, proving the significant electronic interaction between H and the Re surface. These results are consistent with the studies of Pallassana *et al.* In their DFT studies on the chemisorption of Hydrogen on Re(001), it was reported that there is a stronger interaction between the H 1s state with the Re d-band, which is responsible for the stronger chemisorption energy [34].

4.2.6. CO-OH Co-adsorption on Re(001)

CO and OH co-adsorption was studied on Re(001) for two different co-adsorption combinations (Table 4.15); in determining coadsorption site combinations, stability and

strength of individual CO and OH adsorptions on possible Re(001) sites. CO and OH surface coverage was taken as 1/6 ML for each; thus total surface coverage was 1/3 ML. For the first co-adsorption configuration, OH and CO were placed on atop sites, and for the second one, both were placed on bridge sites.

The initial and final structures of CO-OH co-adsorption (CO-atop and OH-atop) on Re(001) is shown in Figure 4.29. In the energy optimized state CO was still on Re atop and OH was tilted on Re atop without any CO-OH interaction. In the second case (CO-bridge and OH-bridge), CO moved from bridge site to atop site, which was found as a stronger adsorption site in individual adsorption studies, and OH moved from bridge site to threefold site which was obtained as the most energetically preferred site in individual adsorption studies. For both co-adsorption configurations, convergence of CO is similar to that of the CO on Re(001), and the convergence of OH is similar to that of the OH on Re(001). Energy optimization results and energy optimized CO and OH configurations for both co-adsorption combinations clearly showed that there is no interaction between CO and OH to form any WGS reaction intermediates, such as carboxyl (HOCO) molecule.

Table 4.15. Initial and final adsorption sites (CO Site and OH Site) for CO-OH co-adsorption.

CO-OH co-adsorption on Re(001)			
Initial		**Final**	
CO Site	**OH Site**	**CO Site**	**OH Site**
A	A	A	A -tilted
B	B	A	T

The results of the CO-OH co-adsorption on Re(001) are signified that Re alone is not an active catalyst for WGS reaction. This is consistent with the results of Çağlayan and Aksoylu's experimental study; there they reported that Re/ceria catalyst are inactive in WGS reaction [6].

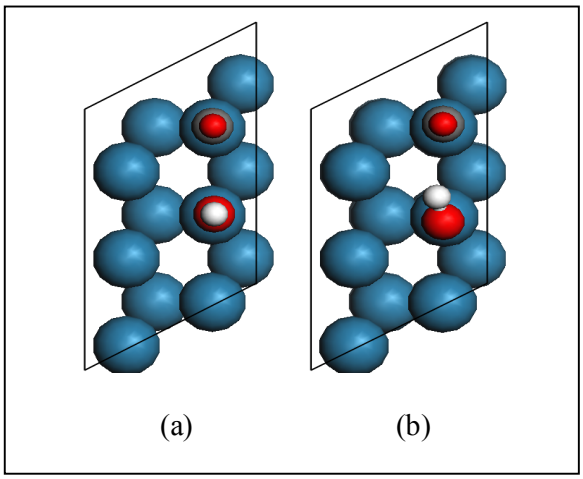

Figure 4.29. The visual models of CO-OH co-adsorption on Re(001): (a) initial structure (CO-atop and OH-atop) and (b) final structure (CO-atop and OH-atop).

4.3. Au-Re Surface Alloys

The aim of this study is to understand the reason of high activity and selectivity of Au-Re system through analyzing the steps of WGS reaction. Au-Re system for WGS has been experimentally studied by Çağlayan and Aksoylu. They reported that the novel Au–Re/ceria catalysts are highly active for WGS reaction, especially at high H_2O/CO feed ratios, led by the catalytically active and steam tolerant sites formed on the bimetallic catalyst. In the experimental study of Çağlayan, the novel catalysts were prepared through gold addition by dp technique on impregnated Re/ceria catalysts [6]. Thus, Au was added top of pre-formed Re sites. Under the light of this information, in the current work bimetallic Au_{ML}/Re(001) surfaces were studied. The notation of Au_{ML}/Re(001) describes the pseudomorphic surface which is formed by Au atoms with concentration levels between 1/6 to 6/6 ML at the top layer of Re(001) as point defects. In Figure 4.30, $Au_{1/6}$/Re(001), $Au_{3/6}$/Re(001), and $Au_{6/6}$/Re(001) surfaces are shown.

The stability of surface alloys with different Au concentrations at the surface layers can be compared based on their surface energies. The surface energy values of the structures calculated according to the equation 3.2 are given in Table 4.16.

Table 4.16. Surface energy (E_{Surf}) of Re(001) and Au-Re surface alloys with different Au concentrations at topmost surface layer. The top views of optimized surfaces are given in the first column: Dark balls (blue) represent Re, light ones (yellow) represent Au atoms.

	Surface Structure	**E_{surf} (J/m^2)**
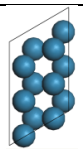	Re(001)	2.62
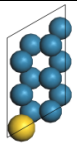	$Au_{1/6}$/Re(001)	2.63
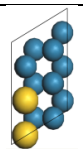	$Au_{2/6}$/Re(001)	2.59
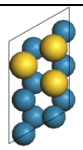	$Au_{3/6}$/Re(001)	2.57
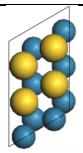	$Au_{4/6}$/Re(001)	2.48
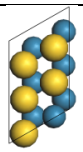	$Au_{5/6}$/Re(001)	2.32
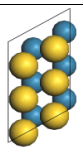	$Au_{6/6}$/Re(001)	2.20

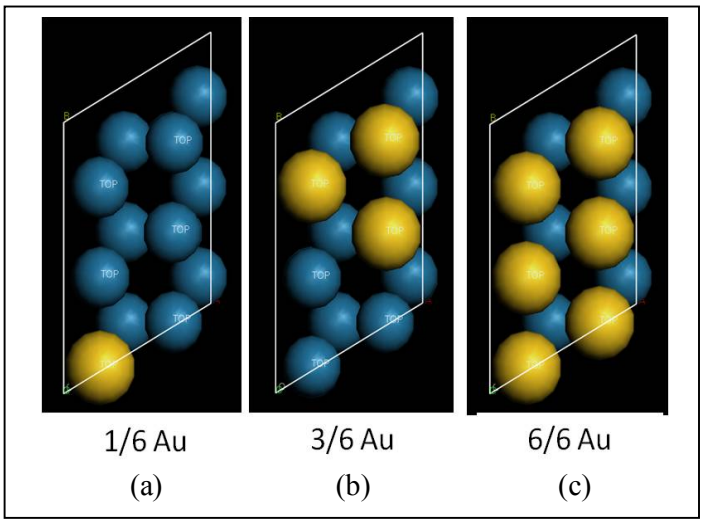

Figure 4.30. The pseudomorphic Au-Re surface alloys: (a) $Au_{1/6}$/Re(001), (b) $Au_{3/6}$/Re(001), and (c) $Au_{6/6}$/Re(001).

The results show that the surface energy of Au-Re alloy depends on the Au concentration at the topmost layer (Table 4.16). When one single Au atom was added as a point defect on Re(001), which is a (2x3) cell, resulting in a Au concentration of 1/6 at the topmost layer, $Au_{1/6}$/Re(001), surface energy become 2.63 J/m^2. The addition of a second Au increasing the surface concentration to 2/6 at the topmost layer, $Au_{2/6}$/Re(001), slightly decreases surface energy to 2.59 J/m^2. With the further increase in Au surface concentration, the surface energy of Au-Re surface alloys decreased (Figure 4.31).

In order to further understand the interaction between Au and Re atoms, LDOS analysis was performed for Au atoms on Au_{ML}/Re(001) surface. LDOS profiles show the changes in the energy level and amplitude of the electron density distribution of the d-band of Au atom on Au-Re surface alloy compared to LDOS of bare Au. A comparative analysis of the d-bands of Au atoms present on Au(111) and the bimetallic Au_{ML}/Re(001) surfaces reveals an interesting change in the d-band structure for the bimetallic surface. The strong electronic interaction of the Au overlayer with the Re atoms in the bimetallic slab causes significant d-band shifts. Similar changes in d-band were also reported by Pallassana *et al.* in their DFT studies for bimetallic metal surfaces of Re and Pd [34].

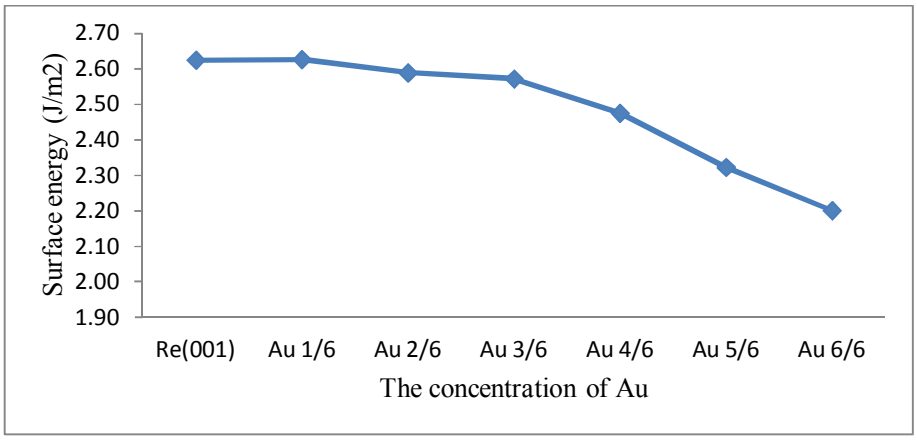

Figure 4.31. Surface energy vs. Au concentration at topmost layer which increases from 0, monometallic Re(001) surface, to 6/6 (100%), pseudomorphic Au layer over Re(001).

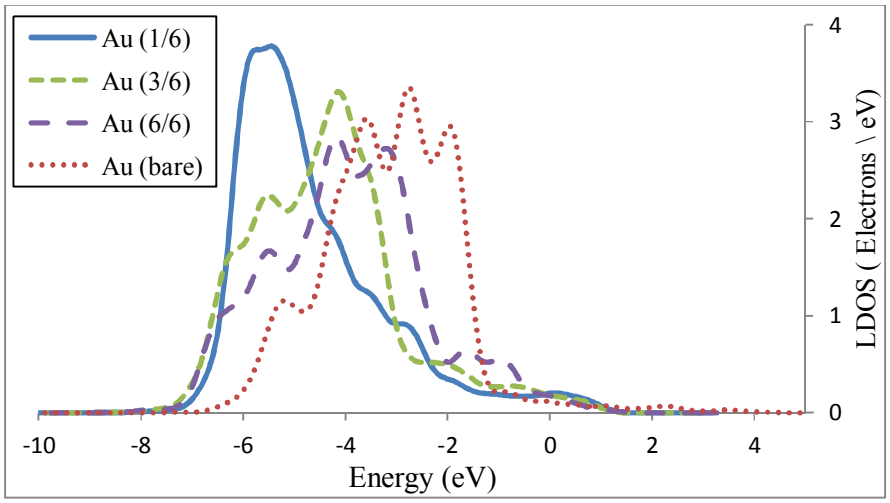

Figure 4.32. LDOS of d-band of Au atoms for its bare states on $Au_{1/6}$/Re(001), $Au_{3/6}$/Re(001), and $Au_{6/6}$/Re(001) surface alloys, and Au atom for its bare state on monometallic Au(111).

For Au_{ML}/Re(001) surface alloys the most significant shift in LDOS of Au occurs for $Au_{1/6}$/Re(001) surface; there three peaks of Au of Au(111) im (-2)-(-4) eV regions are combined and shifted to ca. -6 eV. With the increase in Au surface concentration, LDOS of Au d-band becomes more similar in shape to that of Au of Au(111) accompanied by a shift in peaks towards high energy levels.

The decrease in the surface energies of Au_{ML}/Re(001) bimetallic surface compared to that of Re(001) show that surface alloy can be formed by Au and Re metals, and the remarkable changes in LDOS of Au atoms on Au_{ML}/Re(001) bimetallic surface imply that there is a significant interaction between Au and Re atoms modifying d-band of Au adatoms. This is consistent with the results of the experimental study by Çağlayan *et al* on Au-Re system. They reported that gold addition by dp technique on impregnated Re/ceria catalysts led to higher dispersion and stronger interaction between Au and Re particles and formation of Au-Re surface alloys [6].

4.3.1. CO Adsorption on Au-Re Surface

Rodrigez reported that CO adsorbs on the gold sites during WGS reaction [9]. CO adsorption study was performed on $Au_{1/6}$/Re(001), $Au_{3/6}$/Re(001) and $Au_{6/6}$/Re(001) bimetallic surfaces for a constant surface coverage of 1/6 ML. For each one of three surfaces shown in Figure 4.30, one CO molecule was placed on Au atop for which the initial distance between carbon of CO and metal surface was initially 1.5 Å and CO molecule was perpendicular to metal surface. The adsorption energy, the distance between C atom of CO and metal surface, the C-O bond length, and the initial and final positions of adsorbed CO molecule are shown in Table 4.17.

Table 4.17. The initial and final sites, adsorption energy (E_{ads}), distance between C of CO and metal surface ($d_{C\text{-}Surface}$), and bond length in CO molecule ($d_{C\text{-}O}$) upon CO adsorption on $Au_{1/6}$/Re(001), $Au_{3/6}$/Re(001), and $Au_{6/6}$/Re(001) surface alloys.

CO on Au-Re Surface Alloys					
Au-Re surface	**Initial Site**	**Final Site**	**E_{ads} (eV)**	**$d_{C\text{-}surface}$ (Å)**	**$d_{C\text{-}O}$ (Å)**
$Au_{1/6}$/Re(001)	Au-A	Au-A	-0.221	2.016	1.165
$Au_{3/6}$/Re(001)	Au-A	Au-A	-0.168	2.028	1.164
$Au_{6/6}$/Re(001)	Au-A	Au-A	-0.291	2.071	1.16

CO adsorption at Au atop site is stable with adsorption energies of -0.221, -0.168 and -0.291 eV on $Au_{1/6}$/Re(001), $Au_{3/6}$/Re(001) and $Au_{6/6}$/Re(001) surfaces, respectively. The adsorption energies calculated indicate that CO is weakly adsorbed at Au atop on all three Au-Re surfaces. The bond length of free CO is calculated as 1.154 Å, and the molecular bond length of adsorbed CO molecule in Table 4.17 is greater for all Au atop adsorption systems meaning that C-O bond stretches out led by the adsorbate and surface interaction. It should be noted that the adsorption of CO on Au-Re surfaces is weaker than the adsorption of CO on monometallic single crystal Au and Re surfaces.

Figure 4.33 shows the energy optimized CO geometries on Au-Re surface alloys. The Au-atop adsorbed CO molecules on Au-Re surfaces are still bonded with carbon end, and positioned perpendicular to the surface.

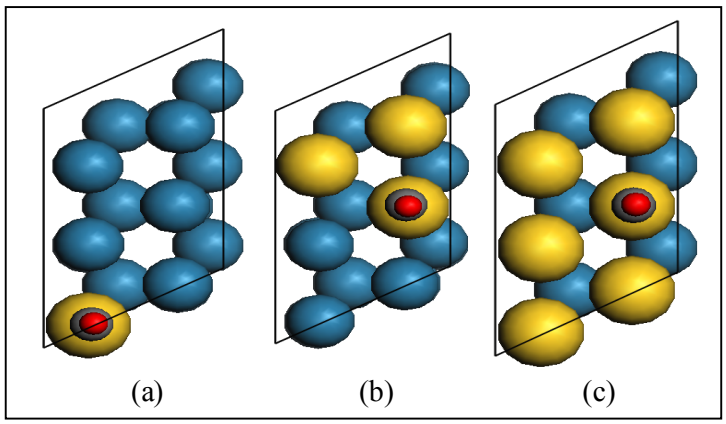

Figure 4.33. The top views of optimized CO adsorption on atop Au sites of (a) $Au_{1/6}$/Re(001), (b) $Au_{3/6}$/Re(001), and (c) $Au_{6/6}$/Re(001) surface alloys upon energy optimization.

4.3.2. OH Adsorptions on Au-Re Surface

OH adsorption on Au-Re surface was analyzed aiming to understand the effect of alloying with Re on the adsorption properties of Au. The studies were performed on $Au_{3/6}$/Re(001) and $Au_{6/6}$/Re(001) bimetallic surfaces for a constant OH surface coverage of 1/6 ML. The adsorption energy, the distance between O atom of OH and metal surface, the

O-H bond length, and the initial and final positions of adsorbed OH molecule are shown in Table 4.18.

Considering OH-adsorption is the strongest on bridge site of Au(111), bridge type OH adsorption on Au atoms of $Au_{3/6}$/Re(001) was performed as an example to analyze the effect of Re-alloying on OH adsorption first. OH molecule diffuse from Au-bridge site to neighboring Re and stabilized on atop-Re site with adsorption energy of -3.889 eV in the energy optimized system. The simulation result reveals that Re presence destabilize the bridge-type OH adsorption on Au site of $Au_{3/6}$/Re(001) and there is an OH transfer from Au to Re through the Au-Re interface (Figure 4.34). The initial perpendicular orientation of OH on Au-bridge site was also transformed in to a tilted orientation on Re-atop site.

Table 4.18. The initial and final sites, adsorption energy (E_{ads}), distance between O of OH and metal surface ($d_{O\text{-}Surface}$), and bond length in OH molecule ($d_{O\text{-}H}$) upon OH adsorption on $Au_{3/6}$/Re(001) and $Au_{6/6}$/Re(001) surface alloys.

OH on Au-Re Surface Alloys					
Au-Re surface	**Initial Site**	**Final Site**	**E_{ads} (eV)**	**$d_{O\text{-}surface}$ (Å)**	**$d_{O\text{-}H}$ (Å)**
$Au_{3/6}$/Re(001)	Au-B	Re-A (tilted)	-3.889	1.927	0.981
$Au_{6/6}$/Re(001)	Au-A	Au-A (tilted)	-2.361	2.11	0.981

This is explained with two reasons: (i) the adsorption strength of OH on Re atop is higher than that of OH on Au bridge site as the binding energies of OH on Re in general are higher than that of OH on Au, and (ii) the electronic structure of Au is modified by Re presence through Au-Re interaction as indicated by differences between LDOS profile of Au d-band for bare Au(111) and Au-Re surface alloy.

Secondly, Au atop adsorption at pseudomorphic Au layer on Re, i.e. $Au_{6/6}$/Re(001), was studied in order to analyze effect of Re on OH adsorption properties on Au. A

comparative analysis with OH adsorption properties on Au(111) reveals that presence of Re layer beneath slightly strengthen OH adsorption on Au-atop, i.e. OH adsorption energy at atop Au decreases from -2.204 eV on Au(111) to -2.361 eV on $Au_{6/6}$/Re(001). This is an expected result as OH adsorption of monometallic Re(001) is far stronger with adsorption energy of -3.8 eV. Note that initial perpendicular orientation of OH on Au-atop of $Au_{6/6}$/Re(001) changed to a tilted orientation allowing H-end gets closer to the surface.

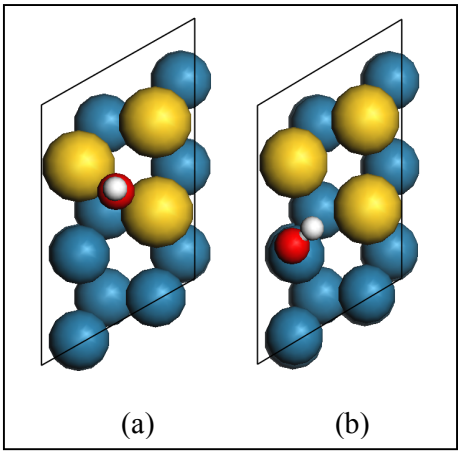

Figure 4.34. The top views of OH adsorption on $Au_{3/6}$/Re(001): (a) initial (OH on bridge Au) and (b) final (OH on atop Re) structures.

4.3.3. CO-OH Co-adsorptions on Au-Re Surface

The aim of this study was to understand the reason of high activity and selectivity of Au-Re system through analyzing the steps of WGS reaction. Au-Re system for WGS has been experimentally studied by Çağlayan and Aksoylu. They reported that the novel Au–Re/ceria catalysts are highly active for WGS reaction, especially at high H_2O/CO feed ratios, led by the presence of catalytically active and steam tolerant sites formed on the bimetallic catalyst [6]. Therefore, the surface reaction between CO and OH on Au-Re system was analyzed in the current study. CO and OH co-adsorption studies were performed on different Au-Re surface alloys, i.e. $Au_{1/6}$/Re(001), $Au_{3/6}$/Re(001) and $Au_{6/6}$/Re(001) surfaces. Surface coverage of CO and OH were taken as 1/6 ML for each. In CO-OH co-adsorption system, total surface coverage was 1/3 ML.

Firstly, CO-OH co-adsorption was studied on $Au_{1/6}$/Re(001) surface. According to the literature on WGS reaction, it is well-known that CO adsorbs on Au active sites [9]. Therefore, CO was placed on Au-atop site and OH was placed on Re-atop site prior to energy optimization (Figure 4.35a). In the energy optimized state (Figure 4.35-b), CO was still on Au atop and OH moved from Re-atop to Re-bridge site, which was found as the energetically unfavorable site on Re(001) surface in individual adsorption studies, without any CO-OH interaction. OH movement proves that the electronic structure of Re atoms on Re(001) surface is modified by Au presence through Au-Re interaction.

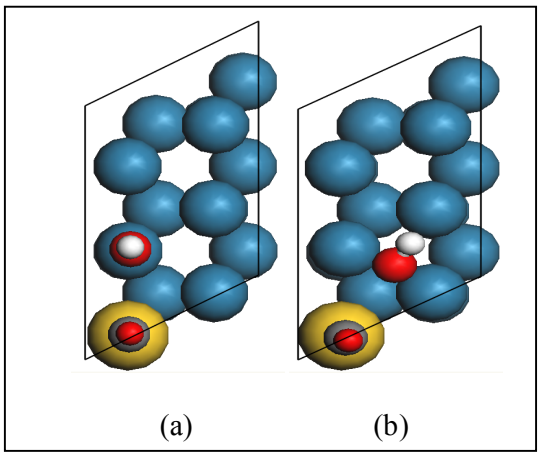

Figure 4.35. The top views of CO-OH co-adsorption on $Au_{1/6}$/Re(001) surface alloy: (a) initial (CO-atop Au and OH-atop Re) and (b) final (CO-atop Au and OH-bridge Re) structures.

.

CO-OH co-adsorption was studied on $Au_{3/6}$/Re(001) surface with two different adsorption combination considering stability/adsorption strength of individual CO and OH on the possible adsorption sites of Au(111). For the first co-adsorption configuration (Figure 4.36a), CO and OH were placed on Au-atop sites of $Au_{3/6}$/Re(001) surface, whereas for the second one (Figure 4.36c), both CO and OH were placed on Au-bridge sites of $Au_{3/6}$/Re(001) surface. The energy optimized forms of both coadsorption configurations clearly indicate the formation of cis-HOCO species through CO-OH interaction, which is reported as the intermediate species for the carboxyl mechanism of WGS reaction on Au(111) by Liu *et al.* [26].

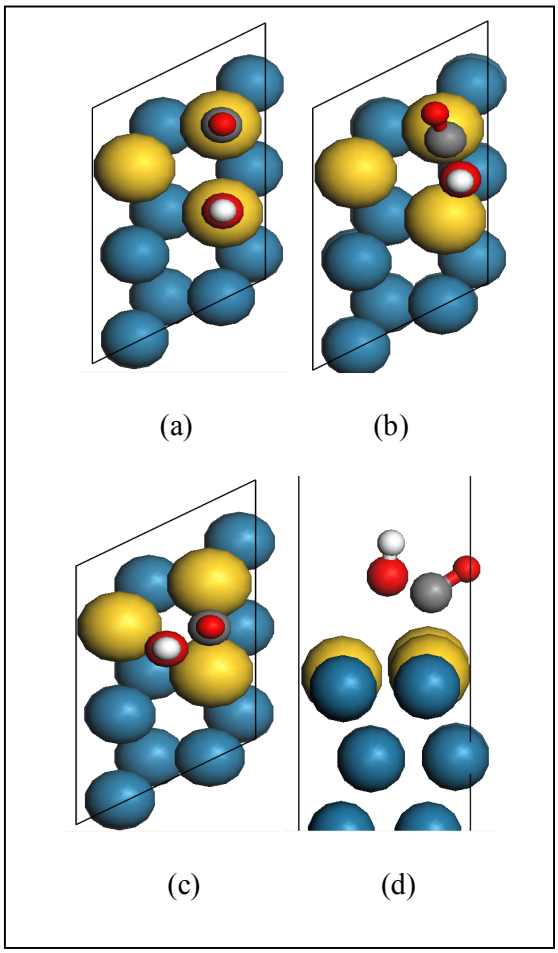

Figure 4.36. The visual models of CO-OH co-adsorption on $Au_{3/6}$/Re(001) surface alloy: (a) initial and (b) final structures for the first co-adsorption configuration, and (c) initial and (d) final (side view) structures for the second co-adsorption configuration.

For CO-OH co-adsorption studies on $Au_{3/6}$/Re(001) surface, the positions and movement of CO and OH molecules from the initial to the final stages of energy optimization are given in Figure 4.36. There, for the first co-adsorption configuration, CO and OH were at their initial positions in Figure 4.36a, i.e. CO and OH adsorbed on Au-atop sites of $Au_{3/6}$/Re(001) surface, and in the energy optimized structure the HOCO molecule was formed as shown in Figure 4.36b. For the second co-adsorption configuration, CO and OH were at their initial positions in Figure 4.36c, i.e. CO and OH adsorbed on Au-bridge sites of $Au_{3/6}$/Re(001) surface, and in the energy optimized structure the HOCO molecule was formed as shown in Figure 4.36d. In both cases, CO and OH were getting close to

each other during energy optimization scheme, formed HOCO molecule, and HOCO moved to Au atop position.

For CO-OH co-adsorption study on $Au_{6/6}$/Re(001) surface, i.e. the pseudomorphic Au layer over Re(001), CO and OH initially adsorbed on Au-atop sites of $Au_{6/6}$/Re(001) surface, and in the energy optimized structure the HOCO molecule was formed. There, CO and OH were getting close to each other during energy optimization scheme, form HOCO molecule, and HOCO moved to Au atop position.

A comparative analysis of the H-O, O-C, C-O bond lengths, H-O-C and O-C-O bond angles and C-surface distance of HOCO molecule (Table 4.19) with the same parameters obtained for HOCO molecule formed through CO-OH coadsorption on Au(111), $Au_{3/6}$/Re(001), and $Au_{6/6}$/Re(001) surfaces clearly shows that the values perfectly matches with each other confirming the formation of WGS reaction intermediate HOCO through CO-OH surface interaction on Au sites of $Au_{3/6}$/Re(001) and $Au_{6/6}$/Re(001) surfaces.

Table 4.19. The values of bond lengths and angles of HOCO at atop on monometallic Au(111) upon HOCO adsorption, and HOCO formed at atop Au on Au-Re surface alloys upon CO-OH co-adsorption.

Surface	**Site**	**d_{H-O} (Å)**	**d_{O-C} (Å)**	**d_{C-O} (Å)**	**H-O-C (°)**	**O-C-O (°)**	**$d_{C-surface}$ (Å)**
Au(111)	HOCO-A	0.991	1.215	1.356	106.988	124.01	2.107
$Au_{3/6}$/Re(001)	CO-Au A, OH-Au A	0.993	1.215	1.367	106.843	122.454	2.121
$Au_{3/6}$/Re(001)	CO-Au B, OH-Au B	0.991	1.217	1.359	107.986	123.67	2.121
$Au_{6/6}$/Re(001)	CO-Au A, OH-Au A	0.992	1.213	1.365	108.874	123.778	2.093

Table 4.20. Initial co-adsorption sites (Site), adsorption energy (E_{ads}), and distance between the carbon of HOCO and Au atom ($d_{C\text{-}surface}$) upon CO-OH co-adsorption on $Au_{3/6}$/Re(001), $Au_{3/6}$/Re(001) and $Au_{6/6}$/Re(001) surface alloys.

CO-OH co-adsorption on Au-Re Surface			
Surface	**Initial Site**	**E_{ads} (eV)**	**$d_{C\text{-}surface}$ (Å)**
$Au_{3/6}$/Re(001)	CO-Au A, OH-Au A	-3.93	2.121
$Au_{3/6}$/Re(001)	CO-Au B, OH-Au B	-3.999	2.121
$Au_{6/6}$/Re(001)	CO-Au A, OH-Au A	-3.917	2.093

The total adsorption energy of the co-adsorption, which can be taken as the formation energies of HOCO molecule, and the distance between Au atom and the carbon of HOCO molecule formed for CO-OH co-adsorption studies on $Au_{3/6}$/Re(001) and $Au_{6/6}$/Re(001) surfaces are shown in Table 4.20 . The formation energy of HOCO molecule is around -4 eV for each coadsorption combinations. The highly negative adsorption energy values indicate that the formation of HOCO through CO-OH interaction on the surface is energetically favorable.

5. CONCLUSIONS AND RECOMMENDATIONS

5.1. Conclusions

The current study on the steps of WGS reaction involves the analysis of adsorption/co-adsorption of WGS reactants, products and possible intermediate species on Au(111), Re(001) and Au-Re(001) surfaces at atomic scale via utilizing DFT modules of CASTEP. The results obtained reveal that monometallic Au and Au-Re surface alloy are active catalysts, whereas Re is not an active catalyst for WGS reaction. Though active, monometallic Au is not resistant to high H_2O concentrations but Au-Re surface alloy is.

CO adsorption was found stable but weak on the Au surface whereas OH-adsorption was strong and stable. Also, OH has stronger interaction with Au surface than that of CO in terms of its high binding energy. It is inferred that the active sites on Au surface, which dominantly participate in WGS reaction steps, can be poisoned by OH molecules due to site competition. This confirms that high H_2O/CO feed ratios leads to a decreased WGS activity over Au/ceria catalyst.

The results of H_2O and CO_2 adsorption on Au(111) show that H_2O adsorption is very weak since there is a very limited interaction between H_2O and Au surface, and CO_2 adsorption is unstable. CO_2 molecule desorbs from the surface as a product of WGS reaction.

The binding energies of OH on Re are higher than that of OH on Au. It is concluded that OH molecules can move from Au sites to Re sites, and the active sites on Au surface can be poisoned by OH molecules to a lesser degree. This proves that Re increases steam resistance of Au-Re/ceria catalyst, which was reported in the experimental study of Çağlayan and Aksoylu [6].

The co-adsorption of CO and OH molecules on Au(111), Re(001) and Au-Re surfaces reveals that WGS reaction takes place on Au sites of monometallic and Au-Re

surface alloy, and the surface reaction between CO and OH molecules on Au is consistent with the carboxyl mechanism.

5.2 Recommendations

The adsorption/co-adsorption of OH molecules on Re(001) should be studied further in order to explain possible OH utilization mechanisms on Re surface.

The sequential steps of carboxyl mechanism of WGS reaction should be studied starting from formation of HOCO intermediate to production of CO_2. Other two possible mechanisms (redox mechanism and carboxyl mechanism) for the water-gas shift reaction on Au(111) surface should be analyzed on Au-Re surface alloys.

Au-Re/Ceria catalyst should be studied by the addition of Au and Re as point defects on ceria via CASTEP in order to form more realistic comparison basis to the experimental results.

REFERENCES

1. Ghenciu, A. F., "Review of Fuel Processing Catalysts for Hydrogen Production in PEM Fuel Cell Systems", *Current Opinion in Solid State and Materials Science*, Vol. 6, pp. 389-399, 2002.

2. Qi, X., and M. Flytzani-Stephanopoulos, "Activity and Stability of Cu-CeO_2 Catalysts in High-Temperature Water-Gas Shift for Fuel-Cell Applications", *Industrial & Engineering Chemistry Research*, Vol. 43, pp. 3055-3062, 2004.

3. Azzam, K. G., I. Babich, K. Seshan, and L. Lefferts, "Role of Re in Pt–Re/TiO_2 Catalyst for Water Gas Shift Reaction: A Mechanistic and Kinetic Study", *Applied Catalysis B: Environmental*, Vol. 80, pp. 129-140, 2008.

4. Fu, Q., W. Deng, H. Saltsburg, and M. Flytzani-Stephanopoulos, "Activity and Stability of Low-Content Gold–Cerium Oxide Catalysts for the Water–Gas Shift Reaction", *Applied Catalysis B: Environmental*, Vol. 56, pp. 57-68, 2005.

5. Tabakova, T., M. Manzoli, D. Paneva, F. Boccuzzi, V. Idakiev, and I. Mitov, "CO-free Hydrogen Production over Au/CeO_2-Fe_2O_3 Catalysts: Part II. Impact of the Support Composition on the Performance in the Water Gas Shift Reaction", *Applied Catalysis B: Environmental*, Vol. 101, pp. 266-274, 2011.

6. Çağlayan, B. S., and A. E. Aksoylu, "Water Gas Shift Activity of Ceria Supported Au-Re Catalysts", *Catalysis Communications*, Vol. 12, pp. 1206-1211, 2011.

7. Chayakul, K., T. Srithanratana, and S. Hengrasmee, "Effect of Re Addition on the Activities of Co/CeO_2 Catalysts for Water Gas Shift Reaction", *Journal of Molecular Catalysis A: Chemical,* Vol. 340, pp. 39-47, 2011.

8. Kunkes, E. L., D. A. Simonetti, J. A. Dumesic, W. D. Pyrz, L. E. Murillo, J. G. Chen, and D. J. Buttrey, "The Role of Rhenium in the Conversion of Glycerol to Synthesis Gas over Carbon Supported Platinum–Rhenium Catalysts", *Journal of Catalysis,* Vol. 260, pp. 164-177, 2008.

9. Rodriguez, J. A, "Gold-based Catalysts for the Water–gas Shift Reaction: Active Sites and Reaction Mechanism", *Catalysis Today*, Vol. 160, pp. 3-10, 2011.

10. Trimm, D. L., "Minimisation of Carbon Monoxide in a Hydrogen Stream for Fuel Cell Application", *Applied Catalysis A: General*, Vol. 296, pp. 1-11, 2005.

11. Leppelt, R., B. Schumacher, V. Plzak, M. Kinne, and R. J. Behm, "Kinetics and Mechanism of the Low-Temperature Water–Gas Shift Reaction on Au/CeO_2 Catalysts in an Idealized Reaction Atmosphere", *Journal of Catalysis*, Vol. 244, pp. 137-152, 2006.

12. Sato, Y., K. Terada, S. Hasegawa, T. Miyao, and S. Naito, "Mechanistic Study of Water-Gas Shift Reaction over TiO_2 Supported Pt–Re and Pd–Re Catalysts", *Applied Catalysis A: General*, Vol. 296, pp. 80-89, 2005.

13. Haruta, M., "Size- and Support-Dependency in the Catalysis of Gold", *Catalysis Today*, Vol. 36, pp. 153-166, 1997.

14. Cameron, D., R. Holliday, and D. Thompson, "Gold's Future Role in Fuel Cell Systems", *Journal of Power Sources*, Vol. 118, pp. 298-303, 2003.

15. Kim, C. H., and L. T. Thompson, "Deactivation of Au/CeO_x Water Gas Shift Catalysts", *Journal of Catalysis*, Vol. 230, pp. 66-74, 2005.

16. Boccuzzi, F., A. Chiorino, M. Manzoli, D. Andreeva, T. Tabakova, L. Ilieva, and V. Iadakiev, "Gold, Silver and Copper Catalysts Supported on TiO_2 for Pure Hydrogen Production", *Catalysis Today*, Vol. 75, pp. 169-175, 2002.

17. Boaro, M., M. Vicario, J. Llorca, C. Leitenburg, G. Dolcetti, and A. Trovarelli, "A Comparative Study of Water Gas Shift Reaction over Gold and Platinum Supported on ZrO_2 and CeO_2–ZrO_2", *Applied Catalysis B: Environmental*, Vol. 88, pp. 272-282, 2009.

18. Tabakova, T., V. Idakiev, D. Andreeva, and I. Mitov, "Influence of the Microscopic Properties of the Support on the Catalytic Activity of Au/ZnO, Au/ZrO_2, Au/Fe_2O_3, Au/Fe_2O_3–ZnO, Au/Fe_2O_3–ZrO_2 Catalysts for the WGS Reaction", *Applied Catalysis A: General,* Vol. 202, pp. 91-97, 2000.

19. Andreeva, D., V. Idakiev, T. Tabakova, L. Ilievaa, P. Falaras, A. Bourlinos, and A. Travlos, "Low-temperature Water-Gas Shift Reaction over Au/CeO_2 Catalysts", *Catalysis Today*, Vol. 72, pp. 51-57, 2002.

20. Tabakova, T., F. Boccuzzi, M. Manzoli, and D. Andreeva, "FTIR Study of Low Temperature Water Gas Shift Reaction on Gold/Ceria Catalyst", *Applied Catalysis A: General*, Vol. 252, pp. 385-397, 2003.

21. Senanayake, S. D., D. Stacchiola, P. Liu, C. B. Mullins, J. Hrbek, and J. A. Rodriguez, "Interaction of CO with OH on Au(111): HCOO, CO_3, and HOCO as Key Intermediates in the Water-Gas Shift Reaction", *Journal of Physical Chemistry C*, Vol. 113, pp. 19536-19544, 2009.

22. Chen, Y., P. Hua, M. H. Lee, and H. Wang, "Au on (111) and (110) Surfaces of CeO_2: A Density-Functional Theory Study", *Surface Science*, Vol. 602, pp. 1736-1741, 2008.

23. Gajdos, M., A. Eichler, and J. Hafner, "CO Adsorption on Close-Packed Transition and Noble Metal Surfaces: Trends from Ab-initio Calculations", *Journal Of Physics: Condensed Matter,* Vol. 16, pp. 1141-1164, 2004.

24. Piccolo, L., D. Loffreda, F. J. Cadete Santos Aires, C. Deranlot, Y. Jugnet, P. Sautet, and J.C. Bertolini, "The Adsorption of CO on Au(1 1 1) at Elevated Pressures Studied by STM, RAIRS and DFT Calculations", *Surface Science,* Vol. 566-568, pp. 995-1000, 2004.

25. Pessoa, A. M., J. L. C. Fajín, J. R. B. Gomes, and M. N. D. S. Cordeiro, "Cluster and Periodic DFT Calculations of Adsorption of Hydroxyl on the Au(h k l) Surfaces", *Journal of Molecular Structure: THEOCHEM*, Vol. 946, pp. 43-50, 2010.

26. Liu, X. M., Z. M. Ni, P. Yao, Q. Xu, J. H. Mao, and Q. Q. Wang, "Comparison of Three Reaction Mechanisms for theWater Gas Shift Reaction on Au(111) Surface", *Acta Physico-Chimica Sinica*, Vol. 26, pp. 1599-1606, 2010.

27. Liu, P., and J. A. Rodriguez, "Water-Gas-Shift Reaction on Metal Nanoparticles and Surfaces", *Journal of Chemical Physics*, Vol. 126, pp. 1647051-1647058, 2007.

28. Iida, H., and A. Igarashi, "Difference in the Reaction Behavior between Pt-Re/TiO_2 (Rutile) and Pt-Re/ZrO_2 Catalysts for Low-Temperature Water Gas Shift Reaction", *Applied Catalysis A: General*, Vol. 303, pp. 48-55, 2006.

29. Iida, H., K. Yonezawa, M. Kosaka, and A. Igarashi, "Low-Temperature Water Gas Shift Reaction over Pt–Re/TiO_2 Catalysts Prepared by a Sub-critical Drying Method", *Catalysis Communications*, Vol. 10, pp. 627-630, 2009.

30. Azzam, K. G., I. V. Babich., K. Seshan, and L. Lefferts, "A Bifunctional Catalyst for the Single-Stage Water–Gas Shift Reaction in Fuel Cell Applications Part 2. Roles of the Support and Promoter on Catalyst Activity and Stability", *Journal of Catalysis,* Vol. 251, pp. 163-171, 2007.

31. Sato, Y., K. Terada, Y. Soma, T. Miyao, and S. Naito, "Marked Addition Effect of Re upon the Water Gas Shift Reaction over TiO_2 Supported Pt, Pd and Ir Catalysts", *Catalysis Communications*, Vol. 7, pp. 91-95, 2006.

32. Ishikawa, Y., M. S. Liao, and C. R. Cabrera, "Energetics of H_2O Dissociation and CO_{ads}+OH_{ads} Reaction on a Series of Pt–M Mixed Metal Clusters: A Relativistic Density-Functional Study", *Surface Science*, Vol. 513, pp. 98-110, 2002.

33. Choung, S. Y., M. Ferrandon, and T. Krause, "Pt-Re Bimetallic Supported on CeO_2-ZrO_2 Mixed Oxides as Water–Gas Shift Catalysts", *Catalysis Today*, Vol. 99, pp. 257-262, 2005.

34. Pallassana, V., M. Neurock, L.B. Hansen, B. Hammer, and J.K. Norskov, "Theoretical Analysis of Hydrogen Chemisorption on Pd(111), Re(0001) and Pd_{ML}/Re(0001), Re_{ML}/Pd(111) Pseudomorphic Overlayers", *Physical Review B: Condens. Matter*, Vol. 60, pp. 6146-6154, 1999.

35. Hehre, W. J., *A Guide to Molecular Mechanics and Quantum Chemical Calculations*, Wavefunction Inc., California, 2003.

36. Sümer, A., *A Theoretical Study on Catalytic Steps of Hydrogen Production and Purification*, Ph.D. Dissertation, Boğaziçi University.

37. Payne, M. C., M. P. Teter, D. C. Allan, T. A. Arias, and J. D. Joannopoulos, "Iterative Minimization Techniques for Ab-initio Total-Energy Calculations: Molecular Dynamics and Conjugate Gradients", *Reviews of Modern Physics*, Vol. 64, pp. 1045-1097, 1992.

38. Sholl, D. S., and J. A Steckel, *Density Functional Theory: A Practical Introduction*, John Wiley & Sons Inc., New Jersey, 2009.

39. Gülmen, M. A., A. Sümer, and A. E. Aksoylu, "Adsorption Properties of CO on Low-Index Pt_3Sn Surfaces", *Surface Science*, Vol. 600, pp. 4909-4921, 2006.

40. Sümer, A., and A. E. Aksoylu, "CO and O Coadsorption on Pt_3Sn Studied by DFT: Changes in the Adsorptives Properties of the Surface with Alloying and Coverage", *Surface Science*, Vol. 602, pp. 1636-1642, 2008.

41. Accelrys Inc., Materials Studio CASTEP, Accelrys Inc., San Diego, 2001.

42. Hu, P., D. A. King, M. H. Lee, and M. C. Payne, "Orbital Mixing in CO Chemisorption on Transition Metal Surface", *Chemical Physics Letters*, Vol. 246, pp. 73-78, 1995.

43. Lynch, M., and P. Hu, "A Density Functional Theory Study of CO and Atomic Oxygen Chemisorption on Pt(111)", *Surface Science*, Vol. 458, pp. 1-14, 2000.

44. Hu, Z. M., and H. Nakatsuji, "Adsorption and Disproportionation Reaction of OH on Ag Surfaces: Dipped Adcluster Model Study", *Surface Science*, Vol. 425, pp. 296-312, 1999.

45. Hasted, J.B., "Liquid Water: Dielectric Properties", *Water A Comprehensive Treatise*, Vol 1, pp. 255-309, 1972.

46. Pan, Y., J. M. Zhang, W. M. Guan, K. H. Zhang, and S. Chen, "Adsorption Site Preference of CO_2 on the Pt(100) Surface by Ab-initio Calculations", *Journal of Physics and Chemistry of Solids*, Vol. 72, pp. 1-4, 2011.

47. Qi, X. Q., Z. D. Wei, L. Li, M. B. Ji, L. L. Li, Q. Zhang, M. R. Xia, S. G. Chen, and L. J. Yang, "DFT Study on Interaction of Hydrogen with Pd(111)", *Computational and Theoretical Chemistry*, Vol. 979, pp. 96-101, 2012.